The Dissertation Committee for Daniel Ross Tengelsen
certifies that this is the approved version of the following dissertation:

Bubble Pulsation and Translation Near a Soft Tissue Interface

Committee:

Mark F. Hamilton, Supervisor

Stanislav Y. Emelianov

Todd A. Hay

Yurii A. Ilinskii

Preston S. Wilson

Jinying Zhu

Bubble Pulsation and Translation Near a Soft Tissue Interface

by

Daniel Ross Tengelsen, B.S.; M.S.

DISSERTATION

Presented to the Faculty of the Graduate School of

The University of Texas at Austin

in Partial Fulfillment

of the Requirements

for the Degree of

DOCTOR OF PHILOSOPHY

THE UNIVERSITY OF TEXAS AT AUSTIN

May 2014

To my brother, Benn.

Acknowledgments

Large projects such as these do not come to fruition without many contributors. Hence, I wish to recognize the many people that have made this dissertation a reality. I also apologize in advance for the many people who I will forget to thank here; please know that your help and investment in my education is greatly appreciated.

First, I want to thank my wife Kate. She has provided me with unwavering support during my many years of graduate school. I never thought that after six years of marriage I would still be in school. I appreciate her encouragement to help me do my best, and the freedom she gives me to choose to do my best or not. I imagine my life would be much less meaningful without her companionship.

Next, I want to thank my parents. I do not believe I would ever have sought higher education had they not instilled in me a love of learning. Both my parents and several influential teachers, leaders, and friends have influenced and encouraged me to seek higher education and contribute meaningfully to society; I cannot thank them enough for their guidance and examples.

I wish to acknowledge the many hours of diligent feedback provided by my advisor, Dr. Mark Hamilton. At times I imagine it is difficult to continually help students learn to think and discover on their own. I appreciate his candid

efforts to help me become a scientist.

I also wish to thank Dr. Todd Hay. Todd was one of the first people to help me get a grasp on this project, and spent many hours getting me up to speed while I am sure he had many other things to do. He has opened my eyes to many computing resources which I currently use and encourage others to explore. I gratefully acknowledge his many helpful suggestions, patience as I learn, and friendship.

I thank Dr. Yurii Ilinskii and Dr. Evgenia Zabolotskaya. Both of these people are brilliant scientists, and have spent many hours helping me find ways to approach this problem correctly. I have appreciated their kindness and patience with my many, many questions. I also thank them for their kindness after my wife and I had our first child.

I want to thank my remaining committee members, Dr. Preston Wilson, Dr. Stanislav Emelianov, and Dr. Jinying Zhu. I appreciate the time and efforts they have given me to help advance my learning and complete this degree. Even though our interactions have been short, some of the most useful suggestions for this research project have come from them.

I want to thank many others who were indirectly involved in my success, specifically Dr. Michael Haberman and students Scott Schoen, Kyle Spratt, and Derek Thomas. I thank them all for letting me constantly borrow their books, and for acting as constant sounding boards for the many questions which I posed to them. Many of my biggest epiphanies came while talking

with these people, and they all seemed to show a genuine interest in my research problem. I appreciated their interest very much, even if they were just pretending.

The last person I wish to thank is my son, the ever-eager Benson. I believe my ability to work hard is in large part due to his excitement and constant desire to play hard. I love to watch him learn and grow; his curiosity about every little facet of the world is contagious. I also want to thank him for helping me get to work early. Somehow he knows that I am most efficient in the early morning hours; I appreciate him waking up so early (every morning) to help me get to work early. He brings a joy into my life that I did not believe existed.

I thank the Applied Research Laboratories at The University of Texas in Austin for providing me with the McKinney Fellowship. Allowing me to choose my research project was what ultimately brought my family and me to Austin; I could not be more satisfied with our decision. I also thank the Cockrell School of Engineering at The University of Texas at Austin for their additional support—specifically the THRUST fellowship, which allowed our little family to survive on a graduate stipend for the past several years.

Bubble Pulsation and Translation Near a Soft Tissue Interface

Daniel Ross Tengelsen, Ph.D.
The University of Texas at Austin, 2014

Supervisor: Mark F. Hamilton

A Lagrangian formalism presented by Hay, Ilinskii, Zabolotskaya, and Hamilton [J. Acoust. Soc. Am. **132**, 124–137 (2012)] to calculate the pulsation of a spherical bubble, immersed in liquid and near one or two viscoelastic layers, is extended here to include bubble translation. The method presented here is simplified from that given by Hay et al. in that only a single interface between a liquid and a viscoelastic half-space is considered. In the present approach the force on the bubble due to the presence of the liquid-solid interface is calculated using a Green's function that takes into account elastic waves and viscosity in the layer, and the viscous boundary layer within the liquid near the interface. Previous models and experiments have shown that the direction of bubble translation near a viscoelastic layer is correlated with the direction of a liquid jet often produced by the bubble during collapse. In this dissertation an attempt is made to model the pulsation and translation of a spherical bubble near a liquid-solid interface to infer the direction of bubble

translation in reference to material parameters of the liquid and viscoelastic medium, and the standoff distance of the bubble from the interface. The analysis is simplified by demonstrating that the direction of bubble translation can be inferred from the phase of the component of the Green's function associated with the reverberant pressure gradient. For linear bubble pulsation it is shown that the domain of material properties of the viscoelastic medium which generally corresponds to bubble translation away from the interface occurs when the effective stiffness of the viscoelastic medium is greater than the effective damping for both itself and the liquid. The analysis is performed assuming the viscoelastic medium is similar to soft tissue, and its dynamics are described by a Voigt, Kelvin, or Maxwell model. The simulations are compared with existing experimental data. Effects of high-amplitude bubble pulsation are explored in terms of how the simulations differ as the pulsation amplitude increases. At higher pulsation amplitudes, it is shown that bubble translation is still described qualitatively by analyzing the phase of the reverberant pressure gradient.

Table of Contents

List of Tables

List of Figures

List of Symbols

A_d	Amplitude of drive source
c_1	Longitudinal sound speed in an inviscid liquid
E	Young's Modulus
$\boldsymbol{\epsilon}$	Strain tensor
γ	Polytropic index
$\boldsymbol{g}^{(n)}$	Green's function for the n^{th} material
g_{rev}	Reflected portion of the irrotational component of the of the vector Green's function, $\boldsymbol{g}^{(1)}$, in the z direction
K_1	Bulk modulus of the fluid
$k_{l,n}$	Longitudinal wavenumber in the n^{th} material
$k_{t,n}$	Transverse wavenumber in the n^{th} material
κ	Angular spectrum parameter (spatial frequency)
$\kappa_{l,n}$	Component of longitudinal wavenumber perpendicular to interface
$\kappa_{t,n}$	Component of transverse wavenumber perpendicular to interface
λ_n	First Lamé parameter for the n^{th} material
μ_n	Shear modulus for the n^{th} material
P_0	Ambient pressure in the liquid

p_e	External pressures from a drive source
$\phi^{(n)}$	Scalar potential defining the Green's function for the n^{th} material
P_{liq}	Pressure in the liquid at the bubble wall
p_{rev}	Pressure due to reflections from the liquid-solid interface
$\boldsymbol{\psi}^{(n)}$	Vector potential defining the Green's function for the n^{th} material
P_v	Vapor pressure
Q	Volume velocity of the bubble
R	Bubble radius
R_0	Equilibrium bubble radius
Re	Reynolds number
ρ_n	Density of the n^{th} material
σ	Surface tension of the bubble
$\mathbf{u}_e$	Fluid particle displacement due to a drive source
$\mathbf{u}_n$	Particle displacement in the n^{th} material
$\mathbf{u}_{\text{rev}}$	Fluid particle displacement due to reflections from the liquid-solid interface
ω	Angular frequency
W	Sigmoid window
ω_d	Angular frequency of drive source
$\mathbf{X}$	Bubble position

$\mathbf{X}_0$ Reference bubble position

ξ Linearized bubble radius

ζ_n Bulk viscosity for the n^{th} material

Transforms

$\mathcal{F}_\omega\{\cdot\}$ Temporal Fourier transform

$\mathcal{H}_m\{\cdot\}$ Hankel transform of order $m = 0, 1$

Subscripts

e External

l Longitudinal

liq Liquid

max Maximum

rev Reverberant

src Source

t Transverse

Chapter 1

Introduction

In this dissertation we develop a semi-analytic model describing the pulsation and translation of a spherical bubble immersed in a viscous liquid and near a viscoelastic half-space. Within this context, we are primarily interested in bubble translation because it has been correlated with other bubble phenomena of interest, particularly jetting. The study of the direction of bubble translation as a function of the material parameters of the fluid and the nearby viscoelastic medium, distance of the bubble from the fluid-solid interface, and pulsation amplitude of the bubble is the primary goal of this dissertation.

1.1 Motivation

The motivation for this dissertation is the ubiquitous use of micron-sized bubbles in various medical applications. For instance, ultrasound contrast agents (UCAs) are encapsulated microbubbles which are used to enhance the contrast of medical imaging using ultrasound. UCAs have been researched for several decades and greatly increase the usefulness of ultrasound imaging.[4]

Another medical application involving microbubbles is the delivery of either drugs or genes to a specific location within a biological specimen (e.g.,

delivering drugs to a tumor).[4] In this application, the bubbles are either coated with or encapsulate the genes or drugs to be delivered. As such, they are presented into the blood stream and circulate through it until arriving at a specified target site. Upon arriving at this intended location, a low-amplitude external sound field is applied to push the microbubbles near the wall of the blood vessel. Once attached to the vessel wall, a high-amplitude pulse of ultrasound induces large radial oscillations which often fragments the microbubble, thus releasing its contents.[5]

Other medical applications involving microbubbles driven by high-amplitude acoustic fields are procedures like shock-wave lithotripsy (SWL) or high-intensity focused ultrasound (HIFU), which often involve cavitation of the liquid surrounding the kidney stone[6,7] or liquid near the tissue,[8,9] respectively. The collapse of these cavitation bubbles is associated with damage to more rigid structures like boat propellers or the aforementioned kidney stones,[6,10] as well as soft tissue.[9,11,12]

When a bubble begins to collapse, instability and radial asymmetry of the flow surrounding the bubble wall generally causes a portion of the bubble wall to implode more quickly than the rest. This part of the bubble wall can move through the opposing side of the bubble, creating a high-velocity liquid jet.[13] Jetting is an important feature of how bubbles interact with a nearby surface. Because the direction of the bubble jet is highly correlated with the direction of translation,[1] more focus has been given here to model the translational dynamics of microbubbles specifically.

Much research has been done to improve the agreement between experiment and analytical/numerical models with regard to bubble pulsation. This has involved decades of research on many aspects of the bubble model, such as liquid compressibility, frequency of oscillation, constraining media, etc. While this research has been imperative for other applications, this dissertation focuses less on the radial pulsation of the bubble and more on the translational dynamics.

1.2 Overview of Previous Research

The study of gas bubbles immersed in liquid began over a century ago,[14] and Lord Rayleigh is often cited as the first to develop a theoretical model.[15] Many others have researched various aspects of bubble dynamics in an unbounded liquid; an exhaustive review of bubble dynamics in an unbounded liquid is found in Leighton.[16] However, the study of bubbles in constrained spaces is much less prevalent—especially when one considers tissue-like boundaries as the constraining media.

1.2.1 Bubbles in constrained media

One of the first works to consider a single gas bubble within a constraining environment was by Oğuz and Prosperetti.[17] They developed a model to study the natural oscillation frequency of a gas-filled bubble confined within a rigid tube of varying geometries. They showed that the natural oscillation frequency of the bubble was altered as the size of both the bubble and the

tube changed. Chen and Prosperetti[18] considered the same environment, but included thermal damping effects and matched the bubble radius to the radius of the confining tube within their model. The original model by Oğuz and Prosperetti[17] was also extended by Sassaroli and Hynynen,[19] also by including thermal damping, as they considered bubbles within mesentery capillaries. They too, however, assumed the capillaries are rigid.

1.2.2 Liquid compressibility

The authors who first created models of bubbles in constraining spaces assumed an incompressible liquid, which was likely appropriate for their respective applications (actuators in fluid-handling devices). However, when multiple bubbles or a bubble near an interface (that does not occupy the entirety of a cross section of the confining space) is considered, liquid compressibility becomes an important feature in the model.[20–26]

Other authors have expanded another branch of bubble-dynamics research, where they considered multiple-bubble systems.[20,24,25] In these works, liquid compressibility is included via a time delay. Incorporating this time delay in the bubble dynamics can significantly alter the bubble dynamics—even when the distance between the bubbles is very small.[21] Another aspect of liquid compressibility is the damping of bubble pulsation associated with radiation into the fluid.[22,23,26,27] Including this effect can cause numerical instabilities in the model,[21] and is more relevant when considering high-amplitude bubble oscillations. The effect of radiation damping is neglected in this dissertation;

however, liquid compressibility is accounted for via a time delay of reflections back onto the bubble from the interface.

Including liquid compressibility in models of bubbles in constrained environments was considered by Leighton et al.[28,29] In Ref. 29, they consider the effect of a rectangular tank on the radial dynamics of an oscillating bubble. They perform this analysis via a Green's function, where the tank is replaced by other sources using the method of images.

Cui et al.[30] considered a bubble constrained between two rigid parallel boundaries, and used the method of images to study the fields created by the resulting bubble arrays. Their work also included liquid compressibility via an appropriate time delay for each image source. This approach was then extended by the same research group to include triangular, rectangular, and hexagonal boundaries.[31]

Including compliance in the confining structure was undertaken by Hay et al.[2] They considered a bubble between two viscoelastic parallel layers, and studied the effects of bubble pulsation due to tissue-like layers. Similar to the work performed within this dissertation, they employed a Green's function approach which accounted for the shear effects within the solid layers and a viscous boundary layer within the fluid. The model presented in this dissertation is simplified geometrically from that of Hay et al.[2] due to the large range of tissue parameters under investigation. However, the model in this dissertation is also more complex in that it includes bubble translation in addition to radial pulsation.

Recently, a portion of the results presented by Hay et al.[2] was questioned by Doinikov and Bouakaz.[32] Specifically, Doinikov and Bouakaz[32] questioned the results for a bubble near a single layer of polystyrene—also referred to as OptiCell, a common material used in microbubble experiments. While Hay et al.[2] showed a decrease in the natural frequency of a bubble near a single layer of OptiCell, the model developed by Doinikov and Bouakaz showed an increase in the natural frequency. With these discrepancies currently being discussed in the literature, and with very little experimental work published on this subject, it is important that more research is dedicated to this subject.

1.2.3 Bubble translation and jetting

Translation of sources has long been considered in other fields outside the realm of bubble dynamics,[33–35] while much of the work has application to the fields of underwater acoustics[36–39] and aeroacoustics.[40–42] Translation of bubbles, in particular, has also been studied in great detail, usually in the context of multiple interacting bubbles.[25,43–46] Brujan et al.[1,13] considered translation (and subsequent jetting) of laser-generated cavitation bubbles near various tissue phantoms with differing elastic properties. They showed that the direction of jetting and bubble translation was dependent on both the distance of the bubble from the interface and the shear modulus of the solid. Chen et al.[3,47] also considered various experiments regarding translation of microbubbles in fluid near a soft-tissue boundary. Their results showed that, for a soft-tissue boundary, bubble translation is directed away from the nearest

vessel wall.

Hay et al.[48] modeled bubble oscillation and translation of a bubble between two parallel elastic layers. This model included shape deformation of the bubble wall and was able to show shape deformation indicative of jetting away from the nearest elastic layer. However, in this model Hay et al.[48] assumed the density and sound speed for each layer was identical to those of the fluid.

1.2.4 Our model

Because bubble channels can be large, such that the effects of the opposite side of the vessel wall seem negligible, we restrict the analysis of this dissertation to a bubble immersed in a viscous fluid near a viscoelastic half-space. In other words, only a single elastic half-space is considered here. We include the effects of viscosity in both the fluid and the solid, and account for translation and spherical pulsation of the bubble. We do not model shape deformation of the bubble wall to study jetting. Instead, we infer the direction of the jet based on the initial direction of translation.

1.3 Summary and Preview of Dissertation

Chapter 2 outlines the basic equations which model a spherically pulsating and translating bubble immersed in a fluid and near a solid. Both the differential equations for the dynamics of the bubble and the surrounding fluid/solid media are covered in detail. The pressure and its corresponding

gradient produced by the presence of the interface are derived via a Green's function method, which admits solutions for the reflected fields due to an interface between an arbitrary viscous fluid and viscoelastic medium. The equations defining the reflected fields are linear for both the fluid and elastic solid, as required by the Green's function.

Chapter 3 deals with the numerical implementation of the theory provided in Chapter 2. We discuss the nondimensionalization of the bubble dynamics equations such that numerical simulations are robust and accurate. We show the various steps required to accurately perform the numerical integrations, inverse transforms, and convolutions inherent in this problem. We also explore the amount of rigor required to accurately represent a Green's function whose spatial coordinates vary as a function of time. Last, we outline several inaccuracies which are likely to be encountered during the numerical simulation of this problem.

Chapter 4 verifies the numerical implementation of the bubble-dynamics equations in three ways. First, we check the numerical implementation of a pulsating bubble near either a rigid or pressure-release boundary by comparing it with its tractable analytical solution. Low-amplitude simulations show changes in oscillation frequency as a function of distance from the boundary, and high-amplitude simulations are compared with the Rayleigh collapse time. Second, frequency spectra associated with the numerical calculation of the reverberant pressure are compared with corresponding results from simplified interface conditions to ensure that the calculations are performed correctly.

Third, translation is included and we show that the direction of bubble translation due to the presence of the fluid-solid interface is consistent with experiments. We also show modifications to the reverberant fields once we include bubble translation. These modifications alter the overall amplitude and time of arrival of the reflected fields at the bubble location.

Chapter 5 presents several parametric studies of both bubble and material parameters, as pertaining to direction of bubble translation. The varied bubble parameters are the distance of the bubble from the interface and its overall size, and the varied material parameters are the fluid shear viscosity and all of the parameters for the viscoelastic medium. It is shown that, for low-amplitude pulsation, bubble translation is correlated with the phase of the reverberant pressure gradient produced by the presence of the interface, relative to the phase of the bubble pulsation. More specifically, we show that knowing the phase of the portion of the Green's function corresponding to the reverberant pressure gradient, at the oscillation frequency of the bubble, is sufficient to predict direction of bubble translation. Several different models commonly used to represent tissue-like media are explored, and the regions of material parameters which admit bubble translation away from the interface are described.

Since we only considers low-amplitude bubble pulsation in Chapter 5, Chapter 6 presents our analysis of how direction of bubble translation is affected for highly nonlinear bubble pulsation. While we consider relatively few tissue-like media in this chapter, we present several simulations to consider

the gradual introduction of higher amplitude bubble pulsation. We continue to analyze the portion of the Green's function associated with the reverberant pressure gradient, and show that its phase may still be used to qualitatively predict direction of bubble translation.

Chapter 7 provides a summary of the dissertation and suggestions for possible extensions of this work in the future. In addition, there are several appendices which expound on various supporting topics. These appendices contain derivations of key results within the main text, and expressions for simplified models which are used to verify these results.

Chapter 2

Mathematical Model

In this chapter we develop a model for a pulsating and translating bubble near an arbitrary liquid-solid interface. First, we introduce two coupled nonlinear second-order ordinary differential equations (ODE) which describe the pulsation and translation of a spherical bubble over time. Pulsation is described by a Rayleigh-Plesset type equation, and bubble translation is described via a momentum equation. Second, we mathematically describe the terms present in these equations which are due to the presence of the liquid-solid interface. The interface affects pulsation through a pressure field reflected back onto the bubble, while translation is affected by the gradient of the reflected pressure. We consider specifically the case of a spherical bubble immersed in a viscous fluid near a viscoelastic solid, and solve for the reverberant fields analytically in the angular-spectrum domain. This is performed by using a Green's function method, and by expressing the particle displacement in both the fluid and the solid via scalar and vector potentials. Because the reverberant fields are expressed analytically in the angular-spectrum domain, including them in the temporal ODE's describing the bubble dynamics involves expressing them in the time domain. This occurs after numerical integration in both the angular-spectrum and frequency domains. The approach

used here is identical in methodology to that used by Hay et al.,[2] except that translation is now included in the analysis and the geometry is simplified.

2.1 Bubble Dynamics

Many theories have been developed to describe the dynamics of pulsating and translating gas-filled bubbles in liquid.[45,46,49,50] The history of the relevant experiments performed and models developed to understand bubble translation is given by Harkin et al.,[46] while a thorough review of the recent literature is performed by Ilinskii et al.[45] With a wealth of information at hand, we merely state without derivation the coupled equations describing bubble pulsation and translation:

$$R\ddot{R} + \frac{3}{2}\dot{R}^2 = \frac{P_{\text{liq}} - P_0}{\rho_1} - \left(\frac{p_e + p_{\text{rev}}}{\rho_1} - \frac{1}{4}\left| \dot{\mathbf{X}} - (\dot{\mathbf{u}}_e + \dot{\mathbf{u}}_{\text{rev}}) \right|^2 \right) , \quad (2.1)$$

$$\frac{d}{dt}\left\{ R^3 \left[\dot{\mathbf{X}} - (\dot{\mathbf{u}}_e + \dot{\mathbf{u}}_{\text{rev}}) \right] \right\} = -2R^3 \boldsymbol{\nabla} \left(\frac{p_e + p_{\text{rev}}}{\rho_1} - \frac{1}{4}\left| \dot{\mathbf{X}} - (\dot{\mathbf{u}}_e + \dot{\mathbf{u}}_{\text{rev}}) \right|^2 \right) + \frac{3\mathbf{F}_d}{2\pi\rho_1} , \quad (2.2)$$

where R is the bubble radius, $\mathbf{X}$ is the position of the bubble and $\dot{\mathbf{X}}$ is its translational velocity, ρ_1 is the fluid density, P_0 is atmospheric pressure, P_{liq} is the liquid pressure just outside the bubble wall, $\mathbf{F}_d$ is the drag force on the bubble due to liquid viscosity, p_e and $\mathbf{u}_e$ are the external source pressure and particle displacement, respectively, and $\dot{\mathbf{u}}_e$ is the corresponding particle

velocity. Equations (2.1) and (2.2) are modified from Eqs. (42) and (43) of Ilinskii et al.[45] to include the terms p_{rev}, $\boldsymbol{\nabla} p_{\text{rev}}$, and $\mathbf{u}_{\text{rev}}$. These terms are included to account for the reflections of the acoustic waves propagating back onto the bubble (and originally radiated by the bubble) due to the presence of the liquid-solid interface. Although these terms exist due to motion of the bubble, they appear as additions to the external external field variables p_e, $\boldsymbol{\nabla} p_e$, and $\mathbf{u}_e$; this is because the reflected fields modify the external dynamics of the liquid and solid, consequently affecting the overall fields that interact with the bubble dynamics. Equation (2.1) is a modified form of the Rayleigh-Plesset equation, and is reduced to such by neglecting bubble translation (the last term on the right-hand side) and the reverberant field variables, while Eq. (2.2) is a momentum equation.

The last term on the right-hand side of Eq. (2.2) is also modified from the expression given in Eqs. (45) and (46) of Ilinskii et al.[45] to include the reverberant field variables:

$$\mathbf{F}_d = -4\pi\eta R\left[\dot{\mathbf{X}} - (\dot{\mathbf{u}}_e + \dot{\mathbf{u}}_{\text{rev}})\right] \text{ , } \text{Re} \ll 1 \quad \text{and} \quad \frac{\text{Re}\dot{R}}{\dot{\mathbf{X}} - (\dot{\mathbf{u}}_e + \dot{\mathbf{u}}_{\text{rev}})} \ll 1\,, \tag{2.3}$$

$$= -12\pi\eta R\left[\dot{\mathbf{X}} - (\dot{\mathbf{u}}_e + \dot{\mathbf{u}}_{\text{rev}})\right] \text{ , } \text{Re} \gg 1 \quad \text{or} \quad \frac{\text{Re}\dot{R}}{\dot{\mathbf{X}} - (\dot{\mathbf{u}}_e + \dot{\mathbf{u}}_{\text{rev}})} \gg 1\,, \tag{2.4}$$

where $\text{Re} = \rho_1 R[\dot{\mathbf{X}} - (\dot{\mathbf{u}}_e + \dot{\mathbf{u}}_{\text{rev}})]/\eta_1$ is the Reynolds number and η_1 is the shear viscosity of the liquid.[49–51]

The pressure in the liquid adjacent to the bubble wall is given in

Eq. (4.81) of Leighton[16] as

$$P_{\text{liq}} = \left(P_0 + \frac{2\sigma}{R_0} - P_v\right)\left(\frac{R_0}{R}\right)^{3\gamma} + P_v - \frac{2\sigma}{R} - 4\eta_1\frac{\dot{R}}{R}\,, \tag{2.5}$$

where σ is the surface tension, R_0 is the equilibrium bubble radius, P_v is the vapor pressure, and γ is the polytropic index.[†] This pressure is an aggregate of several different mechanisms such as surface tension, vapor pressure, and ambient pressure, in addition to the damping due to liquid viscosity which is accounted for via the last term on the right-hand side.

There are many modifications that have been made to the Rayleigh-Plesset equation to account for liquid compressibility,[21–23] radiation damping,[27,52] thermal damping,[53,54] etc. Generally, these modifications are higher-order corrections to the bubble dynamics and are unnecessary until we consider high-amplitude bubble dynamics (Chapter 6). By similar logic, the higher-order term introduced into the translation equation by Ilinskii et al.[45] [the term $\boldsymbol{\nabla}|\dot{\mathbf{X}} - (\dot{\mathbf{u}}_e + \dot{\mathbf{u}}_{\text{rev}})|^2/4$ in Eq. (2.2)] is also ignored.

Solving numerically for the radius R and position $\mathbf{X}$ of the bubble can be quite simple. Many of the parameters are not functions of time and are merely inputs into the equations. In fact, in this model the only time dependent parameters (other than the parameters R and $\mathbf{X}$) are field variables p_e and $\mathbf{u}_e$ created by a driving source and the reverberant fields p_{rev} and $\mathbf{u}_{\text{rev}}$ created by reflections from the liquid-solid interface.

[†]The symbol γ usually signifies the ratio of specific heats; however, we use it here to indicate the polytropic index since the usual symbol κ is used extensively to represent the angular-spectrum wavenumber.

2.2 Dynamical Fluid/Solid Field Variables

In order to solve for the fluid pressure and particle velocity acting on the bubble, we need to model the wave motion in both the fluid and solid. This model is coupled to the bubble-dynamics model presented in Section 2.1 via the reverberant field variables (p_{rev}, $\boldsymbol{\nabla} p_{\text{rev}}$, and $\mathbf{u}_{\text{rev}}$) in Eqs. (2.1) and (2.2). Assuming the fluid and the elastic solid are viscous, the linearized momentum equations for the fluid and solid can be written, respectively, as

$$\left(\mathcal{L}_1 - \rho_1 \frac{\partial^2}{\partial t^2}\right) \mathbf{u}_1 = K_1 \boldsymbol{\nabla} S[t, \mathbf{X}(t)] \,, \tag{2.6}$$

$$\left(\mathcal{L}_2 - \rho_2 \frac{\partial^2}{\partial t^2}\right) \mathbf{u}_2 = \mathbf{0} \,, \tag{2.7}$$

where $\mathbf{u}_1$ represents the displacement field within the fluid, $\mathbf{u}_2$ represents the displacement field within the solid, K_1 represents the bulk modulus of the fluid, and where $\mathcal{L}_1$ and $\mathcal{L}_2$ are linear operators which can be expressed generally such that

$$\mathcal{L}_n \mathbf{u}_n = \left(\lambda_n + \zeta_n \frac{\partial}{\partial t} + \mu_n + \eta_n \frac{\partial}{\partial t}\right) \boldsymbol{\nabla}\boldsymbol{\nabla} \cdot \mathbf{u}_n + \left(\mu_n + \eta_n \frac{\partial}{\partial t}\right) \boldsymbol{\nabla} \cdot \boldsymbol{\nabla} \mathbf{u}_n \,, \tag{2.8}$$

for $n = 1, 2$. Constant λ_n is the first Lamé parameter, ζ_n is the bulk viscosity,[†] μ_n is the shear modulus, and η_n is the shear viscosity for the n^{th} material. Subscript $n = 1$ represents variables within the fluid and $n = 2$ represents variables within the solid, as illustrated in Fig. 2.1. Variable $S[t, \mathbf{X}(t)]$ in

[†]In order to compare with the linearized version of Eq. (15.5) in Landau and Lifshitz,[55] let $\zeta_1 = \zeta^{(L)} - 2\eta^{(L)}/3$ and $\eta_1 = \eta^{(L)}$ where $\zeta^{(L)}$ and $\eta^{(L)}$ are the bulk and shear viscosity in Ref. 55, respectively. The constant $\zeta^{(L)}$ is called the *second viscosity* in their text.

Eq. (2.6) is the source function, which is written in terms of both bubble pulsation and translation as

$$S[t, \mathbf{X}(t)] = \int_{-\infty}^{t} Q(t')\delta[\mathbf{x} - \mathbf{X}(t')]\, dt' \,, \tag{2.9}$$

where Q is the volume velocity of the bubble, and is related to the bubble radius as $Q = 4\pi R^2 \dot{R}$. The source appears only in Eq. (2.6) since the bubble resides in the fluid, and not the solid. In addition, because the fluid is assumed nearly ideal, and only pulsates spherically, the source is only compressional in nature. While we assume the fluid to have zero shear modulus ($\mu_1 = 0$), including shear viscosity in the fluid allows for the presence of shear effects within a region of fluid close to the interface, referred to as the boundary layer. A more intuitive grasp on the source function is obtained by taking a derivative with respect to time of Eq. (2.6), which then relates the fluid particle velocity to the volume velocity of the source; this is a more conventional way of modelling moving sources in fluids.[†]

We solve Eqs. (2.6) and (2.7) by using a Green's function method. This involves replacing the forcing function on the right-hand side of Eq. (2.6) with delta functions in both space and time. Even though the spatial component of the Green's function is already given as a delta function, it is still replaced with one that does not involve time; in this manner, the temporally-variant spatial component of the forcing function is involved in final convolution reproducing particle displacement. The final result is then a convolution of the Green's

[†]Equation (11.2.8) of Morse and Ingard[35] or Chapter 9 of Dowling and Ffowcs Williams.[34]

function with the forcing function.[†] One advantage of this approach is that we can now solve the problem at a single instant in time, setting the source at a single position in space. In other words, even though the source is translating, this approach allows us to consider the source to be stationary and deal with its translation as a part of the convolution. Thus, our attention momentarily shifts to solving

$$\left(\mathcal{L}_1 - \rho_1 \frac{\partial^2}{\partial t^2}\right) \boldsymbol{g}^{(1)} = K_1 \delta(t) \boldsymbol{\nabla} \delta[\mathbf{x} - \mathbf{X}_0]\,, \tag{2.10}$$

$$\left(\mathcal{L}_2 - \rho_2 \frac{\partial^2}{\partial t^2}\right) \boldsymbol{g}^{(2)} = \mathbf{0}\,, \tag{2.11}$$

where $\mathbf{X}_0$ is the time-independent source position used to determine the Green's functions $\boldsymbol{g}^{(1)}$ and $\boldsymbol{g}^{(2)}$. We intentionally leave the fluid bulk modulus on the right-hand side of Eq. (2.10) for later simplifications. To solve Eqs. (2.10) and (2.11), we express $\boldsymbol{g}^{(n)}$ in terms of a scalar potential ϕ^n and a vector potential $\boldsymbol{\psi}^{(n)}$ (a Helmholtz decomposition),

$$\boldsymbol{g}^{(n)} = \boldsymbol{\nabla} \phi^{(n)} + \boldsymbol{\nabla} \times \boldsymbol{\psi}^{(n)}\,. \tag{2.12}$$

This decomposition requires an additional condition so that the four functions defined by the decomposition are not arbitrary with respect to the three components of $\boldsymbol{g}^{(n)}$; this is known as a gauge condition and is chosen to be[‡]

$$\boldsymbol{\nabla} \cdot \boldsymbol{\psi}^{(n)} = 0 \tag{2.13}$$

[†]Morse and Feshbach,[56] Barton,[57] and Duffy,[58] are exhaustive sources to learn more about Green's functions.

[‡]See pages 210-212 of Morse and Feshbach[56] for more background on gauge functions.

for the n^{th} material. Using this gauge condition along with the vector identity[†]

$$\nabla^2 \boldsymbol{g}^{(n)} = \boldsymbol{\nabla}\left(\boldsymbol{\nabla}\cdot\boldsymbol{g}^{(n)}\right) - \boldsymbol{\nabla}\times\left(\boldsymbol{\nabla}\times\boldsymbol{g}^{(n)}\right)\,, \tag{2.14}$$

substitution of Eq. (2.12) into Eq. (2.10) with $n = 1$ and Eq. (2.11) with $n = 2$ yields

$$\boldsymbol{\nabla}\left\{\left[\lambda_1 + \zeta_1\frac{\partial}{\partial t} + 2\left(\mu_1 + \eta_1\frac{\partial}{\partial t}\right)\right]\nabla^2\phi^{(1)} - \rho_1\frac{\partial^2}{\partial t^2}\phi^{(1)} - K_1\delta(t)\delta(\mathbf{x}-\mathbf{X}_0)\right\} + \boldsymbol{\nabla}\times\left[\left(\mu_1 + \eta_1\frac{\partial}{\partial t}\right)\nabla^2\boldsymbol{\psi}^{(1)} - \rho_1\frac{\partial}{\partial t}\boldsymbol{\psi}^{(1)}\right] = \mathbf{0}\,, \tag{2.15}$$

$$\boldsymbol{\nabla}\left\{\left[\lambda_2 + \zeta_2\frac{\partial}{\partial t} + 2\left(\mu_2 + \eta_2\frac{\partial}{\partial t}\right)\right]\nabla^2\phi^{(2)} - \rho_2\frac{\partial^2}{\partial t^2}\phi^{(2)}\right\} + \boldsymbol{\nabla}\times\left[\left(\mu_2 + \eta_2\frac{\partial}{\partial t}\right)\nabla^2\boldsymbol{\psi}^{(2)} - \rho_2\frac{\partial}{\partial t}\boldsymbol{\psi}^{(2)}\right] = \mathbf{0}\,. \tag{2.16}$$

Since the terms in both Eq. (2.15) and Eq. (2.16) are taken to be independent of one another, each must therefore individually be zero. This leads to the following wave equations for longitudinal and shear wave propagation in both the fluid and the solid:

$$\left[\lambda_1 + \zeta_1\frac{\partial}{\partial t} + 2\left(\mu_1 + \eta_1\frac{\partial}{\partial t}\right)\right]\nabla^2\phi^{(1)} - \rho_1\frac{\partial^2}{\partial t^2}\phi^{(1)} = K_1\delta(t)\delta(\mathbf{x}-\mathbf{X}_0)\,, \tag{2.17}$$

$$\left(\mu_1 + \eta_1\frac{\partial}{\partial t}\right)\nabla^2\boldsymbol{\psi}^{(1)} - \rho_1\frac{\partial^2}{\partial t^2}\boldsymbol{\psi}^{(1)} = \mathbf{0}\,, \tag{2.18}$$

$$\left[\lambda_2 + \zeta_2\frac{\partial}{\partial t} + 2\left(\mu_2 + \eta_2\frac{\partial}{\partial t}\right)\right]\nabla^2\phi^{(2)} - \rho_2\frac{\partial^2}{\partial t^2}\phi^{(2)} = 0\,, \tag{2.19}$$

$$\left(\mu_2 + \eta_2\frac{\partial}{\partial t}\right)\nabla^2\boldsymbol{\psi}^{(2)} - \rho_2\frac{\partial^2}{\partial t^2}\boldsymbol{\psi}^{(2)} = \mathbf{0}\,. \tag{2.20}$$

[†]Equation (1.5.12) of Morse and Feshbach.[56]

In order to express Eqs. (2.17) to (2.20) in the frequency domain, we define the temporal Fourier transform pair, using the function $\phi^{(n)}$ for demonstration:

$$\begin{aligned}\widehat{\phi}^{(n)}(\omega,\mathbf{x}) &= \mathcal{F}_\omega\big\{\phi^{(n)}(t,\mathbf{x})\big\} \\ &= \int_{-\infty}^{\infty} \phi^{(n)}(t,\mathbf{x}) e^{i\omega t}\, dt\,, \end{aligned} \tag{2.21}$$

$$\begin{aligned}\phi^{(n)}(t,\mathbf{x}) &= \mathcal{F}_\omega^{-1}\Big\{\widehat{\phi}^{(n)}(\omega,\mathbf{x})\Big\} \\ &= \frac{1}{2\pi}\int_{-\infty}^{\infty} \widehat{\phi}^{(n)}(\omega,\mathbf{x}) e^{-i\omega t}\, d\omega\,, \end{aligned} \tag{2.22}$$

where throughout this dissertation a hat $\widehat{\cdot}$ signifies the temporal Fourier transform of the corresponding variable. Hence, setting $K_1 = \rho_1 c_1^2$ and performing a forward temporal Fourier transform on Eqs. (2.17) to (2.20) yields

$$\nabla^2\widehat{\phi}^{(1)} + k_{l,1}^2\widehat{\phi}^{(1)} = \delta(\mathbf{x}-\mathbf{X}_0)\,, \tag{2.23}$$

$$\nabla^2\widehat{\boldsymbol{\psi}}^{(1)} + k_{t,1}^2\widehat{\boldsymbol{\psi}}^{(1)} = \mathbf{0}\,, \tag{2.24}$$

$$\nabla^2\widehat{\phi}^{(2)} + k_{l,2}^2\widehat{\phi}^{(2)} = 0\,, \tag{2.25}$$

$$\nabla^2\widehat{\boldsymbol{\psi}}^{(2)} + k_{t,2}^2\widehat{\boldsymbol{\psi}}^{(2)} = \mathbf{0}\,. \tag{2.26}$$

where $k_{l,n}$ and $k_{t,n}$ are the longitudinal and transverse wavenumbers within the n^{th} material, respectively, defined as

$$k_{l,n} = \omega\sqrt{\frac{\rho_n}{\tilde{\lambda}_n + 2\tilde{\mu}_n}}\,, \tag{2.27}$$

$$k_{t,n} = \omega\sqrt{\frac{\rho_n}{\tilde{\mu}_n}}\,, \tag{2.28}$$

where $\tilde{\lambda}_n = \lambda_n - i\omega\zeta_n$ and $\tilde{\mu}_n = \mu_n - i\omega\eta_n$.

2.3 Bubble Near a Viscoelastic Half-space

The study of reflection and transmission from a liquid-solid interface is not new.[†] Traditionally, however, the problem is explored from a wave propagation standpoint. In this dissertation the bubble is considered to be very close to the interface where we anticipate a large portion of the reflected field to decay exponentially from the interface (i.e., to evanesce). Bearing this in mind, the general solutions for the field variables are structured differently. Another difference is that the typical presentation of this problem employs a Cartesian coordinate system. However, the most convenient coordinate system for a spherical bubble near a planar liquid-solid interface is a cylindrical coordinate system. While cylindrical coordinates have been employed by others,[60,61] the source term here is different and viscosity is added to the analysis. The boundary conditions here are identical to those posed by Hay et al.;[2] however, in this dissertation the details of the derivation are explicitly performed in cylindrical coordinates (r, φ, z), and are reduced in complexity due to a simple half-space geometry.

Mathematically, we are solving Eqs. (2.17) to (2.20) for a point source located at $\mathbf{X}_0 = (0, 0, -z_0)$. We assume that the bubble translates only along the z axis, which is normal to the solid-liquid interface located at $z = 0$, as shown in Fig. 2.1. Because the problem is axially symmetric, we require that the angular component of the displacement field be zero. Hence, only the φ

[†]See, for example, Chapter 4 of Brekhovskikh and Godin,[59] Chapter 7 of Achenbach,[60] and papers by Zhu et al.,[61] Hay et al.,[2] or de Hoop.[62]

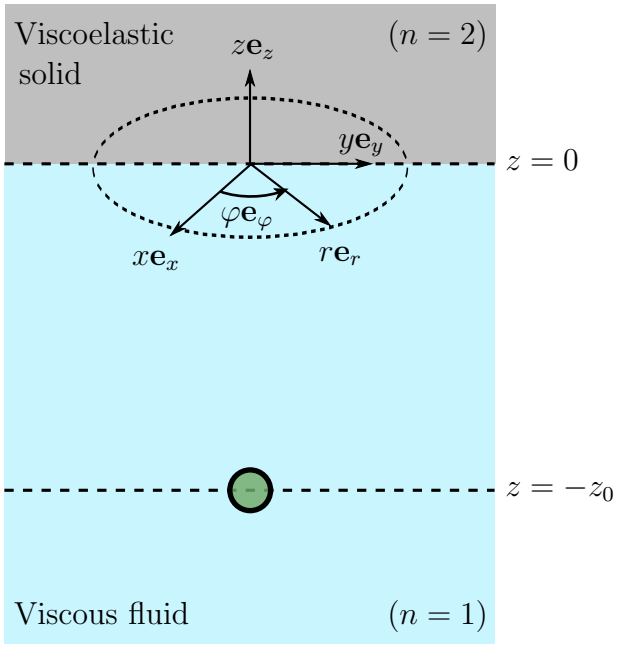

Figure 2.1: Geometry of a bubble immersed in a viscous fluid near a viscoelastic half-space.

component of the vector potentials $\boldsymbol{\psi}^{(n)}$ will have nonzero values. Thus, the components of Eq. (2.12) may be reduced to

$$g_r^{(n)} = \frac{\partial \phi^{(n)}}{\partial r} - \frac{\partial \psi^{(n)}}{\partial z} \,, \tag{2.29}$$

$$g_\varphi^{(n)} = 0 \,, \tag{2.30}$$

$$g_z^{(n)} = \frac{\partial \phi^{(n)}}{\partial z} + \frac{1}{r}\frac{\partial}{\partial r}\left(r\psi^{(n)}\right) \,, \tag{2.31}$$

where $\boldsymbol{\psi}^{(n)} = \psi^{(n)}\mathbf{e}_\varphi$.

Before using Eqs. (2.29)–(2.31) to solve Eqs. (2.23)–(2.26), we express $g^{(n)}$ through its angular spectrum. The following spatial Fourier trans-

form pairs are defined to express the potential functions $\phi^{(n)}$ and $\psi^{(n)}$ (comprising $g^{(n)}$) as angular spectra within their respective Helmholtz equations [Eqs. (2.23)–(2.26)]:

$$\begin{aligned}\Phi^{(n)}(\omega,\kappa,z) &= 2\pi\mathcal{H}_0\left\{\widehat{\phi}^{(n)}(\omega,r,z)\right\} \\ &= 2\pi\int_0^\infty \widehat{\phi}^{(n)}(\omega,r,z)J_0(\kappa r)r\,dr\,, \end{aligned} \tag{2.32}$$

$$\begin{aligned}\widehat{\phi}^{(n)}(\omega,r,z) &= \frac{1}{2\pi}\mathcal{H}_0^{-1}\left\{\Phi^{(n)}(\omega,\kappa,z)\right\} \\ &= \frac{1}{2\pi}\int_0^\infty \Phi^{(n)}(\omega,\kappa,z)J_0(\kappa r)\kappa\,d\kappa\,, \end{aligned} \tag{2.33}$$

for the scalar potentials, and

$$\begin{aligned}\Psi^{(n)}(\omega,\kappa,z) &= 2\pi\mathcal{H}_1\left\{\widehat{\psi}^{(n)}(\omega,r,z)\right\} \\ &= 2\pi\int_0^\infty \widehat{\psi}^{(n)}(\omega,r,z)J_1(\kappa r)r\,dr\,, \end{aligned} \tag{2.34}$$

$$\begin{aligned}\widehat{\psi}^{(n)}(\omega,r,z) &= \frac{1}{2\pi}\mathcal{H}_1^{-1}\left\{\Psi^{(n)}(\omega,\kappa,z)\right\} \\ &= \frac{1}{2\pi}\int_0^\infty \Psi^{(n)}(\omega,\kappa,z)J_1(\kappa r)\kappa\,d\kappa\,, \end{aligned} \tag{2.35}$$

for the vector potentials. We define variables $r = \sqrt{x^2+y^2}$ and κ as the spatial analog of angular frequency, where J_m is the Bessel function of the first kind of order m which is associated with the Hankel transform of the same order $\mathcal{H}_m$. In cylindrical coordinates we note that the angular spectrum for the scalar potential is obtained differently than for the vector potential. This is because the Laplacian of the scalar potential satisfies the corresponding component of Bessel's equation for J_0, whereas the Laplacian of the vector potential satisfies

the same component of Bessel's equation for J_1.[†] Using the spatial transforms given in Eqs. (2.32)–(2.35), we transform Eqs. (2.23)–(2.26) to the angular-spectrum domain, resulting in the following ordinary differential equations:

$$\frac{\partial^2}{\partial z^2}\Phi^{(1)} - \kappa_{l,1}^2\Phi^{(1)} = \delta\left(z+z_0\right)\,, \tag{2.36}$$

$$\frac{\partial^2}{\partial z^2}\Psi^{(1)} - \kappa_{t,1}^2\Psi^{(1)} = 0\,, \tag{2.37}$$

$$\frac{\partial^2}{\partial z^2}\Phi^{(2)} - \kappa_{l,2}^2\Phi^{(2)} = 0\,, \tag{2.38}$$

$$\frac{\partial^2}{\partial z^2}\Psi^{(2)} - \kappa_{t,2}^2\Psi^{(2)} = 0\,, \tag{2.39}$$

where

$$\kappa_{l,n}^2 = \kappa^2 - k_{l,n}^2\,, \tag{2.40}$$

$$\kappa_{t,n}^2 = \kappa^2 - k_{t,n}^2\,. \tag{2.41}$$

General solutions for Eqs. (2.36) to (2.39) are written in the form

$$\Phi^{(1)} = \begin{cases} Ae^{-\kappa_{l,1}z} + Be^{\kappa_{l,1}z} & \text{for } -z_0 \le z \le 0\,, \\ Ce^{\kappa_{l,1}z} & \text{for } z \le -z_0\,, \end{cases} \tag{2.42}$$

$$\Psi^{(1)} = De^{\kappa_{t,1}z} \qquad \text{for } z \le 0\,, \tag{2.43}$$

$$\Phi^{(2)} = Ee^{-\kappa_{l,2}z} \qquad \text{for } z \ge 0\,, \tag{2.44}$$

$$\Psi^{(2)} = Fe^{-\kappa_{t,2}z} \qquad \text{for } z \ge 0\,, \tag{2.45}$$

where A, B, C, D, E, and F are unknown coefficients that are obtained by satisfying the boundary conditions. This form of a general solution represents

[†] $\boldsymbol{\nabla}^2\phi^{(n)} = \left(\frac{\partial^2}{\partial r^2} + \frac{1}{r}\frac{\partial}{\partial r} + \frac{\partial^2}{\partial z^2}\right)\phi^{(n)}$ is the Laplacian of the scalar potential, whereas the Laplacian for the vector potential is $\boldsymbol{\nabla}^2\boldsymbol{\psi}^{(n)} = -\boldsymbol{\nabla}\times\boldsymbol{\nabla}\times\boldsymbol{\psi}^{(n)} = \left(\frac{\partial^2}{\partial r^2} + \frac{1}{r}\frac{\partial}{\partial r} - \frac{1}{r^2} + \frac{\partial^2}{\partial z^2}\right)\psi^{(n)}$ given that $\boldsymbol{\psi}^{(n)} = \psi^{(n)}\mathbf{e}_\varphi$.

waves that travel perpendicular to the interface, as shown in Fig. 2.2. When $\kappa \geq k_{l,n}$, longitudinal wave propagation ceases and the resulting evanescent field decays exponentially with distance. Similarly, shear wave propagation becomes evanescent when $\kappa \geq k_{t,n}$. Because $\kappa_{l,n}$ and $\kappa_{t,n}$ both involve square roots of complex functions, there are four possible roots that satisfy Eqs. (2.40) and (2.41), respectively. The root which describes the correct physics (i.e., exponential decay from the interface) is when $\mathrm{Re}\{\kappa_{l,n}\} \geq 0$ and $\mathrm{Im}\{\kappa_{l,n}\} \leq 0$.[†] The same branch is chosen for $\kappa_{t,n}$.

The general solutions defined for the potential functions in the angular spectrum domain are used in the boundary-condition equations formulated in Section 2.3.1. We can also use them to define expressions for the Green's function in the angular-spectrum domain, where the non-zero components are given by

$$G_r^{(n)} = i\left(\kappa\Phi^{(n)} + \frac{\partial}{\partial z}\Psi^{(n)}\right), \tag{2.46}$$

$$G_z^{(n)} = \frac{\partial}{\partial z}\Phi^{(n)} + \kappa\Psi^{(n)}, \tag{2.47}$$

where Eq. (2.46) is multiplied by $-i$ to equate the Hankel transform [Eq. (2.34)] with the original spatial Fourier transform in Cartesian coordinates.[‡] Because of the Dirac delta function in Eq. (2.36), we consider this problem to have two boundaries: (1) the solid-liquid interface at $z = 0$, and (2) the source plane

[†]Stipulations on the imaginary part of $\kappa_{l,n}$ are determined by how we defined our temporal Fourier transform pair in Eqs. (2.21) and (2.22). The convention used for this transform pair is similar to assuming an $e^{-i\omega t}$ time dependence.

[‡]Similar to Eq. (7) of Hay et al.[2]

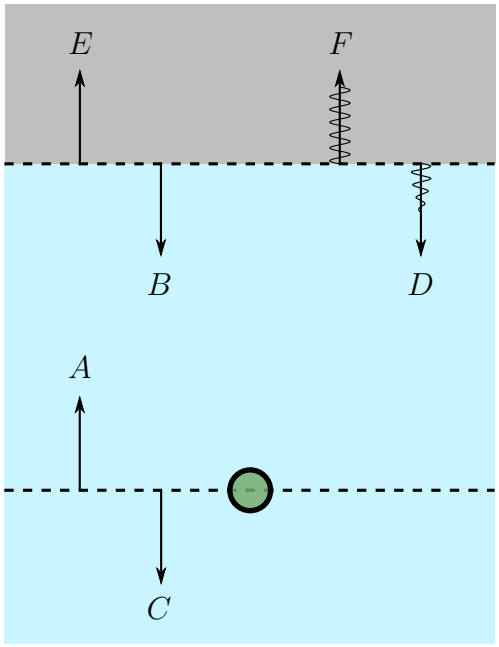

Figure 2.2: Directions of wave propagation and corresponding complex amplitude coefficients.

parallel to the solid-liquid interface at $z = -z_0$. The Dirac delta function is thus incorporated in the boundary condition for the source plane, rendering the ordinary differential equation homogeneous. This methodology is standard in solving many Green's function problems.[†]

2.3.1 Interface boundary conditions

At the liquid-solid interface we require continuity of displacement and stress. Because the Green's function is acting as the solution for our displace-

[†]Pages 22–24 of Duffy.[58]

ment field, we treat it as such. Hence, at the liquid-solid interface the radial component of displacement in the fluid, Eq. (2.29) with $n = 1$, must be equal to the radial component of the displacement in the solid, Eq. (2.29) with $n = 2$, giving

$$\frac{\partial}{\partial r}\phi^{(1)} - \frac{\partial}{\partial z}\psi^{(1)} = \frac{\partial}{\partial r}\phi^{(2)} - \frac{\partial}{\partial z}\psi^{(2)} \quad \text{at} \quad z = 0\,,$$

which in the angular-spectrum domain becomes[†]

$$-\kappa\Phi^{(1)} - \frac{\partial}{\partial z}\Psi^{(1)} = -\kappa\Phi^{(2)} - \frac{\partial}{\partial z}\Psi^{(2)} \quad \text{at} \quad z = 0\,,$$

using the relation $\mathcal{H}_1\left\{\partial\phi^{(n)}/\partial r\right\} = -\kappa\mathcal{H}_0\left\{\phi^{(n)}\right\}$.[63] Substitution of the general solutions for $\Phi^{(n)}$ and $\Psi^{(n)}$ [Eqs. (2.42)–(2.45)] into the previous equation gives

$$\kappa\,(A + B) + \kappa_{t,1}D = \kappa E - \kappa_{t,2}F\,. \tag{2.48}$$

Following an identical procedure, we impose continuity of normal displacement or, equivalently, continuity of the z component of the Green's function:

$$\frac{\partial}{\partial z}\phi^{(1)} + \frac{1}{r}\frac{\partial}{\partial r}\left(r\psi^{(1)}\right) = \frac{\partial}{\partial z}\phi^{(2)} + \frac{1}{r}\frac{\partial}{\partial r}\left(r\psi^{(2)}\right) \quad \text{at} \quad z = 0\,.$$

When expressed in terms of the general solutions and evaluated at the boundary $z = 0$, the previous expression yields

$$-\kappa_{l,1}\,(A - B) + \kappa D = -\kappa_{l,2}E + \kappa F\,. \tag{2.49}$$

[†]This expression does not match Eq. (2.46) because we have not multiplied the result by $-i$, which relates the Hankel transform of order one to the spatial Fourier transform.

Boundary conditions for the shear and normal stress components are derived in a similar manner and merely given here, where the derivation is performed in Appendix A. Continuity of shear stress yields

$$\beta_1 \kappa_{l,1} (A - B) - \alpha_1 D = \beta_2 \kappa_{l,2} E - \alpha_2 F \,, \tag{2.50}$$

and continuity of normal stress gives

$$\alpha_1 (A + B) + \beta_1 \kappa_{t,1} D = \alpha_2 E - \beta_2 \kappa_{t,2} F \,, \tag{2.51}$$

where

$$\alpha_n = \tilde{\mu}_n \left(\kappa^2 + \kappa_{t,n}^2 \right) \,, \tag{2.52}$$

$$\beta_n = 2 \tilde{\mu}_n \kappa \,. \tag{2.53}$$

2.3.2 Source boundary conditions

In the source plane we require continuity of the field variable $\Phi^{(1)}$, which is expressed mathematically by evaluating the field a distance ϵ above and below the source plane as $\epsilon \to 0$:

$$\lim_{\epsilon \to 0} \Phi^{(1)}(-z_0 + \epsilon) = \lim_{\epsilon \to 0} \Phi^{(1)}(-z_0 - \epsilon) \,.$$

Substitution of Eq. (2.42) into the preceding expression yields

$$A e^{\kappa_{l,1} z_0} + B e^{-\kappa_{l,1} z_0} - C e^{-\kappa_{l,1} z_0} = 0 \,. \tag{2.54}$$

The final source condition defines the discontinuity over the source plane of the first derivative of $\Phi^{(1)}$, which arises since two derivatives of $\Phi^{(1)}$ is proportional

to a spatial Dirac delta function [Eq. (2.36)]. The boundary condition is derived by integrating Eq. (2.36) over z from $-z_0 - \epsilon$ to $-z_0 + \epsilon$ in the limit as $\epsilon \to 0$, which simplifies to

$$\lim_{\epsilon \to 0} \frac{\partial}{\partial z} \Phi^{(1)}(z) \Big|_{z=-z_0-\epsilon}^{z=-z_0+\epsilon} = 1 \,. \tag{2.55}$$

The integration of the right-hand side of Eq. (2.36) is 1 since, by definition, that is the area under a delta function.[†] Substitution of Eq. (2.42) into Eq. (2.55) produces

$$A e^{\kappa_{l,1} z_0} - B e^{-\kappa_{l,1} z_0} + C e^{-\kappa_{l,1} z_0} = -\frac{1}{\kappa_{l,1}} \,, \tag{2.56}$$

and combining Eqs. (2.54) and (2.56) allows us to explicitly solve for the coefficient A:

$$A = -\frac{1}{2\kappa_{l,1}} e^{-\kappa_{l,1} z_0} \,. \tag{2.57}$$

This is the result for a free-space Green's function [Eq. (3.4.3) of Duffy.[58]], which is what the coefficient A represents since all energy traveling in its direction (toward the interface) must be produced by the source (i.e., the bubble).

2.3.3 Solving for the reverberant fields

Given that A is now known, we are able to solve Eqs. (2.48)–(2.51) for coefficient B, which is the principle coefficient needed to calculate the

[†]Equation (1.38) of Williams.[64]

fields affecting the bubble dynamics due to reflections from the interface. The coefficient B is written as

$$B = -\frac{(C_1 + C_2) - (C_3 - C_4)}{(C_1 + C_2) + (C_3 - C_4)} A \,, \tag{2.58}$$

where

$$\begin{aligned}
C_1 &= \left[(\beta_1 - \beta_2)\kappa_{l,2}\kappa_{t,1} - (\alpha_1 - \alpha_2)\kappa\right](\alpha_1 - \alpha_2)\kappa \,, \\
C_2 &= \left[(\beta_1\kappa - \alpha_2)\kappa_{t,1} + (\beta_2\kappa - \alpha_1)\kappa_{t,2}\right](\beta_2\kappa - \alpha_1)\kappa_{l,2} \,, \\
C_3 &= \left[(\beta_1\kappa - \alpha_2)\kappa_{t,1} + (\beta_2\kappa - \alpha_1)\kappa_{t,2}\right](\beta_1\kappa - \alpha_2)\kappa_{l,1} \,, \\
C_4 &= \left[(\beta_1 - \beta_2)\kappa_{l,2}\kappa_{t,1} - (\alpha_1 - \alpha_2)\kappa\right](\beta_1 - \beta_2)\kappa_{l,1}\kappa_{t,2} \,.
\end{aligned}$$

The details of this result can be found in Appendix B. In order to obtain results for all coefficients, it is easiest to write Eqs. (2.48)–(2.51) in matrix form and solve the linear system of equations numerically:

$$\begin{bmatrix} \kappa & \kappa_{t,1} & -\kappa & \kappa_{t,2} \\ \kappa_{l,1} & \kappa & \kappa_{l,2} & -\kappa \\ \alpha_1 & \beta_1\kappa_{t,1} & -\alpha_2 & \beta_2\kappa_{t,2} \\ \beta_1\kappa_{l,1} & \alpha_1 & \beta_2\kappa_{l,2} & -\alpha_2 \end{bmatrix} \begin{bmatrix} B \\ D \\ E \\ F \end{bmatrix} = \begin{bmatrix} -\kappa \\ \kappa_{l,1} \\ -\alpha_1 \\ \beta_1\kappa_{l,1} \end{bmatrix} A \,. \tag{2.59}$$

Once the coefficients are obtained, a solution for the displacement in the fluid is obtained by convolving the temporal Green's function for the fluid with the source function given in Eq. (2.9). This source function, however, is overly complicated for the problem at hand. One simplification is to evaluate the particle velocity of the fluid, instead of its displacement. This is achieved after taking a derivative with respect to time of Eq. (2.6), yielding

$$\left(\mathcal{L}_1 - \rho_1 \frac{\partial^2}{\partial t^2}\right) \dot{\mathbf{u}}_1 = K_1 Q(t) \boldsymbol{\nabla} \delta[\mathbf{x} - \mathbf{X}(t)] \,. \tag{2.60}$$

Reformulation of the entire problem in terms of velocity potentials yields identical boundary conditions. Thus, the solutions obtained for the displacement potentials are convolved with the derivative of the source function, $Q(t)\delta[\mathbf{x}-\mathbf{X}(t)]$, producing an expression for the velocity potential. We are interested in the reverberant pressure and its gradient, and obtain a temporal form of these quantities by convolving the new source function given here with the reverberant portion of the fluid scalar potential:

$$p_{\text{rev}} = -\rho_1 \frac{\partial}{\partial t} \int_{-\infty}^{\infty} \int_{\mathbf{X}_0} \phi_{\text{rev}}(t-\tau;\mathbf{x},\mathbf{X}_0)\, Q(\tau)\delta[\mathbf{X}_0-\mathbf{X}(\tau)]\; d\mathbf{X}_0 d\tau\,. \tag{2.61}$$

Variable ϕ_{rev} represents the portion of the fluid scalar potential that is propagating back onto the bubble due to the interface. Its angular spectrum is the term $Be^{\kappa_{l,1}z}$, originally defined in Eq. (2.42), and is expressed in the time domain after a spatial and temporal inverse transforms:

$$\begin{aligned}\phi_{\text{rev}}[t;\mathbf{x},\mathbf{X}(\tau)] &= \mathcal{F}_{\omega}^{-1}\left\{\frac{1}{2\pi}\mathcal{H}_0^{-1}\left\{\Phi_{\text{rev}}\right\}\right\} \\ &= \mathcal{F}_{\omega}^{-1}\left\{\frac{1}{2\pi}\int_0^{\infty} B(\mathbf{X}_0)\, e^{\kappa_{l,1}z} J_0(\kappa r)\kappa\, d\kappa\right\}\,. \end{aligned} \tag{2.62}$$

The convolution on the right-hand side of Eq. (2.61) thus represents the reverberant velocity potential, where a derivation of the relationship between the momentum equation used here, and that used to derive the Green's function, is given in Appendix C. Equation (2.61) is then simplified through the sifting property:[†]

$$p_{\text{rev}}[t,\mathbf{x}{=}\mathbf{X}(t)] = -\rho_1 \frac{\partial}{\partial t}\int_{-\infty}^{\infty} \phi_{\text{rev}}[t-\tau;\mathbf{x},\mathbf{X}(\tau)]\, Q(\tau)\, d\tau\,. \tag{2.63}$$

[†]Equation (1.37) of Williams.[64]

The calculation of the reverberant pressure is often performed numerically, where details of this calculation are explained in Chapter 3.

The reverberant portion of the vector potential $\psi^{(1)}$ is not included in the computation of the reflected pressure, or its gradient, since the fluid has no shear modulus, and it ultimately does not contribute to compression of the bubble. In addition, because all fields are axially symmetric, translation only occurs in the z direction (perpendicular to the interface). Thus, Eq. (2.62) is simplified by only considering the field at the bubble position along the z axis, i.e., $r = 0$ and $z = -z_b(t)$:

$$\phi_{\text{rev}} = \mathcal{F}_\omega^{-1}\left\{ \frac{1}{2\pi} \int_0^\infty B[-z_b(\tau)]\, e^{-\kappa_{l,1} z_b(\tau)} \kappa \, d\kappa \right\} . \tag{2.64}$$

Calculating the translation perpendicular to the interface requires the pressure gradient in the $\mathbf{e}_z$ direction, written as

$$\frac{\partial p_{\text{rev}}}{\partial z} = -\frac{\partial}{\partial t} \rho_1 \int_{-\infty}^\infty g_{\text{rev}}[t - \tau; \mathbf{x}, \mathbf{X}(\tau)]\, Q(\tau)\, d\tau \,, \tag{2.65}$$

where $g_{\text{rev}} = \partial \phi_{\text{rev}} / \partial z$, which is obtained in a similar manner to ϕ_{rev}:

$$\begin{aligned} g_{\text{rev}} &= \mathcal{F}_\omega^{-1}\left\{ \frac{1}{2\pi} \int_0^\infty \frac{\partial}{\partial z} B(\mathbf{X}_0)\, e^{\kappa_{l,1} z} J_0(\kappa r) \kappa \, d\kappa \right\} \Bigg|_{\mathbf{X}_0 = \mathbf{X}(\tau)} \\ &= \mathcal{F}_\omega^{-1}\left\{ \frac{1}{2\pi} \int_0^\infty \kappa_{l,1} B[-z_b(\tau)]\, e^{-\kappa_{l,1} z_b(\tau)} \kappa \, d\kappa \right\} . \end{aligned} \tag{2.66}$$

We refer to g_{rev} as the transfer function for the reverberant pressure gradient and always consider it to be evaluated at the center of the bubble [$\mathbf{x} = \mathbf{X}(t)$]. Equation (2.65) is the contribution of the reflections from the interface onto

the bubble in Eq. (2.2). For a free response (no external driving source) it is the only pressure gradient within the fluid accounted for in the model. This dissertation focuses on the reverberant pressure gradient since it is the term involved in describing bubble translation.

In summary, computation of the reverberant fields within the fluid is somewhat arduous. First, an analytical form of the angular spectrum of the reverberant fields within the fluid is obtained by solving the boundary-condition equations at the liquid-solid interface for the coefficient B. This coefficient is then combined with the reverberant portion [the portion multiplied by the coefficient B in Eq. (2.42)] of the general solution of the scalar potential defining the fluid Green's function. A time domain signal of the scalar potential associated with the reverberant pressure is obtained after integration in both the angular-spectrum and frequency domains, and convolution of this result with the volume velocity of the source at its current location yields the reverberant portion of the velocity potential in the fluid. Both the reverberant pressure and its gradient are then related to the reverberant velocity potential and substituted into the bubble dynamics equations, Eqs. (2.1) and (2.2).

2.4 Half-Space Assumption

While the theory developed in Sections 2.2 and 2.3 assumes that both the liquid and the viscoelastic solid are infinite in extent, actual experiments involve finite layers.[1,3,65] Thus, it is important to know at what thickness the viscoelastic layer may be approximated as a half-space—the thickness at

which the analysis here is comparable to experiments. Figure 2.3 shows the (a) magnitude and (b) phase of $\widehat{g}_{\text{rev}}(\omega)$ at a distance of 22.5 μm from the interface between the water and the a of the viscoelastic layer nearest to the bubble. The spectra are normalized with the corresponding spectra for an image source which is in phase with the bubble dynamics, derived in Appendix D [Eq. (D.5)]:

$$\begin{aligned}\widehat{g}_{\text{im}} &= -\frac{\partial}{\partial z}\frac{e^{i\omega D/c_1}}{4\pi D} \\ &= \left(i\frac{\omega}{c_1} - \frac{1}{D}\right)\frac{e^{i\omega D/c_1}}{4\pi D}\,, \end{aligned} \tag{2.67}$$

where $D = z_0 - z$, and we evaluate the field at the source location $z = -z_0$. The material properties for the fluid are those for water and the viscoelastic layer is assigned values similar to those for tissue. The specific values for both the fluid and the tissue-like solid are listed in Table 2.1. The theory used to calculate $\widehat{g}_{\text{rev}}(\omega)$ for a viscoelastic layer is given by Hay et al.[2] As the thickness of the layer exceeds about 1 mm, we note that all of the undulations in the spectra disappear, and the spectrum converges to that obtained assuming a half-space. The thicknesses used by others is generally larger than this

	Water	Viscoelastic layer
Density (kg/m^3)	998	1012
Speed of sound (m/s)	1484	1518
Shear modulus (Pa)	0	5666
Shear viscosity (Pa·s)	10^{-3}	1.5×10^{-3}
Bulk viscosity (Pa·s)	0	0

Table 2.1: Material properties of water and the viscoelastic layer used to calculate $\widehat{g}_{\text{rev}}(\omega)$ shown in Fig. 2.3.

value.[1,2] Further, for low-amplitude bubble pulsation the only relevant portion

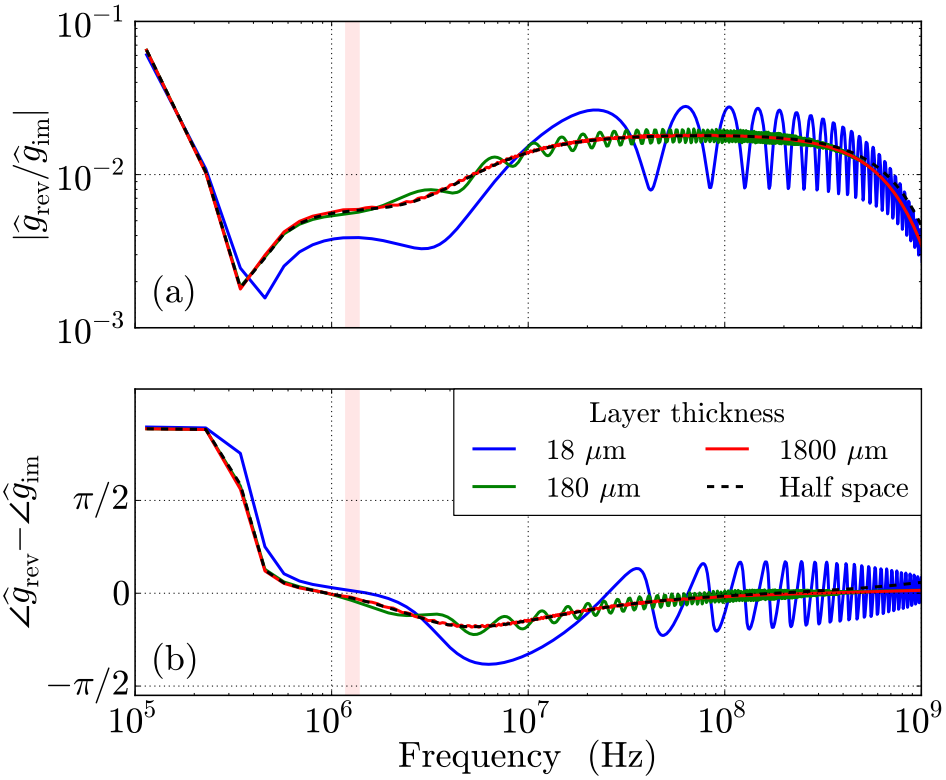

Figure 2.3: The (a) magnitude and (b) phase of $\widehat{g}_{\mathrm{rev}}(\omega)$, normalized by the corresponding spectrum for an image source [Eq. (2.67)], calculated a distance $22.5\,\mu$m ($7.5R_0$ for $R_0 = 3\,\mu$m) from the viscoelastic layer. The material properties for the fluid are water and those for the viscoelastic layer are tissue-like, where specific values are listed in Table 2.1. The theory used to calculate the spectra from a viscoelastic layer is given by Hay et al.[2]

of the spectra is near the oscillation frequency of the bubble, where the natural oscillation frequency for a bubble of radius $3\,\mu$m (a common bubble radius used throughout this dissertation) is denoted by the region of the axes in Fig. 2.3 shaded in pink. The frequency spectra are evaluated at frequencies much higher than the natural oscillation frequency of the bubble to resolve

numerically in time the very small distance between the interface and the bubble center. While the spectra can vary in phase and amplitude for different distances from the interface, or for different fluid and solid material properties, the undulations are not significant enough to wildly alter the physics gleaned from the half-space approximation considered here. However, we note that this assumption must be evaluated on a case-by-case basis since the bubble size and distance from the interface will change how thick the layer must be such that its corresponding spectrum is similar to that for a half space.

2.5 Conclusion

This chapter introduced the fundamental nonlinear equations used to model the dynamics of a spherical bubble immersed in a viscous fluid and near a viscoelastic solid. A Rayleigh-Plesset type equation was used to describe the bubble pulsation, and was coupled to a momentum equation describing bubble translation. The effects due to the fluid-solid interface affecting bubble pulsation and translation were included as terms in the bubble dynamics equations as a reverberant pressure and a reverberant pressure gradient, respectively. These terms were obtained via a Green's function method. The Green's function accounts for elastic wave propagation in the solid, and viscosity in both the liquid and the solid. An explicit analytical expression for the angular spectrum of the reverberant fields was derived for an arbitrary viscous fluid and viscoelastic solid, where temporal expressions of these fields are generally obtained numerically.

This chapter also justified the use of a viscoelastic half-space to approximate the viscoelastic layers used in experiments. This simplification greatly reduces the complexity of the problem, and helps to focus on the pertinent physics of the problem at hand. It was shown that the half-space approximation is valid when the layer has tissue-like properties and its thickness is greater than a few millimeters. This is often the case for the experiments with which we compare.[1,2]

Chapter 3

Numerical Implementation

The focus of this chapter is on the details of numerical implementation of the bubble dynamics equations. The first step will be to outline the nondimensionalization parameters used for these equations; the small bubble size and its corresponding large natural frequency make this step imperative. Next, a simplified numerical implementation of the problem is considered where the bubble is assumed to be in free space. Last, the many details involved in numerically calculating the reverberant fields are addressed. The bubble dynamics equations are temporal differential equations, and are solved for using a Green's function method. However, the Green's function is only expressed analytically in the angular-spectrum domain. Thus, integration over both the angular frequency ω and the wavenumber κ must be performed to obtain a temporal Green's function, with which we can simulate the bubble dynamics equations [Eqs. (2.1) and (2.2)]. By accounting for bubble translation in the model, the Green's function must be recalculated each time the bubble moves. Therefore, it is of interest to explore possible alternatives to this procedure.

Analytical treatment of moving sources has previously been given much attention.[34,40,42,66–69] In order to evaluate the fundamental equations, how-

ever, simplifications are often required. The two most common simplifications are a constant-velocity source,[40,42,66–68] and describing the object in motion as a Dirac delta function in space.[40,42,66,67] Assuming a constant-velocity source is generally acceptable because the end application is commonly aeroacoustics or underwater acoustics. In this dissertation, however, this assumption may not be appropriate due to the lurching motion of a bubble during collapse and rebound. Fortunately, we are able to describe the bubble as a spatial Dirac delta function which changes its spatial location as a function of time.

Works relying more heavily on numerical calculations to approximate the field produced by a moving source are also ubiquitous.[36–39,41] However, most of the work involving this problem assumes a free-space Green's function which greatly simplifies the numerical computation. The work done by Schmidt et al.[38] is similar to the method employed in this dissertation, in that the field calculated for the moving source is affected by a nearby layer. However, the movement of the source considered by Schmidt et al.[38] is always considered to be parallel to the interface, changing the numerical approach entirely. Numerically, the work presented here is most similar to that of Sabra et al.[36,37]

3.1 General Numerical Implementations

Before delving into the details of the numerical implementation of the reverberant pressure gradient, we focus on some of the generalities common to many different calculations.

3.1.1 Nondimensionalization

A requisite procedure for numerical accuracy for problems with both large and small scales is nondimensionalization of the expressions at hand. Because the typical bubble of interest is only a few microns large, the natural resonance frequency of the bubble is around a megahertz. The inverse relationship between the length scale of the bubble size and the frequencies of oscillation can cause inaccuracies in the numerical simulations. In addition, the spectrum of the Green's function includes frequencies much higher than the resonance frequency of the bubble. Under these circumstances, nondimensionalization is imperative.

For these simulations, we choose the length scale to be the equilibrium bubble radius R_0 and the time scale to the period of natural oscillation frequency for linear pulsation,

$$T_0 = \frac{2\pi}{\omega_0}\,, \tag{3.1}$$

where ω_0 is natural oscillation frequency of the bubble in free space. The term used to nondimensionalize pressure is a consequence of the chosen time and length scales, given to be $\rho_1 R_0^2/T_0^2$.

We solve the nondimensional versions of Eqs. (2.1) and (2.2) for $\ddot{R}$ and $\ddot{X}$, respectively. This coupled set of equations is then solved numerically by employing a standard numerical integration scheme. The simulations performed in this dissertation employ the FORTRAN version of the CVODE

package for both the integration of the bubble dynamics equations and the inverse spatial transform of the angular spectrum of the Green's function.[70]

3.1.2 Free field dynamics

This first and simplest case to implement numerically is to neglect the interface, assuming the bubble pulsates and translates in free space. For this case, it is not necessary to compute the reverberant fields p_{rev}, $\boldsymbol{\nabla} p_{\text{rev}}$, and $\mathbf{u}_{\text{rev}}$ in Eqs. (2.1) and (2.2). We describe the pressure from the drive source as a sinusoidal plane wave,

$$p_{\text{src}} = A_d \sin\left[\omega_d \left(t - x/c_1\right)\right] , \tag{3.2}$$

where c_1 is the compressional wave speed in the liquid after neglecting viscosity, A_d is the amplitude of the drive source, and ω_d is the frequency at which the bubble is driven. For numerical reasons, we gate the sine wave with a sigmoid function, defined as

$$W(t) = \frac{1}{e^{-\chi\omega_d(t-x/c_1)} + 1} , \tag{3.3}$$

where χ defines how quickly the sigmoid function changes from zero to one. Hence, the value of the source pressure at the bubble location is given by

$$p_e = p_{\text{src}}(X)\left[W(t) - W(t-T)\right] , \tag{3.4}$$

where T is the time at which the source turns off, and the source function is spatially evaluated at the center of the bubble, $x = X$, as Eqs. (2.1) and (2.2)

are numerically integrated. The pressure gradient along the x axis of the first term on the right-hand side of Eq. (3.4) is

$$\frac{\partial}{\partial x}\left(p_{\mathrm{src}}W\right) = -W\frac{\omega_d}{c_1}\left\{A_d\cos\left[\omega_d\left(t-x/c_1\right)\right] + \chi e^{-\chi\omega_d(t-x/c_1)}p_{\mathrm{src}}W\right\}\ . \quad (3.5)$$

3.1.3 Nonlinear free-field simulation

Figure 3.1 shows the radial pulsation and translation for a typical simulation of a nonlinearly oscillating and translating bubble of radius 3 μm in free space, driven by an external source. The drive source is a 5-cycle gated sinusoid, defined by Eq. (3.4) where $T = 5$, $A_d = 5P_0$, $\chi = 2.5$, and $\omega_d = \omega_0$. The maximum value of the bubble radius, induced by the drive source, is large in this simulation and the radial oscillations are highly nonlinear. The bubble collapse occurs during a region of time where the bubble radius quickly falls from being several equilibrium radii to a local minimum. The translational dynamics are coupled to the radial pulsation such that collapse corresponds to moments of high translational velocity and acceleration. During these times, the bubble can be seen to quickly accelerate in the direction of the pressure gradient. The translational motion then comes to an equally abrupt stop as the bubble radius begins to expand again. Although the bubble trajectory contains regions of high translational velocity and acceleration, the amount of translation in between each collapse is very small. It is during these periods of little movement where most of the simulation takes place. Thus, even though the computation of the reverberant fields requires a recalculation of the Green's function, Fig. 3.1 shows promise that much of the simulation can be simplified

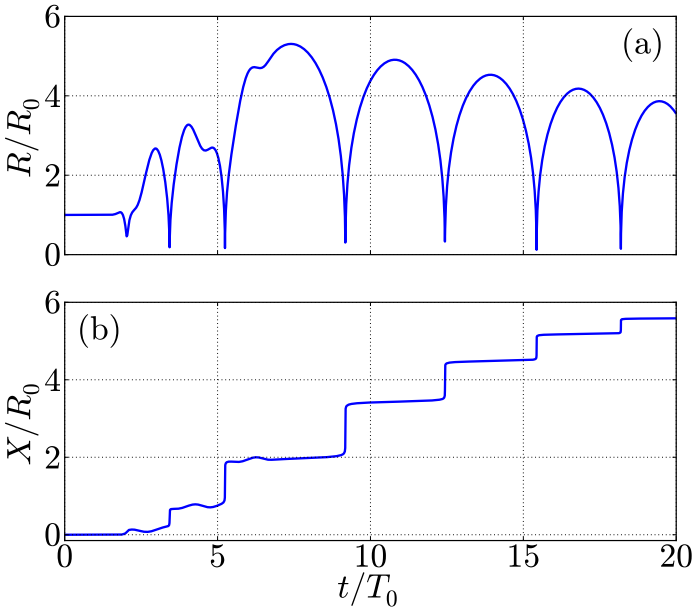

Figure 3.1: Simulations of bubble (a) pulsation and (b) translation for a bubble of radius $3\,\mu$m in free space. The bubble is excited by a five-cycle, gated sine wave with a $5P_0$ pressure amplitude.

by assuming a stationary bubble to compute the Green's function—during times where bubble translation is minimal.

3.2 Reverberant Fields

As shown in Section 2.3.3, the analytical representation of the reverberant pressure and its gradient involves two inverse transforms: (1) an inverse spatial transform and (2) an inverse temporal transform. Generally, these operations cannot be performed analytically and are therefore computed numerically. The details for numerical implementation of each of these inverse transforms are given here.

3.2.1 Angular-spectrum domain

Before obtaining the spectra of the reverberant pressure and its gradient in spatial coordinates, we first perform an inverse spatial transform. As with the bubble dynamics equations, we also nondimensionalize this operation. In the angular-spectrum domain we nondimensionalize the wavenumber variables κ, $\kappa_{l,n}$, and $\kappa_{t,n}$ with

$$k_0 = \frac{\omega_0}{c_1} .$$

For example, the nondimensional form of $\kappa_{l,1}$ is

$$\frac{\kappa_{l,1}}{k_0} = \sqrt{\left(\frac{\kappa}{k_0}\right)^2 - \frac{(\omega/\omega_0)^2}{1 - i\omega\left(\frac{2\eta_1+\zeta_1}{\rho_1 c_1^2}\right)}} , \tag{3.6}$$

where κ/k_0 is the new nondimensional angular-spectrum variable, and ω is put in terms of ωT_0, the nondimensional angular frequency. Using this nondimensionalization parameter in conjunction with those defined in Section 3.1.1, the nondimensionalization of the inverse spatial transform for the reverberant scalar potential yields the form given in Eq. (2.62) (except that all of the variables are now nondimensional), multiplied by k_0:

$$\widehat{\phi}_{\text{rev}} = \frac{k_0}{2\pi}\mathcal{H}^{-1}\left\{\Phi_{\text{rev}}\right\} , \tag{3.7}$$

where the nondimensional angular spectrum is $\Phi_{\text{rev}} = k_0 B e^{\kappa_{l,1} z}$. The nondimensionalization of quantities involving both a spatial and an angular-spectrum variable (i.e., the product $\kappa_{l,1} z$) result in the quantity $k_0 R_0$ after nondimensionalization. This quantity helps maintain numerically calculations

near unity and is thus desirable in nondimensionalized expressions. This is achieved, for example, in Eq. (3.7) by expressing the left-hand side as a nondimensional version of $\widehat{\phi}_{\text{rev}}$ divided by R_0 and then solving for the nondimensional $\widehat{\phi}_{\text{rev}}$. This identical procedure may be performed to obtain a nondimensional form of $\widehat{g}_{\text{rev}} = \partial\widehat{\phi}_{\text{rev}}/\partial z$ used to compute the reverberant pressure gradient, which results in the form given in Eq. (2.66) multiplied by $(k_0 R_0)^2$.

The final detail for numerical integration is determining an upper bound of integration. This value may be drastically different for different locations from the interface. However, we are only interested in the field inasmuch as it affects the bubble. Thus, evaluating Eq. (3.7) at the bubble center $(0,0,-z_0)$ is the sole location of interest. Thus, we evaluate the integrand of the inverse spatial transform of $\widehat{g}_{\text{rev}}(\omega_0)$ to determine an upper bound of integration.

Figure 3.2 plots the (a) magnitude and (b) phase of the integrand of the inverse spatial transform of $\widehat{g}_{\text{rev}}(\omega_0)$ for an interface between water and a tissue-like solid at varying distances from the interface. The specific material properties for the water and the solid are given in Table 3.1. The vertical dashed lines labeled L_1 and L_2 near $\kappa/k_0 = 1$ represent where κ is equal to the real part of the longitudinal wavenumbers $k_{l,1}$ and $k_{l,2}$, respectively. The line labeled L_3 shows where κ is equal to the real part of the transverse wavenumber $k_{t,2}$; we do not show a line where κ is equal to the real part of $k_{t,1}$ since transverse wave propagation in the fluid is always evanescent. Lines L_1, L_2, and L_3 help to decipher when the interaction at the interface generates a field potential that either propagates or decays exponentially from

	Fluid	Solid
Density (kg/m^3)	998	1030
Speed of sound (m/s)	1484	1580
Shear modulus (Pa)	0	10^6
Shear viscosity (Pa·s)	10^{-3}	1.5×10^{-3}
Bulk viscosity (Pa·s)	3.09×10^{-3}	0

Table 3.1: Material properties assigned to the fluid and tissue-like solid during calculation of the integrand of $\mathcal{H}_0^{-1}\{G_{\text{rev}}\}$ [Eq. (2.66)] shown in Fig. 3.2. The fluid is assigned values for water, while the viscoelastic solid is given tissue-like properties.

the interface. For example, we recall [Eq. (2.40)] that

$$\kappa_{l,n} = \sqrt{\kappa^2 - k_{l,n}^2}\,, \tag{3.8}$$

which for values where $\kappa < \text{Re}\{k_{l,n}\}$ is almost entirely imaginary (since $k_{l,n}^2$ is almost entirely real) and corresponds to a compressional wave which propagates in the n^{th} medium. When $\kappa > \text{Re}\{k_{l,n}\}$, however, Eq. (3.8) is mostly real and therefore corresponds to a compressional wave whose amplitude decays exponentially in the n^{th} medium. This same analysis is also true for the wavenumbers corresponding to shear waves $\kappa_{t,n}$, but the shear component in the fluid admits a large amount of evanescent decay for all κ since $k_{l,1}^2$ is imaginary. Significant decay of the entire spectrum is observed after the longitudinal waves in both media, and the transverse wave in the viscoelastic medium, are evanescent ($\kappa > |k_{l,1}|, |k_{l,2}|, |k_{t,2}|$). The line labeled L_4 corresponds to a minimum in the denominator of the coefficient B [Eq. (2.58)]. For a liquid-solid interface without viscosity, this minimum is consistent with one of the roots of the characteristic equation defining interface waves [see, e.g., Eq. (15) of

Zhu et al.[61]]. Because this peak occurs in a region where evanescent decay is expected for both compressional and shear waves in the fluid and the solid, the wave is confined to the surface and is likely the Scholte wave. Another

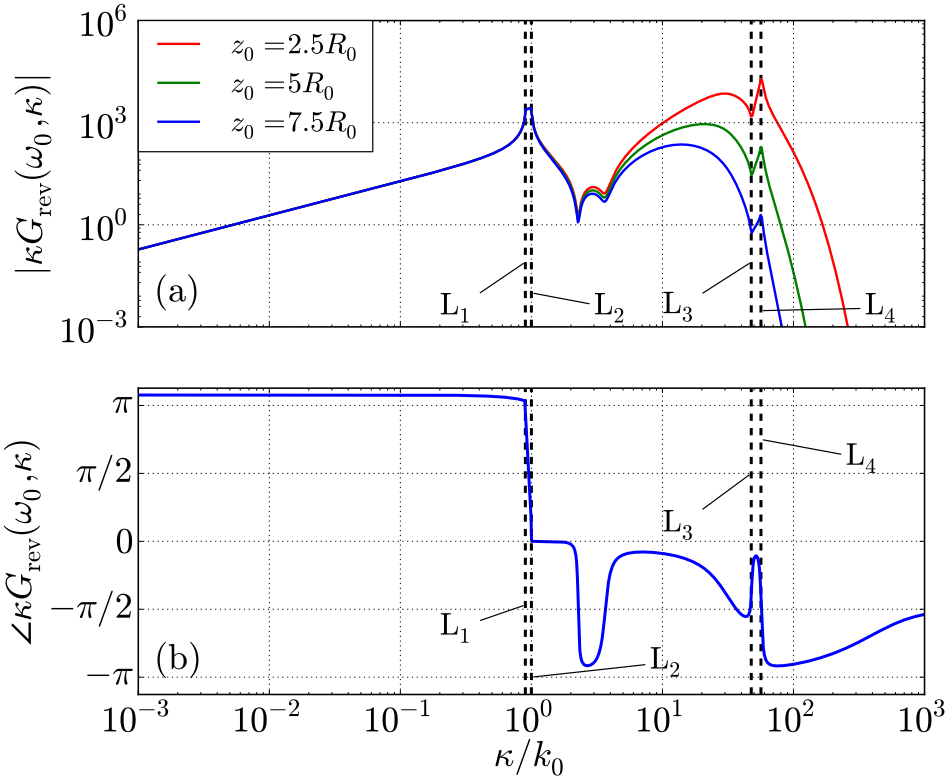

Figure 3.2: The (a) magnitude and (b) phase of the integrand of $\mathcal{H}_0^{-1}\{G_{\mathrm{rev}}\}$ for an interface between water and a tissue-like solid, evaluated along the z axis at distances from the interface ranging from $2.5R_0$ to $7.5R_0$ for $R_0 = 3\,\mu$m. The vertical, dashed lines labeled L_1, L_2, and L_3 indicate where $\kappa = \mathrm{Re}\{k_{l,2}\}$, $\mathrm{Re}\{k_{l,1}\}$, and $\mathrm{Re}\{k_{t,2}\}$, respectively. Line L_4 represents a minimum in the denominator of the coefficient B [Eq. (2.58)]. Specific material parameters for both water and the viscoelastic medium are given in Table 3.1.

feature to recognize is the small region of constant amplitude in between lines

L_1 and L_2. This region represents the angles at which total internal reflection occurs, and only occurs for angles nearly grazing the surface of the interface since the compressional wave speed in the fluid and the tissue-like solid are nearly similar. This is more easily seen in Fig. 3.3.

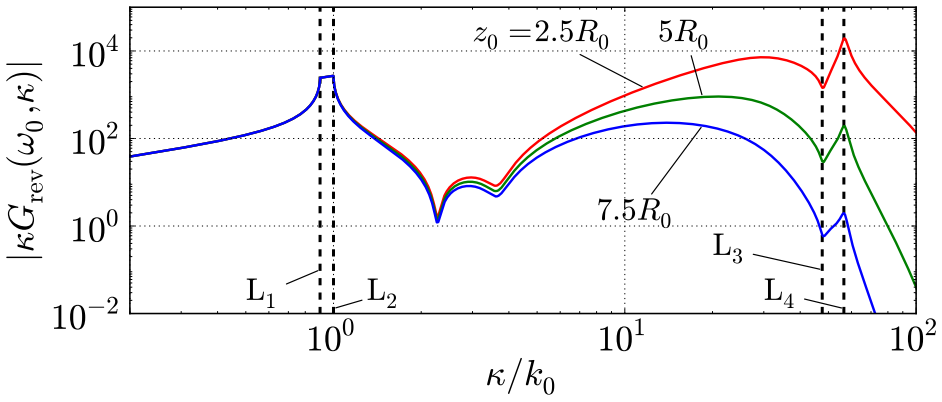

Figure 3.3: A closeup of the magnitude of the integrand of $\mathcal{H}_0^{-1}\{G_{\text{rev}}\}$ shown in Fig. 3.2. As in Fig. 3.2, the vertical dashed lines labeled L_1, L_2, and L_3 indicate where $\kappa = \text{Re}\{k_{l,2}\}$, $\text{Re}\{k_{l,1}\}$, and $\text{Re}\{k_{t,2}\}$, respectively. Line L_4 represents a minimum in the denominator of the coefficient B [Eq. (2.58)].

The amount of evanescent decay in the reverberant field is highly dependent on the distance of the bubble from the interface, which explains the wide range in amplitudes between the magnitude of the spectra shown in Figs. 3.2 and 3.3 for $\kappa/k_0 > 1$; the magnitude of the spectrum at distance $7.5\,\mu$m from the interface ($2.5R_0$ for $R_0 = 3\,\mu$m) contains a much greater magnitude compared to the corresponding magnitude at distance $22.5\,\mu$m from the interface ($7.5R_0$). In addition, the phase of the integrand of $\mathcal{H}_0^{-1}\{G_{\text{rev}}\}$, shown in Fig. 3.2(b), does not vary as the distance from the interface is changed.

Last, because the magnitude of the spectrum is insignificant for $\kappa/k_0 > 1000$, numerical integration is only required to this point. This limit was sufficient for the vast majority of cases we evaluated, while the maximum value for κ/k_0 was typically set at a value of around 1900. The inverse spatial transform is performed using the FORTRAN version of the CVODE package,[70] a standard backwards-differentiation routine.

3.2.2 Frequency domain

With the quantities $\widehat{\phi}_{\text{rev}}(\omega)$ and $\widehat{g}_{\text{rev}}(\omega)$ calculated, we outline the steps required to express the reverberant pressure and its gradient in the time domain. Because these reverberant fields are ultimately calculated via a convolution [Eqs. (2.63) and (2.65)], there is some freedom in the numerical approach. For a stationary source, a convolution is generally performed in one of two ways: (1) by explicit evaluation of the convolution integral in the time domain, or (2) by multiplication of the spectra in the frequency domain. Because the reverberant fields are only needed at the current time, the first method is computationally more efficient than the second.[2]

When the bubble moves, however, the methods used to calculate the reverberant fields produced by a stationary bubble are inaccurate. Implementation of the first method with a moving source can be inaccurate since the Green's function may be significantly altered at each time step. While several Green's functions may be calculated, this approach would then involve skipping between Green's functions—computing entire time series of data for each

Green's function when only a few time steps are necessary before moving the next Green's function. Additionally, the second method does not help with simplification since the source function is composed of two functions that depend on time. The transform of this source function involves a convolution in the frequency domain between the spectra of the volume velocity and bubble translation, with the additional complication of the variable bubble location being embedded within the Green's function. Thus, the simplest approach is to keep the volume velocity and bubble translation as functions of delay time τ, while transforming the Green's function into the frequency domain. Mathematically, this is achieved by taking temporal Fourier transforms of Eqs. (2.63) and (2.65):

$$\widehat{p}_{\text{rev}} = i\omega\rho_1 \int_{-\infty}^{\infty} \widehat{\phi}_{\text{rev}}[\omega, \mathbf{X}(\tau)]\, Q(\tau) e^{i\omega\tau}\, d\tau\,, \tag{3.9}$$

$$\frac{\partial \widehat{p}_{\text{rev}}}{\partial z} = i\omega\rho_1 \int_{-\infty}^{\infty} \widehat{g}_{\text{rev}}[\omega, \mathbf{X}(\tau)]\, Q(\tau) e^{i\omega\tau}\, d\tau\,. \tag{3.10}$$

If the source is stationary, then $\widehat{\phi}_{\text{rev}}$ and $\widehat{g}_{\text{rev}}$ can be removed from the integrands in Eqs. (3.9) and (3.10), respectively, and by definition the remaining integrals both become the spectrum of the volume velocity. Because we allow the source to move, however, these quantities depend on the integration variable cannot be removed. The form of Eqs. (3.9) and (3.10) are somewhat ideal, since we do not transform the volume velocity or translation of the bubble and can use the spectrum of the Green's function before performing an inverse Fourier transform. The reverberant fields may then be calculated by

performing an inverse Fourier transform at only the current time t_c,

$$p_{\text{rev}}(t_c) = \frac{1}{2\pi}\int_{-\infty}^{\infty} \widehat{p}_{\text{rev}} e^{-i\omega t_c}\, d\omega\,. \tag{3.11}$$

In order to use Eqs. (3.9) and (3.10) in the numerical simulations, they are represented as discrete sums for the numerical calculation as

$$\widehat{p}_{\text{rev}} = i\omega\rho_1\Delta t \sum_{k=t_i}^{t_c} \widehat{\phi}_{\text{rev}}[\omega, \mathbf{X}(t_k)]\, Q(t_k) e^{i\omega t_k}\,, \tag{3.12}$$

$$\frac{\partial \widehat{p}_{\text{rev}}}{\partial z} = i\omega\rho_1\Delta t \sum_{k=t_i}^{t_c} \widehat{g}_{\text{rev}}[\omega, \mathbf{X}(t_k)]\, Q(t_k) e^{i\omega t_k}\,, \tag{3.13}$$

where Δt represent the time step $t_{k+1} - t_k$ and the summation spans from an initial time t_i to the current simulation time t_c. Additionally, in the frequency domain the delay time τ is the only explicit temporal variable and is thus replaced with variable t for clarity. At each new time step the spectra for the reverberant fields are calculated by adding the effects from the current time. For example, to calculate the reverberant pressure initially, we multiply the initial values for the volume velocity with $\widehat{\phi}_{\text{rev}}$:

$$\widehat{p}_{\text{rev}}(t_0) = i\omega\rho_1\Delta t \widehat{\phi}_{\text{rev}}[\omega, \mathbf{X}(t_0)]\, Q(t_0) e^{i\omega t_0}\,,$$

where t_0 is the first time step of the simulation. Computation of the next time step merely involves adding the effects from the current time, since

$$\begin{aligned}\widehat{p}_{\text{rev}}(t_1) &= i\omega\rho_1\Delta t \left\{ \widehat{\phi}_{\text{rev}}[\omega, \mathbf{X}(t_0)]\, Q(t_0) e^{i\omega t_0} + \widehat{\phi}_{\text{rev}}[\omega, \mathbf{X}(t_1)]\, Q(t_1) e^{i\omega t_1} \right\} \\ &= \widehat{p}_{\text{rev}}(t_0) + i\omega\rho_1\Delta t \widehat{\phi}_{\text{rev}}[\omega, \mathbf{X}(t_1)]\, Q(t_1) e^{i\omega t_1}\,,\end{aligned} \tag{3.14}$$

where t_1 is the second step of the simulation. Thus, at each time step the reverberant fields are calculated by adding the effects from the current time to the existing spectra and then computing a one-point inverse Fourier transform at the current time step.

The downside to computing the reverberant pressure and its gradient in this way is that we maintain the simulation history in the frequency domain; therefore, the maximum simulation time is

$$t_{\max} = \frac{N}{f_{\max}}\,, \tag{3.15}$$

where N is the number of discrete frequencies in the spectrum and $f_{\max}$ is the maximum frequency at which the spectra are computed. For $t > t_{\max}$, the temporal solution will alias and the results are no longer valid. Hence, computing the spectrum of the Green's function becomes increasingly more time consuming for longer simulation times since we require a larger N.

3.3 Numerical Simplifications

If the simulation is performed by calculating the reverberant fields as described by Eqs. (3.12) and (3.13), a large portion of the computation time is used to recompute the Green's function at each time step. An illustrative example is helpful to understand this point; imagine that the evolution of the bubble is simulated as given in Fig. 3.4. In this figure the green bubble is the state of the bubble dynamics at the current simulation time. All white dashed bubbles to the left of the green bubble represent states of the bubble

at previous simulations times, while those to the right represent future states.

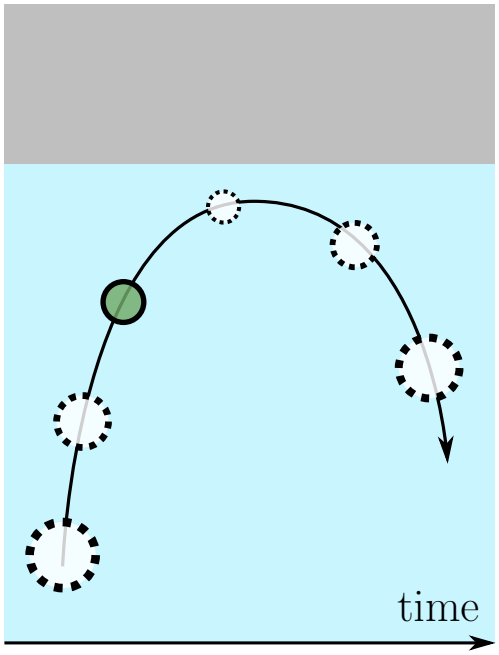

Figure 3.4: Cartoon of the bubble evolution where the current time step is represented by the green bubble, past dynamical values are drawn as white dashed circles to the left of the green bubble, and future values are to the right of the green bubble.

The process involved in calculating the bubble dynamics at the next time step requires the following three steps:

1. Calculating the spectrum of the Green's function for the given distance from the interface (involves bubble location X)

2. Computing the reverberant pressure at the current time (involves bubble pulsation parameters R and $\dot{R}$)

3. Using these values to compute the future bubble dynamics through numerical integration of the coupled differential equations (involves all bubble dynamics parameters: R, $\dot{R}$, X, and $\dot{X}$)

3.4 Simplifying the Green's Function Calculation

As seen in Fig. 3.1, there are several periods of relatively little translation, which occurs in between bubble collapses. Thus, there are many instances when the Green's function does not need to be recomputed. To express this simplification mathematically, we expand the Green's function about a stationary point in space X_m:

$$\widehat{g}_{\text{rev}}[\mathbf{X}(t)] = \widehat{g}_{\text{rev}}(\mathbf{X}_m) + [\mathbf{X}(t) - \mathbf{X}_m] \cdot \boldsymbol{\nabla}_{\mathbf{x}} \widehat{g}_{\text{rev}}[\mathbf{X}(t)] \Big|_{\mathbf{X}=\mathbf{X}_m} + \cdots , \qquad (3.16)$$

where $\mathbf{X}_m$ is a value chosen beforehand about which we perform the expansion, and $\boldsymbol{\nabla}_{\mathbf{x}}$ represents the gradient with respect to the bubble coordinates. By only using the first term in this expansion, translation is ignored in the Green's function—reducing it to the case of a stationary bubble at location $\mathbf{X}_m$. For a bubble near a rigid wall with a slip condition at its surface, the Green's function may be reduced to the first term on the right-hand side of Eq. (3.16) when $|\mathbf{X}(t) - \mathbf{X}_m| \ll z_0$, where in this case z_0 is the distance from point $\mathbf{X}_m$ to the interface. Figure 3.5 shows the proposed alterations to the calculation of the Green's function by choosing only a few locations for $\mathbf{X}_m$. As in Fig. 3.4, the past and future bubble dynamics are represented by the path white dashed bubbles, while the green bubble represents the current bubble dynamics. The

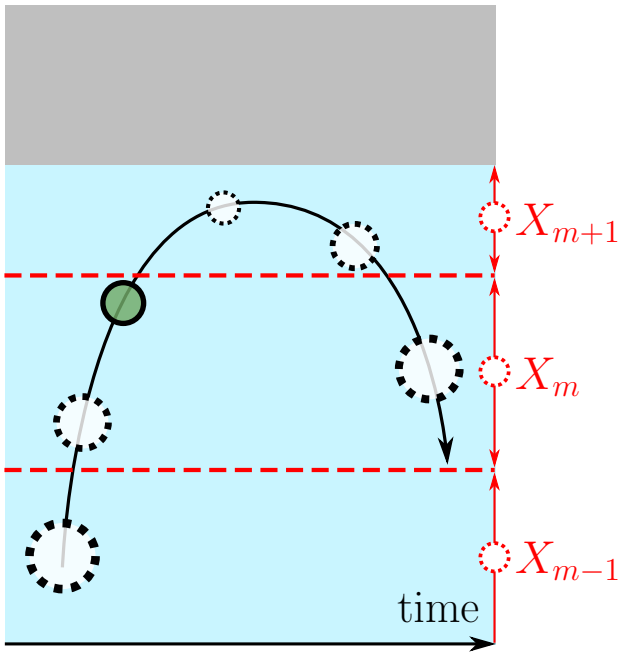

Figure 3.5: Alteration of Fig. 3.4 by using discrete locations of the bubble when calculating the Green's function. Each region is represented by the area encompassed between the red, dashed lines. For a bubble near a rigid wall with a slip condition at its surface, the Green's function may be reduced to the first term on the right-hand side of Eq. (3.16) when the distance between the bubble position and the expansion point, $|X(t) - X_m|$, is much smaller than the distance from X_m to the interface.

red, dashed lines represent the discretization of the bubble distance from the interface—used to compute the Green's function. In other words, the equations describing the bubble dynamics account for the movement of the bubble—with exception to the terms involving the reverberant fields, which are computed assuming a stationary bubble at position X_m on the z axis. Thus, for the duration of time that the actual bubble location remains inside the region

appertaining to the discrete point X_m, the same Green's function is reused. This simplification greatly decreases the amount of computation time required for each simulation.

The effect of this simplification is shown in Fig. 3.6. This figure shows three different simulations of a bubble of radius $3\,\mu$m immersed in water and initially located a distance $7.5R_0$ from a rigid interface and excited by a $3P_0$ amplitude sine wave. For this example, the excitation source travels parallel to the boundary and the associated primary Bjerknes force is ignored. In other words, translation toward the interface is solely due to the reverberant pressure gradient. The only difference between the simulations is the size of the discretization. The black curve shows the radial and translational dynamics when the Green's function is recomputed at every time step, and represents the most accurate computation of the reverberant fields within the bubble dynamics equations [Eqs. (2.1) and (2.2)]. The blue curve employs only one location (the initial location) of the bubble to compute the reverberant fields—regardless of the actual bubble location. The red curve uses two discrete bubble locations separated by $4R_0$. Hence, after the bubble has translated $2R_0$ (indicated by the red marker), the Green's function is recalculated in the middle of the next discrete region, a distance of $3.5R_0$ from the boundary for this example.

Simulations similar to those shown in Fig. 3.6 can take a very long time to compute when numerical integration of the angular-spectrum of the Green's function is required. For this reason, the simulations shown in Fig. 3.6 use the

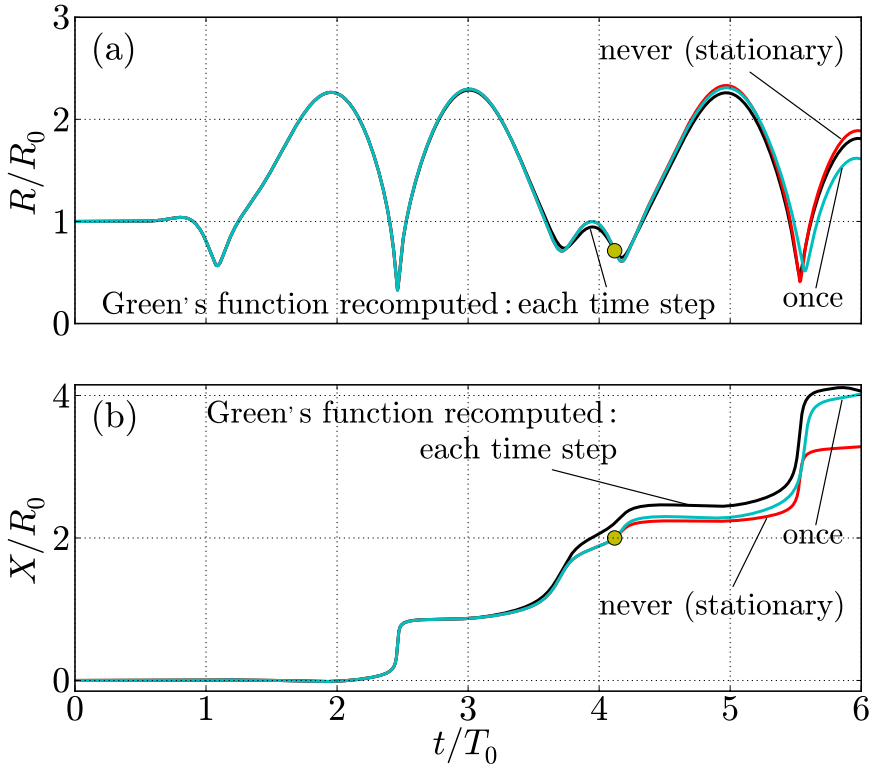

Figure 3.6: Bubble (a) pulsation and (b) translation for a bubble of radius $3\,\mu$m at an initial distance $7.5R_0$ from a rigid boundary. The bubble is excited into motion by a $3P_0$ sinusoid, where the primary Bjerknes force from the source is neglected. The reverberant pressure and its gradient are computed in three different ways: the location of the bubble used to calculate the Green's function corresponding to the reverberant fields is either updated at each time step (black); it's updated once from $7.5R_0$ to $3.5R_0$ at the yellow dot (blue); it's never updated, i.e., the reverberant fields are computed for a stationary source (red).

analytical solution for the spectrum of a rigid interface [Eq. (D.5)], bypassing the numerical integration.

Because the simulations shown in Fig. 3.6 are similar enough to each other, we resort to the discretized approach when computing the reverberant

pressure and its gradient for future simulations. This simplification gives us the latitude to work in any domain (time or frequency) we wish. Evaluating the reverberant fields in the time domain proves to be most efficient since we only perform the inverse Fourier transform once for each Green's function. The convolution then becomes a simple summation after multiplying the function g_{rev} with the volume velocity Q, and simulations are not restricted to the maximum simulation time $t_{\max}$ [Eq. (3.15)]. Additional terms of the expansion given in Eq. (3.16) can be added to increase accuracy of the calculation; however, they do not seem necessary enough given the current accuracy of the of the calculations only using one term in the expansion, shown in Fig. 3.6.

3.5 Numerical Pitfalls

While many numerical calculations require attention to detail at various points in the calculation, it is worth mentioning some of the particulars of this calculation requiring extra attention.

3.5.1 Discretization artifacts

One of the principle problems due to discretizing the bubble location during the computation of the Green's function is that the discretization size too large. Even with small discretization steps, an abrupt jump from one location to another can be observed in the computation of the reverberant fields. As seen in Fig. 3.7, when the bubble location used to compute the Green's function is changed, a sharp discontinuity is introduced in the reverberant

pressure. The subsequent discontinuities in the reverberant pressure are due

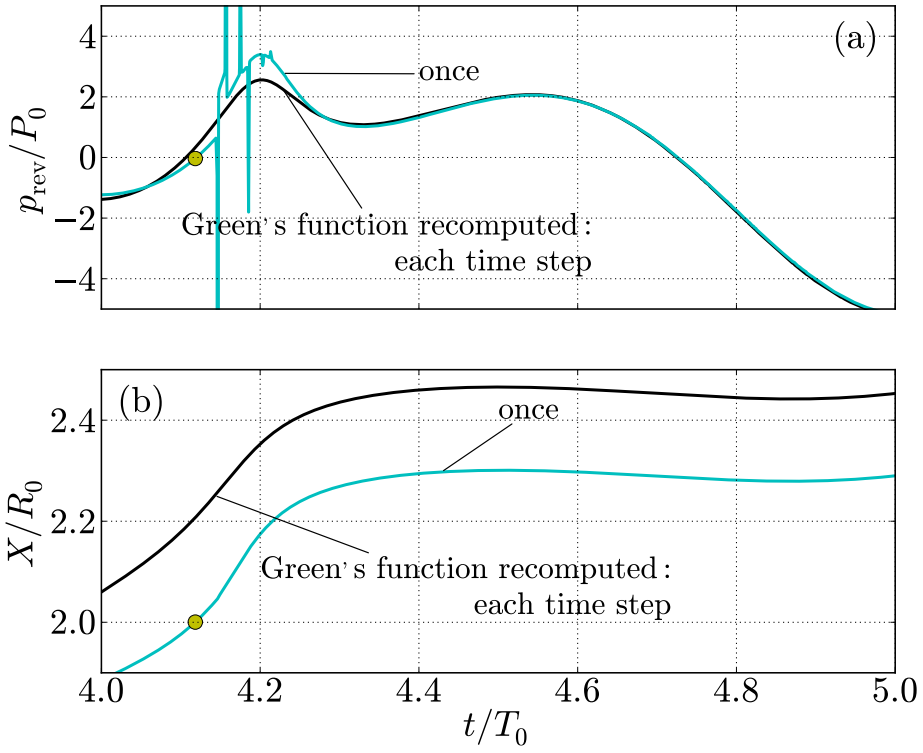

Figure 3.7: The (a) reverberant pressure and (b) bubble translation for the simulation in Fig. 3.6, but zoomed in where the Green's function is recomputed (at the yellow dot). The large discontinuities present in the reverberant pressure are due to the discretization of the source location while computing the Green's function. Both the reverberant pressure and the bubble translation are compared with the simulation which recomputed the Green's function at every time step.

to the interaction between the reverberant fields and the bubble dynamics. A discontinuity in the reverberant pressure induces a discontinuity in the bubble dynamics, which induces yet another discontinuity in the reverberant pressure, and so on until the effect decays. This can often lead to simulation instabilities,

and is avoided by reducing the discretization size.

3.5.2 Aliasing

Another problematic feature of implementing these simulations numerically is the effect of aliasing. For a stationary bubble, a maximum frequency for the spectrum of the Green's function can be chosen such that negligible aliasing occurs. However, this spectrum changes when the bubble location changes. Thus, as the bubble moves toward or away from the liquid-solid interface, the maximum frequency chosen may no longer be valid and significant aliasing may be introduced into the simulation. This aliasing can have a dramatic effect on the direction and overall amount of bubble translation, as illustrated in Fig. 3.8. The simulations shown in this figure are the same as those shown in Fig. 3.6, except that the simulations run for more time and thus allow the bubble to get very close to the rigid interface. As the bubble gets to within a few bubble radii of the boundary, the amount of aliasing affecting the computation increases. The effect of aliasing not only leads to erroneous results in the overall magnitude of the translation, but in this case alters the direction of translation as well. As the maximum frequency used to compute the reverberant field increases, the aliasing is reduced and the computation time is increased. Thus, it is advantageous to find a low enough maximum frequency to optimize the computation, while being high enough to avoid sacrificing accuracy when the bubble is close to the viscoelastic medium.

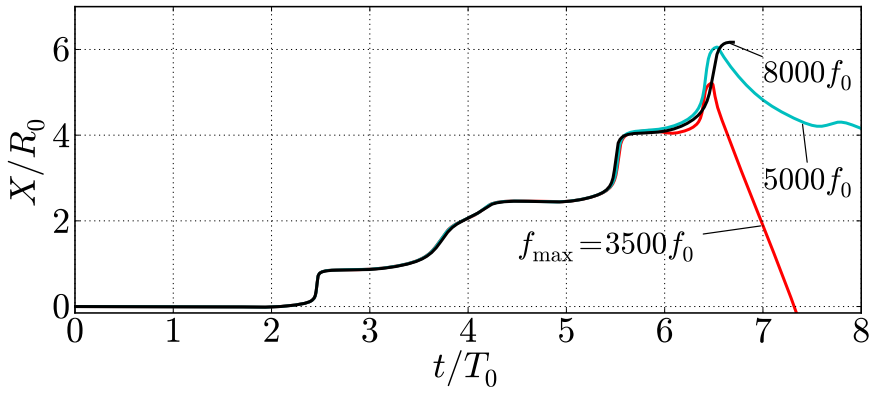

Figure 3.8: The translation of a bubble of radius 3 μm immersed in water and near a rigid wall, where the maximum frequency for computing the spectrum of the reverberant fields ranges from $3500f_0$ to $8000f_0$.

3.5.3 Reversed time sequence

Assuming that the problem employs the discretization routine outlined in Section 3.4, the inverse temporal transform is performed using a standard inverse fast-Fourier transform library. It is common that this library assumes a different sign convention for its forward and backward transforms than what is defined here. If so, this is remedied by taking the complex conjugate of the reverberant fields before numerically computing their temporal signals:

$$\begin{aligned} p_{\text{rev}}(t) &= p^*_{\text{rev}}(t) \\ &= \left(\frac{1}{2\pi} \int_{-\infty}^{\infty} \widehat{p}_{\text{rev}} e^{-i\omega t}\, d\omega \right)^* \\ &= \frac{1}{2\pi} \int_{-\infty}^{\infty} \widehat{p}^*_{\text{rev}} e^{i\omega t}\, d\omega\,, \end{aligned} \tag{3.17}$$

where the symbol * denotes complex conjugation. The reverberant pressure is equal to its conjugate because it is a real quantity, and thus the conjugate

of its frequency spectrum is used with an inverse transform of opposite sign convention.

3.5.4 Zero-frequency component

Another difficulty in computing the Green's function numerically is that the denominator of its angular spectrum can be zero when $\omega = 0$. Thus, these values are determined analytically. In the limit as $\omega \to 0$, we express $\kappa_{l,n}$ and $\kappa_{t,n}$ as series expansions and obtain the following expressions at $\omega = 0$:

$$\mathcal{F}_\omega \left\{ \frac{\partial}{\partial t} \phi_{\text{rev}} \right\} \Bigg|_{\omega=0} = -\frac{\eta_1}{4\pi\rho_1 z_0^3}\,, \tag{3.18}$$

$$\mathcal{F}_\omega \left\{ \frac{\partial}{\partial t} g_{\text{rev}} \right\} \Bigg|_{\omega=0} = -\frac{3\eta_1}{8\pi\rho_1 z_0^4}\,, \tag{3.19}$$

for simulations including viscosity in the fluid. The derivation of this result is given in Appendix E.

A quick numerical solution to this problem is to evaluate a very small nonzero frequency, instead of exactly $\omega = 0$. This method is justified since the spectra of the time derivative both ϕ_{rev} and g_{rev} converge to the constant values given in Eqs. (3.18) and (3.19), respectively, before the frequency is exactly zero.

3.5.5 Skipping the resonance frequency

As shown in Section 3.5.2, in order to avoid aliasing while calculating the reverberant fields, the maximum frequency used when numerically calculating their spectra is on the order of several thousand times the natural

frequency. Unfortunately, this large maximum frequency inevitably requires that the sample size N be quite large to ensure that the resonance frequency is sufficiently resolved. The linear step size between frequencies is calculated via

$$\Delta f = \frac{f_{\max}}{N-1}\,. \tag{3.20}$$

In order for the time-domain signal to appropriately include the effects of the bubble dynamics, it is essential to resolve the spectral information near the resonance frequency of the bubble. We are ultimately interested in bubble radii of only a few microns; thus, the maximum frequency needed to resolve the time delay due to propagation from the interface to the bubble is in the gigahertz region. For the case at hand, $N = O(2^{13})$ which gives a step size of around a 10^5 Hz, where the natural frequency of the bubble is around a megahertz.

3.6 Conclusions

This chapter covered important steps for implementing the bubble-dynamics simulations numerically. The relevant equations were converted to a nondimensional form to help with both the very large and small numbers dealt with in the problem. In addition, the numerical calculation of the reverberant fields—involving a moving source—was shown to be most accurately performed by transforming the Green's function into the frequency domain, and directly integrating the remaining dynamical quantities [Eqs. (3.12)

and (3.13)]. A practical simplification was shown for the computation of the reverberant fields, which involved discretizing the space over which the bubble translated and using these stationary bubble locations to compute the Green's function. This simplification greatly reduced the amount of computation time for each simulation without dramatically changing the results. Finally, we concluded the chapter by touching on some of the pitfalls due to numerical implementation.

Chapter 4

Model Verification

It is imperative to determine the accuracy of any given model before analyzing its predictions. For the model presented in this dissertation, we accomplish this as follows. First, we neglect translation and consider low-amplitude pulsation of a spherical bubble near a rigid wall. This allows us to compare the Green's function approach used in this dissertation with the analytical solution of the linearized Rayleigh-Plesset equation. We then consider high-amplitude pulsation, which helps to ensure that the reverberant fields are being calculated correctly—even when the bubble undergoes collapse.

Second, we verify the numerical computation of the reverberant fields produced by the presence of the liquid-solid interface. Specifically, the numerical computation of the angular-spectrum integration (i.e., the inverse Hankel transform) is checked by comparing the numerical computation of $\widehat{\phi}_{\text{rev}}(\omega) = \mathcal{H}_0^{-1}\{\Phi_{\text{rev}}\}$ in one of two different ways: first, by using the equations describing a general interface between a viscous liquid and viscoelastic medium [Eqs. (2.48) to (2.51) of Section 2.3.1]. Second, corresponding solutions where the interface conditions are simplified (derived in Appendix F) are also used as a comparison. For example, the numerical computation of $\widehat{\phi}_{\text{rev}}(\omega)$ for a

water-steel interface is compared with its computation for an interface between water and a rigid wall. Another example is the numerical computation of $\widehat{\phi}_{\text{rev}}(\omega)$ for a water-air interface, which is compared with its computation for an interface between water and a vacuum. Last, we also compute $\widehat{\phi}_{\text{rev}}(\omega)$ for a water-water interface, where theoretically no reflections should occur, to show that the numerical computation of similar interfaces is numerically tractable. We reiterate that the angular spectra for all of the idealized solutions used in these comparisons are derived in Appendix F.

Third, we reintroduce the translational bubble dynamics and check that bubble translation agrees qualitatively with experiment. This is performed for low-amplitude simulations first, such that the effects of translation are almost negligible. We then consider finite-amplitude simulations near a rigid wall to show the effects of incorporating bubble translation in the computation of the reverberant fields.

4.1 Verification for Linear Pulsation

By neglecting translation in Eq. (2.1), the dynamical model for bubble pulsation reduces to the Rayleigh-Plesset equation:

$$R\ddot{R} + \frac{3}{2}\dot{R}^2 = \frac{P_{\text{liq}} - P_0 - p_e - p_{\text{rev}}}{\rho_1}\,. \tag{4.1}$$

Verification of the numerical implementation of Eq. (4.1) is performed by simulating free bubble oscillation for low-amplitude pulsation and comparing this with the analytical solution of the linearized form of Eq. (4.1). This compari-

son is first considered for a bubble near a rigid wall, immersed in an inviscid fluid.

4.1.1 Bubble near a rigid wall in an inviscid fluid

To linearize Eq. (4.1), we first define the radial pulsation as $R = R_0 + \xi$. Then by assuming $\xi \ll R_0$, we then obtain the following linearized form:

$$\ddot{\xi} + \omega_0^2 \xi = -\frac{p_{\text{rev}}}{\rho_1 R_0}\,, \tag{4.2}$$

where the natural oscillation frequency ω_0 is

$$\omega_0^2 = \frac{1}{\rho_1 R_0^2}\left[3\gamma\,(P_0 - P_v) + (3\gamma - 1)\,\frac{2\sigma}{R_0}\right]\,. \tag{4.3}$$

The last term in Eq. (4.2) is computed by convolving the portion of the Green's function which corresponds to the reverberant pressure, ϕ_{rev}, with the volume velocity of the bubble Q. This convolution is proportional to the pressure in the fluid coming back onto the bubble due to the nearby interface, and is repeated here for convenience [Eq. (2.63)]:

$$p_{\text{rev}} = -\rho_1 \frac{\partial}{\partial t}\int_{-\infty}^{\infty} \phi_{\text{rev}}(t-\tau) Q(\tau)\, d\tau \tag{4.4}$$

$$= -\rho_1 \frac{\partial}{\partial t}\int_{-\infty}^{\infty} \phi_{\text{rev}}(\tau) Q(t-\tau)\, d\tau\,. \tag{4.5}$$

Near a rigid wall with a slip condition on its surface, Appendix D shows the derivation of the frequency spectrum of ϕ_{rev}:

$$\widehat{\phi}_{\text{rev}} = -\frac{e^{i\omega D/c_1}}{4\pi D}\,, \tag{4.6}$$

where c_1 is the compressional sound speed in the fluid, and $D = z_0 - z$. We recall from Fig. 2.1 that the bubble is located at $z = -z_0$, and since we are interested in the reverberant pressure field incident on the bubble, we take $D = 2z_0$. Using the transform relation for a complex exponential,[†] the inverse Fourier transform of Eq. (4.6) yields a temporal Delta function,

$$\phi_{\text{rev}} = -\frac{\delta(t - D/c_1)}{4\pi D}\,. \tag{4.7}$$

The linearized volume velocity is $Q = 4\pi R_0^2 \dot{\xi}$, and substitution of this and Eq. (4.7) into Eq. (4.5) produces

$$\begin{aligned} p_{\text{rev}} &= \frac{\rho_1 R_0^2}{D} \int_{-\infty}^{\infty} \delta(\tau - D/c_1)\, \ddot{\xi}(t - \tau)\, d\tau \\ &= \frac{\rho_1 R_0^2}{D} \ddot{\xi}(t - D/c_1)\,, \end{aligned} \tag{4.8}$$

which is then substituted into Eq. (4.2) to give

$$\ddot{\xi} + \omega_0^2 \xi = -\frac{R_0}{D} \ddot{\xi}(t - D/c_1)\,. \tag{4.9}$$

Equation (4.9) is similar to Eq. (3.27) of Thomas[21] for a two-bubble case, assuming the bubbles oscillate in phase with one another; however, the comparison is not identical since we neglect radiation damping.[‡] As the liquid becomes incompressible ($c_1 \to \infty$), we can combine terms involving $\ddot{\xi}$ in Eq. (4.9) to produce

$$\ddot{\xi} + \frac{\omega_0^2}{1 + R_0/D} \xi = 0\,. \tag{4.10}$$

[†]Equation (1.36) of Ref. 64.

[‡]The terms due to radiation damping are neglected in this dissertation since they require derivatives of the Green's function which can cause significant numerical instability.

Equation (4.10) is similar to Eq. (3.28) of Thomas[21] when the two-bubble case is again considered and radiation damping is again neglected. Equation (4.10) shows that the presence of the rigid wall lowers the natural oscillation frequency of the bubble by a factor of $1/\sqrt{1+R_0/D}$. While neglecting the time delay in Eq. (4.9) helps us to quantify the change in the oscillation frequency of the bubble, this time delay is inherent in the numerical computation of the Green's function. In addition, including the time delay (due to the fluid compressibility) in the reverberant pressure provides notable differences in the decay of a freely oscillating bubble.[†] Because the time delay is built into the Green's function model presented here, comparison with Eq. (4.9), instead of Eq. (4.10), is necessary.

We obtain an analytical solution to Eq. (4.9) by first assuming a general form for the linear pulsation of the bubble:

$$\xi = \xi_0 e^{st}\,, \tag{4.11}$$

where ξ_0 is the initial state of the bubble at time $t = 0$, and s is an unknown complex variable. We determine s upon substitution of Eq. (4.11) into Eq. (4.9), yielding

$$\left[\left(1+\frac{R_0}{D}e^{-sD/c_1}\right)s^2+\omega_0^2\right]\xi = 0\,, \tag{4.12}$$

[†]Compare models C3-L (compressible liquid) and C4-L (incompressible liquid) in Fig. (3.5) of Thomas,[21] or Fig. 2(b) of Feuillade.[20] Both show an increase in damping of radial pulsation after including propagation delay.

where a nontrivial solution is obtained by letting

$$\left[\left(1+\frac{R_0}{D}e^{-sD/c_1}\right)s^2+\omega_0^2\right]=0\,. \tag{4.13}$$

Equation (4.13) is a transcendental equation; thus, a solution for s at a particular distance D is obtained numerically.

Figure 4.1 displays the temporal pulsation of a bubble of radius $3\,\mu$m, where the bubble is located a distance of $2.5R_0$ from a rigid surface. The bubble oscillates freely after beginning with an initial radius of $0.9R_0$. The blue dashed curve illustrates the analytical solution given in Eq. (4.11) after solving Eq. (4.13) for s with $D = 5R_0$. The red curve displays the result obtained through numerical integration of Eq. (4.9). Although the fluid is inviscid, accounting for propagation delay introduces damping in the bubble pulsation.

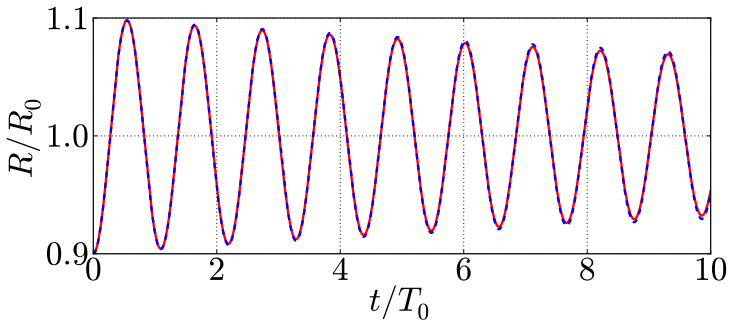

Figure 4.1: Pulsation of a bubble of radius $3\,\mu$m in free oscillation, at distance $2.5R_0$ from a rigid interface, with an initial radius of $0.9R_0$. The blue dashed curve shows Eq. (4.11) after numerically solving for s in Eq. (4.13). The red curve displays the solution obtained after numerical integration of Eq. (4.9).

4.1.2 Bubble near a rigid wall in a viscous fluid

Because fluid viscosity is essential for the numerical computation of the Green's function, it is imperative that we include viscosity to calculate the reverberant pressure using the Green's function. Thus, we consider the same type of analysis we just performed, while including viscosity in the fluid. In order to account for the fluid viscosity, both the linearized Rayleigh-Plesset equation and the reverberant pressure field are modified. The linearized Rayleigh-Plesset equation becomes

$$\ddot{\xi} + \frac{4\eta_1}{\rho_1 R_0^2}\dot{\xi} + \omega_0^2 \xi = -\frac{p_{\text{rev}}}{\rho_1 R_0}\,, \tag{4.14}$$

where the second term on the left-hand side describes the decay of bubble pulsation due to the shear viscosity η_1 in the liquid. The reverberant pressure field is related to ϕ_{rev} [Eq. (4.6)], which must now account for viscous losses. Thus, a more general expression for the frequency spectrum of ϕ_{rev} is

$$\widehat{\phi}_{\text{rev}} = -\frac{e^{ik_{l,1}D}}{4\pi D}\,, \tag{4.15}$$

where

$$k_{l,1} = \omega\sqrt{\frac{\rho_1}{\lambda_1 - i\omega(\zeta_1 + 2\eta_1)}}\,. \tag{4.16}$$

Assuming the fluid has no shear modulus, $\lambda_1 = \rho_1 c_1^2$ and Eq. (4.16) is rearranged and expanded as

$$\begin{aligned} k_{l,1} &= \frac{\omega}{c_1}\left[1 - i\omega\left(\frac{\zeta_1 + 2\eta_1}{\rho_1 c_1^2}\right)\right]^{-1/2} \\ &\simeq \frac{\omega}{c_1}\left(1 + i\omega\delta\right)\,, \end{aligned} \tag{4.17}$$

where

$$\delta = \frac{\zeta_1 + 2\eta_1}{2\rho_1 c_1^2}\,. \tag{4.18}$$

By only considering the first term on the right-hand side of Eq. (4.17), the frequency spectrum of ϕ_{rev}, defined in Eq. (4.15), reduces to that given in Eq. (4.6).

Substitution of Eq. (4.17) into Eq. (4.15) yields the following analytically tractable form for ϕ_{rev}:

$$\phi_{\text{rev}} = -\frac{1}{2\pi}\int_{-\infty}^{\infty} \frac{e^{-i\omega(t-D/c_1)}}{4\pi D} e^{-\omega^2 \delta D/c_1}\, d\omega \tag{4.19}$$

$$= -\frac{1}{4\pi D}\sqrt{\frac{c_1}{4\pi\delta D}}\, e^{-\frac{(t-D/c_1)^2}{4\delta D/c_1}}\,, \tag{4.20}$$

where Eq. (4.20) reduces to Eq. (4.7) for $\omega\delta \ll 1$ in Eq. (4.19). For the case of a microbubble in water, $\omega\delta$ is of order $O(10^{-6})$. Thus, the additional term in the expansion of $k_{l,1}$ is negligible and $\widehat{\phi}_{\text{rev}}$ may again be defined by Eq. (4.7). Hence, substitution of Eq. (4.8) into Eq. (4.14) gives

$$\ddot{\xi} + \frac{4\eta_1}{\rho_1 R_0^2}\dot{\xi} + \omega_0^2 \xi = -\frac{R_0}{D}\ddot{\xi}(t - D/c_1)\,, \tag{4.21}$$

which is a linearized Rayleigh-Plesset equation accounting for viscosity and compressibility in the liquid, while still ignoring damping due to radiation. Hence, substitution of Eq. (4.20) and the linearized volume velocity into Eq. (4.5) produces

$$p_{\text{rev}} = \frac{\rho_1 R_0^2}{D}\sqrt{\frac{c_1}{4\pi\delta D}}\int_{-\infty}^{\infty} e^{-\frac{(\tau-D/c_1)^2}{4\delta D/c_1}}\ddot{\xi}(t-\tau)\, d\tau\,, \tag{4.22}$$

and substitution of Eq. (4.22) for the last term in Eq. (4.14) yields

$$\ddot{\xi} + \frac{4\eta_1}{\rho_1 R_0^2}\dot{\xi} + \omega_0^2 \xi = -\frac{R_0}{D}\sqrt{\frac{c_1}{4\pi\delta D}} \int_{-\infty}^{\infty} e^{-c_1 \frac{(\tau - D/c_1)^2}{4\delta D}} \ddot{\xi}(t-\tau)\, d\tau\,. \tag{4.23}$$

Figure 4.2 shows the temporal pulsation of a bubble of equilibrium radius $3\,\mu$m in free oscillation, where the bubble begins with an initial radius of $0.9R_0$, at distance $7.5R_0$ from the rigid wall ($D = 15R_0$). The simulation is performed by calculating the reverberant pressure in two different ways. The red curve shows the calculation of the reverberant pressure as given in Eq. (4.21). Thus, we simply use the bubble acceleration at time $t - D/c_1$ in the bubble dynamics simulation. In contrast, the blue dashed curve shows the calculation of the reverberant pressure as given on the right-hand side of Eq. (4.23), where the reverberant pressure is explicitly calculated via convolution with ϕ_{rev}, as presented in Chapter 3. We note that the methods are identical to within graphical resolution, and that the oscillation frequency is correctly lowered by a factor of $1/\sqrt{1+1/15} \approx 0.968$. A slight discrepancy is in the pulsation amplitude and is due to the nonlinear Rayleigh-Plesset equation [Eq. (4.1)] used to calculate the blue dashed curve.

We also check the numerical computation of the bubble pulsation and the reverberant pressure for simulations involving moderately high-amplitude pulsation. In order to do so, however, we can no longer compare with the linearized Rayleigh-Plesset equation [Eq. (4.14)]. Thus, we model the bubble pulsation using Eq. (4.1) and calculate the reverberant pressure in two different ways. For the first method, we compute the reverberant pressure as shown

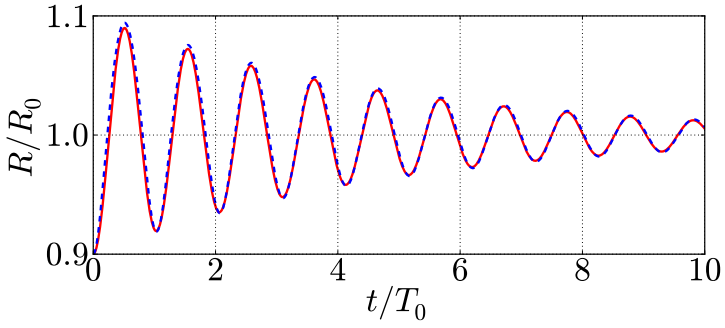

Figure 4.2: Pulsation of a bubble of equilibrium radius $3\,\mu$m at distance $7.5R_0$ from a rigid interface, where the initial radius of the bubble is $0.9R_0$. The pulsation is calculated either via numerical integration of Eq. (4.23) (red), or Eq. (4.21) (blue, dashed).

on the right-hand side of Eq. (4.23), except that the volume velocity is not linearized; this method accounts for fluid viscosity in the Green's function and computes the reverberant pressure explicitly as a convolution. For the second method, ϕ_{rev} is approximated as a delta function as in Eq. (4.7), giving

$$p_{\text{rev}} = \rho_1 \frac{\dot{Q}(t - D/c_1)}{4\pi D}\,. \tag{4.24}$$

Figure 4.3(a) compares the pulsation of a bubble of radius $3\,\mu$m, where the bubble is located a distance of $7.5R_0$ from a rigid interface (with a slip condition) and the reverberant pressure is calculated using these two different methods. The method which computes the reverberant pressure via Eq. (4.24) is illustrated in red, while the method which includes fluid viscosity in ϕ_{rev} is shown in blue. For these simulations, the initial bubble radius is $3R_0$; hence, the subsequent dynamics are nonlinear and include bubble collapse. Figure 4.3(b) shows the reverberant pressure calculated at the bubble center via both methods. Regions of high pressure appear to occur during bubble collapse, though

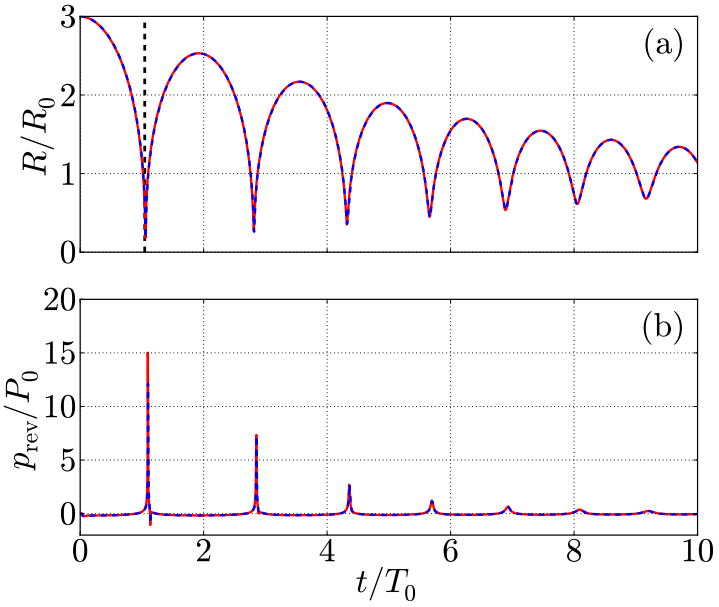

Figure 4.3: Comparison of the (a) radial pulsation and (b) reverberant pressure using (red) Eq. (4.24) in the fully nonlinear Rayleigh-Plesset equation [Eq. (4.1)] and the (blue, dashed) Green's function method for a $3\,\mu$m radius bubble in free oscillation, at a distance of $7.5R_0$ from a rigid interface, with an initial radius of $3R_0$. In (a), the time for Rayleigh collapse [Eq. (4.25)] is indicated by the (black, dashed) vertical line near $t/T_0 = 1$.

they are slightly delayed in time. For larger distances, the time delay is more apparent. Agreement of these two methods ensures that the numerical computation of the angular-spectrum integration works properly.

To ensure that the first collapse occurs at approximately the correct time, we compare the time to the first collapse with the Rayleigh collapse time [Eq. (2.27) of Leighton[16]]:

$$t_{\mathrm{collapse}} = 0.915 R_{\mathrm{init}} \sqrt{\frac{\rho_1}{P_0}}\,, \tag{4.25}$$

where R_{init} is the initial radius of the bubble. While the Rayleigh collapse

time is derived by assuming an unbounded incompressible liquid, and a vacuum inside the bubble cavity, it is still used as an approximate check of the nonlinear radial dynamics. For the case presented in Fig. 4.3(a), the associated Rayleigh collapse time is indicated by the vertical, black, dashed line near $t/T_0 = 1$.

While Figs. 4.2 and 4.3 verify accurate simulations for the radial dynamics of the bubble, we reiterate that, up to this point, we have only considered an interface between water and a rigid wall for the simulations computed via the Green's function method. In other words, we have greatly reduced the complexity of the problem by skipping the angular-spectrum integration. Hence, we must incorporate the angular-spectrum integration in order to consider a general interface between a viscous fluid and a viscoelastic medium.

4.2 Verification of the Reverberant Spectra

To determine the accuracy of the numerical computation of the Green's function for an interface between an arbitrary viscous fluid and a viscoelastic medium, we compare the angular-spectrum form with various cases for which analytical solutions exist. Because this computation does not involve translation, we compute $\widehat{\phi}_{\text{rev}}(\omega)$ at $z = -z_0$ (i.e., the bubble location) via an inverse spatial transform of the angular spectrum $\Phi_{\text{rev}}(\kappa)$ [Eq. (2.64)]:

$$\widehat{\phi}_{\text{rev}}(\omega) = \frac{1}{2\pi} \int_0^\infty B e^{-\kappa_{l,1} z_0} \kappa \, d\kappa \, . \tag{4.26}$$

Repeated here for convenience is the coefficient B for a general fluid-solid interface, which is derived in Appendix B:

$$B = -\frac{(C_1 + C_2) - (C_3 - C_4)}{(C_1 + C_2) + (C_3 - C_4)} A \,, \tag{4.27}$$

where

$$\begin{aligned}
C_1 &= [(\beta_1 - \beta_2)\kappa_{l,2}\kappa_{t,1} - (\alpha_1 - \alpha_2)\kappa]\,(\alpha_1 - \alpha_2)\kappa \,, \\
C_2 &= [(\beta_1\kappa - \alpha_2)\kappa_{t,1} + (\beta_2\kappa - \alpha_1)\kappa_{t,2}]\,(\beta_2\kappa - \alpha_1)\kappa_{l,2} \,, \\
C_3 &= [(\beta_1\kappa - \alpha_2)\kappa_{t,1} + (\beta_2\kappa - \alpha_1)\kappa_{t,2}]\,(\beta_1\kappa - \alpha_2)\kappa_{l,1} \,, \\
C_4 &= [(\beta_1 - \beta_2)\kappa_{l,2}\kappa_{t,1} - (\alpha_1 - \alpha_2)\kappa]\,(\beta_1 - \beta_2)\kappa_{l,1}\kappa_{t,2} \,,
\end{aligned}$$

and [Eq. (2.57)]

$$A = -\frac{1}{2\kappa_{l,1}} e^{-\kappa_{l,1} z_0} \,. \tag{4.28}$$

The computation of $\widehat{\phi}_{\text{rev}}(\omega)$ is performed for three different cases. First, it is computed for a water-steel interface. The computed solution for this interface should be similar to that obtained for an interface between water and a rigid wall, given by Eq. (4.6). Next we compute $\widehat{\phi}_{\text{rev}}(\omega)$ for a water-air interface and compare it with its analytical counterpart—an interface between water and a vacuum, which yields the negative of Eq. (4.6):

$$\widehat{\phi}_{\text{rev}} = \frac{e^{i\omega D/c_1}}{4\pi D} \,. \tag{4.29}$$

Last, we compute $\widehat{\phi}_{\text{rev}}(\omega)$ for a water-water interface, which theoretically is zero.

Because Eq. (4.6) is derived assuming a slip condition at the interface, viscous effects (i.e., the boundary layer) are not present in its spectrum. In order to validate the entire frequency spectrum of $\widehat{\phi}_{\text{rev}}(\omega)$, we reduce Eq. (4.27) for the three idealized cases listed in the previous paragraph, and compare their corresponding results with those obtained with the unreduced form in Eq. (4.27). Thus, for an interface between water and a rigid wall we assume the second medium is completely rigid, yielding [Eq. (F.19)]

$$B = -\frac{\kappa^2 + \kappa_{t,1}\kappa_{l,1}}{\kappa^2 - \kappa_{t,1}\kappa_{l,1}} A\,, \tag{4.30}$$

where a no-slip condition has been enforced. Second, for an interface between water and a vacuum we assume the pressure in the second medium is zero, producing [Eq. (F.23)]

$$B = -\frac{\alpha_1^2 + \beta_1^2\kappa_{t,1}\kappa_{l,1}}{\alpha_1^2 - \beta_1^2\kappa_{t,1}\kappa_{l,1}} A\,. \tag{4.31}$$

Last, assuming both media are fluids where their properties are identical to one another gives [Eq. (F.12)]

$$\begin{aligned} B &= \frac{\rho_2\kappa_{l,1} - \rho_1\kappa_{l,2}}{\rho_2\kappa_{l,1} + \rho_1\kappa_{l,2}} A\,, \\ &= 0\,, \quad \text{for} \quad \rho_1 = \rho_2 \quad \text{and} \quad \kappa_{l,1} = \kappa_{l,2}\,. \end{aligned} \tag{4.32}$$

While these results are merely presented here, their respective derivations are detailed in Appendix F.

Figures 4.4 and 4.5 show the comparisons between the numerical computation of $\widehat{\phi}_{\text{rev}}(\omega)$ at distance $22.5\,\mu$m ($7.5R_0$ for $R_0 = 3\,\mu$m) from a water-steel and water-air interface, respectively. The specific material properties

	Water	Steel	Air
Density (kg/m^3)	998	7700	1.21
Speed of sound (m/s)	1484	5741	343
Shear modulus (Pa)	0	75.74×10^9	2.85×10^{-2}
Shear viscosity (Pa·s)	10^{-3}	10^{-4}	10^{-6}
Bulk viscosity (Pa·s)	3.09×10^{-3}	0	0

Table 4.1: Properties assigned to the materials used to calculate the reverberant spectra in Figs. 4.4 and 4.5. The fluid is assigned values for water, and the viscoelastic medium is given properties of either steel or air.

used for water, steel, and air in these calculations are tabulated in Table 4.1, where the values for water have been repeated for convenience. Function $\widehat{\phi}_{\text{rev}}(\omega)$ is normalized by Eq. (4.6), where the spectrum in Eq. (4.6) is denoted as $\widehat{\phi}_{\text{im}}$ since it is the spectrum of an image source of a point source near a rigid boundary. The blue dashed curves show the ratio of $\widehat{\phi}_{\text{rev}}$ to $\widehat{\phi}_{\text{im}}$ after numerical integration of Eq. (4.26), using the most general expression for the coefficient B [Eq. (4.27)].[†]

Although these calculation of $\widehat{\phi}_{\text{rev}}(\omega)$ requires no bubble parameters, we note that the portion of the axes shaded in pink corresponds to the natural oscillation frequency of a bubble of radius $3\,\mu$m. We note that $\widehat{\phi}_{\text{rev}}$ diverges from $\widehat{\phi}_{\text{im}}$ at very low frequencies and very high frequencies relative to the natural frequency of the bubble, both of which are due to the absence of liquid viscosity in $\widehat{\phi}_{\text{im}}$. The red curves in Figs. 4.4 and 4.5 show the corresponding frequency spectra of $\widehat{\phi}_{\text{rev}}(\omega)$, obtained by numerical integration of Eq. (4.26),

[†]The coefficient B is obtained numerically after solving the linear system of equations given in Eq. (2.59).

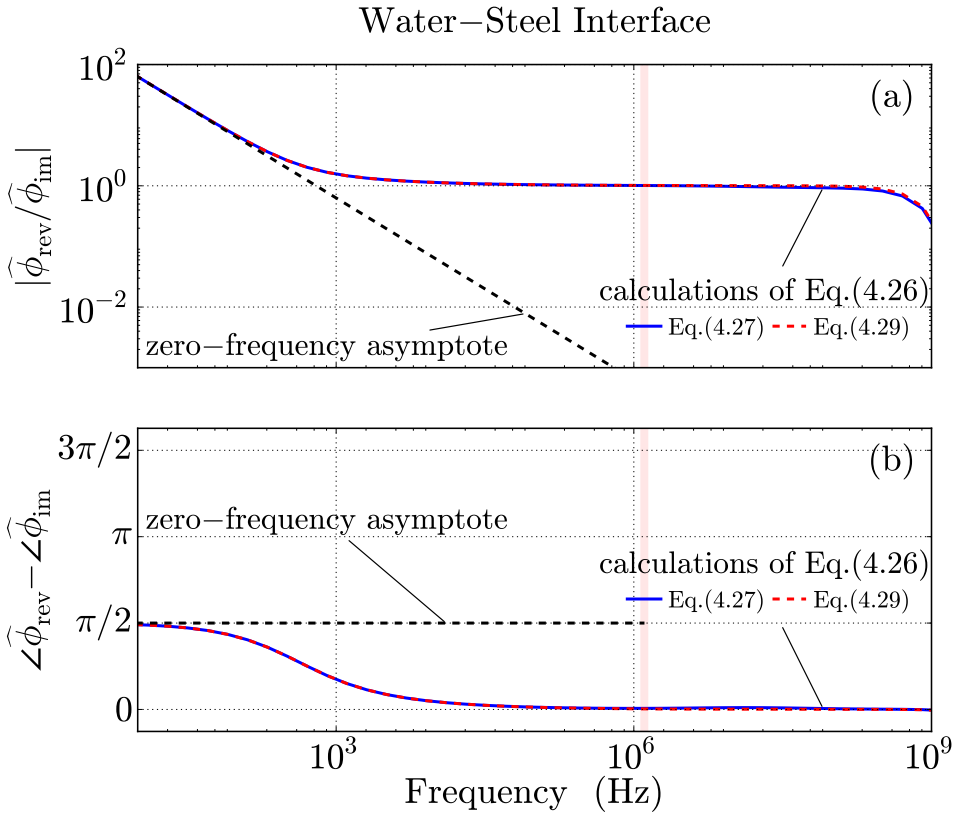

Figure 4.4: Comparison of the numerical computation of $\widehat{\phi}_{\rm rev}$ at a distance of $22.5\,\mu$m ($7.5R_0$ for $R_0 = 3\,\mu$m) from a water-steel interface, and normalized by Eq. (4.6). The blue line is calculated via numerical integration of Eq. (4.26), where the coefficient B is calculated using Eq. (4.27). The red dashed line is also computed through numerical integration of Eq. (4.26), but the coefficient B is calculated using Eq. (4.30). The magnitude of $\widehat{\phi}_{\rm rev}$ at $\omega = 0$ is represented by the black dashed line to show correct convergence of the spectra at low frequencies.

while using the idealizations of the coefficient B given in Eqs. (4.30) and (4.31), respectively. Last, the black curves show the corresponding value of the magnitude of $\widehat{\phi}_{\rm rev}$ when $\omega = 0$, obtained analytically in Appendix E. This constant is also normalized by the image source given in Eq. (4.6). The frequency spec-

tra computed using the unreduced form of the coefficient B [Eq. (4.27)] are the same as those computed with the reduced forms [Eqs. (4.30) and (4.31)] to within graphical resolution. This verification provides assurance that the linear system of equations used to compute the spectra [Eq. (2.59)] is correct. We note that while the magnitudes of the spectra for both a water-air and a water-steel interface are similar, the phase shown in Figs. 4.4(b) and 4.5(b) of the two simulations are in antiphase with each other.

Figure 4.6 shows $\widehat{\phi}_{\text{rev}}(\omega)$, normalized by $\widehat{\phi}_{\text{im}}(\omega)$ for a water-water interface obtained via numerical integration of Eq. (4.26), where the general form of the coefficient B [Eq. (4.27)] is used. The analytical solution is not shown in Fig. 4.6 since it is zero. We note that the values computed numerically for this interface are several orders of magnitude lower than those shown in Figs. 4.4 and 4.5, ensuring that the reverberant field is negligible.

Figures 4.4–4.6 show that $\widehat{\phi}_{\text{rev}}(\omega)$ is computed with sufficient accuracy for all of the different cases considered. These checks assure us that the Green's function method can accurately compute the reverberant field for arbitrary parameters for the viscoelastic half-space, and can be used to correctly represent the reverberant fields during a time-domain simulation of the bubble dynamics.

4.3 Verification for Translation

The final test we perform is to check that translation is correctly incorporated into the bubble dynamics simulations. Figure 4.7 shows the (a)

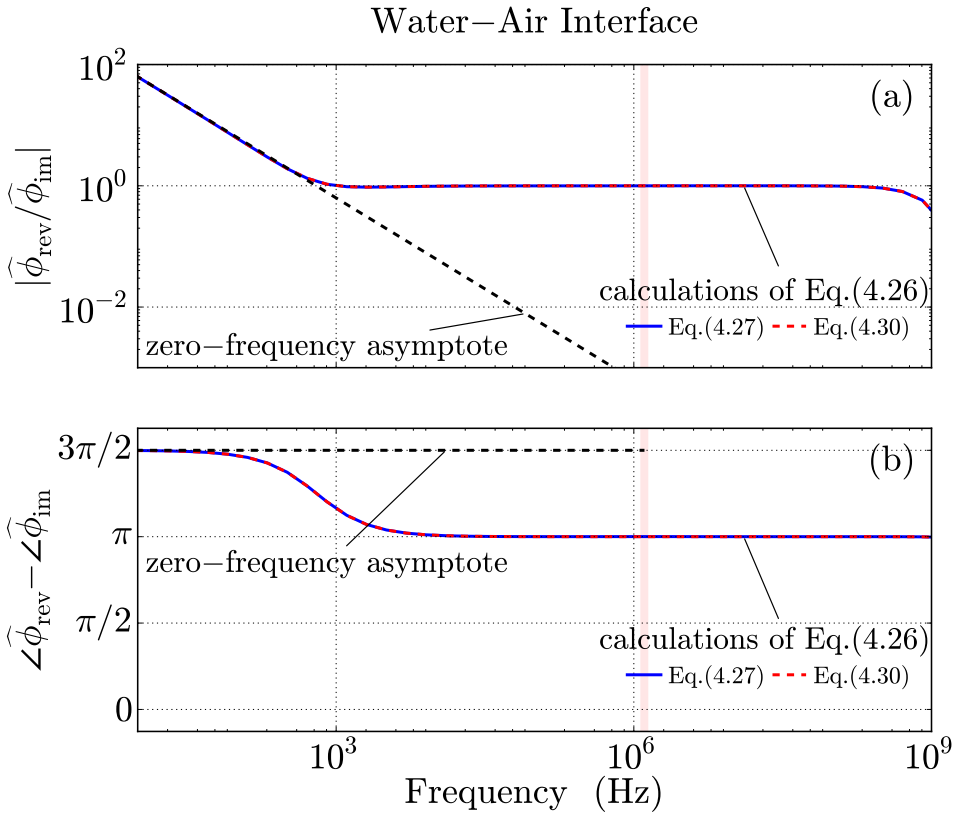

Figure 4.5: Comparison of the numerical computation of $\widehat{\phi}_{\rm rev}$ at a distance of 22.5 μm ($7.5R_0$ for $R_0 = 3\,\mu$m) from a water-air interface, and normalized by Eq. (4.6). The blue dashed line is calculated via numerical integration of Eq. (4.26), where the coefficient B is calculated using Eq. (4.27). The red line is also computed through numerical integration of Eq. (4.26), but the coefficient B is calculated using Eq. (4.31). The magnitude of $\widehat{\phi}_{\rm rev}$ at $\omega = 0$ is represented by the black dashed line to show correct convergence of the spectra at low frequencies.

pulsation and (b) translation of a spherical bubble of radius 3 μm, released from rest with initial radius $0.8R_0$, immersed in water and at distance $7.5R_0$ from a water-steel (blue, dashed) or water-air (red) interface. The material properties assigned to water, steel, and air are the same as those used to com-

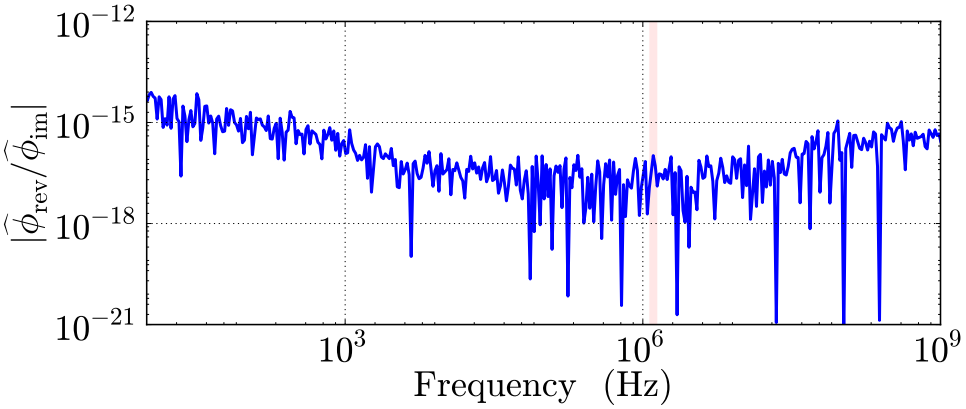

Figure 4.6: Numerical integration of Eq. (4.26), where the coefficient B is defined by Eq. (4.27), at distance 22.5 μm ($7.5R_0$ for $R_0 = 3\,\mu$m) from a water-water interface, and normalized by the corresponding function for an image source [Eq. (4.6)].

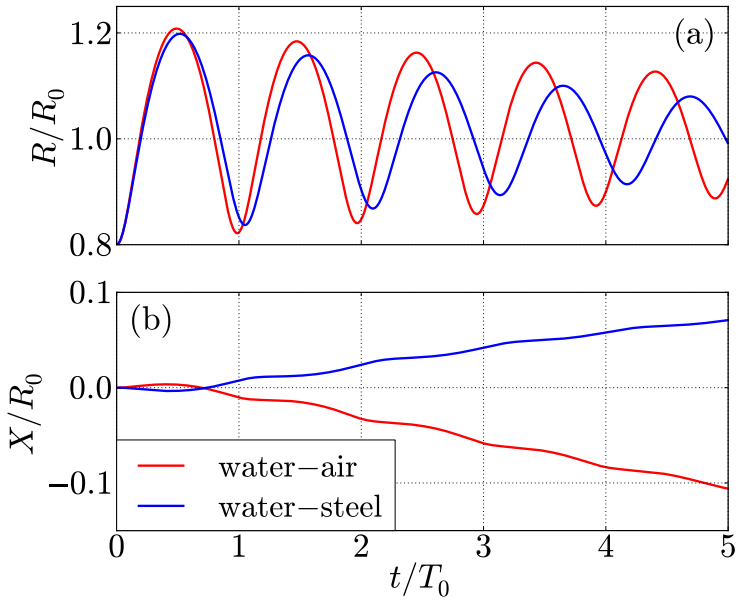

Figure 4.7: Time-domain simulations for the (a) pulsation and (b) translation of a 3 μm radius bubble in free oscillation, at a distance of $7.5R_0$ from a water-steel (black) or water-air (red) interface.

pute the spectra in Figs. 4.4 and 4.5, and are listed in Table 4.1. As shown in previous work, bubble translation tends toward a rigid surface and away from a pressure-release surface.[1,3] Since most of the work on bubble translation involves two or more bubbles in free space (rather than a single bubble near an interface), we compare with the two-bubble cases by considering the second bubble to be an image source due to the nearby rigid or pressure-release boundary. It is worth noting that the direction of bubble translation is due to the phase of the field produced by the second bubble—relative to the pulsation of the real bubble; if the pressure field produced by the second bubble (the image) is in phase with the pulsation of the real bubble then these two bubbles attract. Whereas if the pressure field produced by the second bubble (the image) is in antiphase with the pulsation of the real bubble (i.e., the image source due to a pressure-release surface), then the two bubbles repel.[44,46,71]

Because the bubble pulsation shown in Fig. 4.7 is linear and translation is small, we expect the resonance frequency to shift as was shown for the stationary bubble in Section 4.1. Thus, in addition to the bubble translation being in the right direction, the number of cycles after 5 Minneart periods for the bubble near the steel interface is approximately correct for a stationary bubble (4.8 cycles). For the bubble near the air half-space, we expect the resonance frequency to increase by a factor of $1/\sqrt{1 - R_0/D}$; as seen in Fig. 4.7, the number cycles for 5 Minneart periods is about 5.2.

Last, Fig. 4.8 shows the (a) pulsation, (b) translation, and (c) reverberant pressure for simulations of a spherical bubble of radius $3\,\mu$m in free

oscillation, where the bubble is initially located at distance $7.5R_0$ from a rigid wall with a slip condition at its surface. In this figure, the only difference in computation is with regard to the reverberant pressure and its gradient. The red curve shows the bubble dynamics and subsequent reverberant pressure for the case in which a stationary source is assumed during computation of the Green's function. The blue curve, however, shows the dynamics and reverberant fields after recomputing the Green's function at every time step. Figure 4.8(c) shows that including bubble translation in the computation of reverberant pressure causes significant changes in both amplitude and time of arrival. Qualitatively, a change in pressure amplitude is expected when bubble translation is incorporated in the computation of the reverberant pressure since the resulting pressure is due to both the velocity of the bubble wall and the bubble center. Likewise, by including bubble translation in the calculation of the pressure field the amount of time that a pressure wave created by the bubble takes to travel from the bubble to the interface, reflect off the interface and travel back onto the bubble is altered . For example, consider the large pressure wave produced by the bubble during its collapse at $t/T_0 = 2.46$ in Fig. 4.8(a). In a compressible liquid, the amount of time that it takes for this pressure wave to travel to the interface and back to the bubble is $D/c_1 = 15R_0/c_1 \approx 0.039T_0$. Thus, for a stationary bubble we expect the pressure wave produced during bubble collapse to arrive back at the bubble at approximately $t/T_0 = 2.5$. We note that the reverberant pressure field calculated assuming a stationary source (the red curve) shows a large pressure

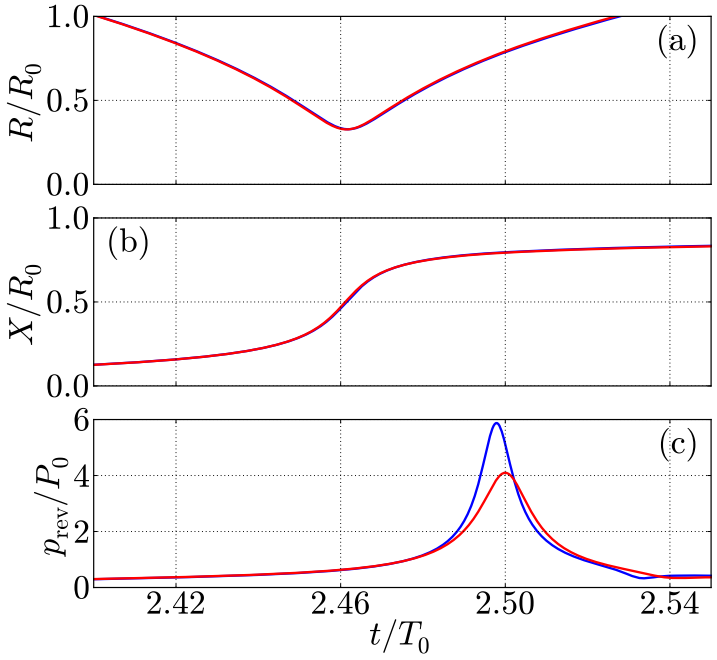

Figure 4.8: Time-domain simulations for the (a) pulsation and (b) translation of a bubble of radius $3\,\mu$m, where the bubble is initially located at distance $7.5R_0$ from a rigid interface. The (c) reverberant pressure is calculated in two ways, either accounting for a bubble translation during computation of $\widehat{\phi}_{\mathrm{rev}}$ (blue) or assuming a stationary source during computation of $\widehat{\phi}_{\mathrm{rev}}$ (red).

compression arriving back at the bubble at this expected time [$t/T_0 = 2.5$ in Fig. 4.8(c)]. The same pressure wave calculated assuming a moving source, however, arrives back at the bubble center sooner since, in this example, the bubble translates toward the interface. In the example shown in Fig. 4.8, including bubble translation while computing the reverberant fields does not seem to have a significant effect on the subsequent bubble dynamics, especially during regions of low-amplitude pulsation and translation. However, the significance of including bubble translation in the computation of the reverberant

fields is best determined on a case-by-case basis since it depends significantly on the standoff distance, the strength of the external field, and the properties of the viscoelastic solid.

4.4 Conclusions

This chapter verified the numerical model developed to simulate pulsation and translation of spherical bubbles near an arbitrary viscoelastic halfspace. First, the numerical integration scheme used to model the bubble dynamics was checked for a stationary bubble. The dynamics for linear pulsation were checked against its analytical counterpart, developed in Section 4.1. These simulations showed that the resonance frequency was lowered by a factor of $1/\sqrt{1+R_0/D}$, due to the fields produced by the nearby rigid wall. The dynamics for nonlinear pulsation were also checked by comparing the time required for bubble collapse with the Rayleigh collapse time. These two times were shown to be in very close agreement. These checks validate that numerical computation of the nonlinear equation representing bubble pulsation correctly reduces to the linear model and correctly incorporates the reverberant pressure.

Second, the numerical computation of $\widehat{\phi}_{\text{rev}}(\omega)$, which is used to compute the reverberant pressure, was verified by comparing the results with various idealized solutions. In order to do so, the following three cases were considered: (1) a water-steel interface, (2) a water-air interface, and (3) a water-water interface. The corresponding idealized solutions were interfaces between a fluid

and rigid surface, a fluid and a pressure-release surface, and two identical fluids (theoretically providing no reflection), respectively. Agreement between the frequency spectra of ϕ_{rev} produced for all three situations were identical to within graphical resolution. These solutions were also compared to the analytical solution for the frequency spectrum of $\frac{\partial}{\partial t}\phi_{\text{rev}}$ at very low frequencies (derived in Appendix E) and correctly converged to the zero-frequency solution.

Last, bubble translation was introduced into the model to verify that both pulsation and translation are correctly affected by the reverberant fields. For low-amplitude free bubble oscillation, the natural frequency was again shifted due to the presence of the viscoelastic medium. The translational dynamics were checked in two different ways. First, the direction of bubble translation was confirmed to move toward a water-steel (rigid) interface and away from a water-air (pressure release) interface. Second, the reverberant pressure, which was calculated accounting for bubble translation, was shown to increase in amplitude and arrive back at the bubble sooner than the reverberant pressure which was calculated assuming a stationary source.

Chapter 5

Translation Near Tissue-like Media

With the bubble dynamics model implemented numerically and verified for accuracy, we turn our attention to the study of bubble dynamics near tissue-like media. The main focus of this chapter is the effect of the materials parameters of the viscoelastic medium on the reflected fields—specifically with regard to the reverberant pressure gradient, which is responsible for the direction of bubble translation. Thus, both the temporal dynamics of the bubble and the frequency spectrum of reverberant pressure gradient are analyzed for a freely oscillating bubble immersed in water and near various tissue-like media.

A simplified approach to the calculation of bubble translation is also presented in this chapter. We first show that low-amplitude bubble translation is correlated with the phase of the portion of the Green's function corresponding to the reverberant pressure gradient, $\widehat{g}_{\text{rev}}(\omega)$, at the natural frequency of the bubble, ω_0. We demonstrate that bubble translation is toward the interface when the phase of $\widehat{g}_{\text{rev}}(\omega_0)$ is in phase with bubble pulsation, and away from the interface when this portion of the Green's function is in antiphase with bubble pulsation. This approach is used to study direction of bubble translation for various (1) combinations of material parameters for the viscoelastic

medium, (2) standoff distances from the interface, and (3) shear viscosity of the liquid. We then identify combinations of these parameters which correlate with bubble translation directed away from the interface.

This simplified approach is presented for the three most common tissue models: the Voigt, Kelvin, and Maxwell models. For each model, it is shown that bubble translation away from the interface tends to occur when the real part of the complex shear modulus of the viscoelastic medium is greater than the magnitude of the imaginary part of the complex shear modulus (i.e., the loss factor) of either the fluid or the viscoelastic medium. While we implicitly assume a Voigt model in the dynamical equations for the viscoelastic medium presented in Section 2.2, the Kelvin and Maxwell models are shown to better describe the dynamics of tissue-like media.

5.1 Bubble Dynamics Near a Tissue-Like Medium

In the previous chapter, the material properties of the viscoelastic medium were chosen to correspond with either steel or air. The time-domain simulations of a freely oscillating bubble in water near these media was shown in Fig. 4.7. The simulation results display a correct change in oscillation frequency as well as bubble translation directed toward a rigid-like wall and away from a pressure-release surface. Both of these effects are due to the presence of the interface. In addition, the only computational difference between the simulations, which accounts for the difference in direction of bubble translation, is due to the reverberant pressure gradient. Thus, it is of interest to

compare the reverberant fields used in these simulations to better understand the mechanism responsible for the difference in direction of bubble translation.

In addition to the bubble dynamics shown in Fig. 4.7, the magnitude and phase of $\widehat{\phi}_{\text{rev}} = \partial \widehat{g}_{\text{rev}}/\partial z$ for both a water-air and water-steel interface were shown in the previous chapter (Figs. 4.4 and 4.5). These spectra were then used to produce simulations shown in Fig. 4.7, with a notable difference in direction of bubble translation. While the magnitudes of these spectra are virtually identical, the phase of the spectrum for the water-air interface is in antiphase with that for the water-steel interface. In other words, the magnitude of the force applied to the bubble due to the field created by the interface is almost identical in these two cases; however, the direction of the force created by the water-air interface is opposite that for the water-steel interface.

Near an interface formed by water and a tissue-like solid, the expectation is that the same reasoning applies; at a particular frequency, the spectrum of the reverberant pressure gradient (a complex function) supplies a magnitude and phase which determines the interaction of the bubble with the interface. If the phase of the spectrum of the reverberant pressure gradient is similar to that produced near a water-air interface, then we expect translation away from the interface. On the other hand, if the phase is closer to that for a water-steel interface, then we expect translation toward the interface. At an arbitrary frequency, the magnitude of the reverberant pressure gradient is thus responsible for the overall distance of translation, while the phase is responsible for the

direction it travels. Thus, we analyze the spectrum of the reverberant pressure gradient by taking a Fourier transform of Eq. (2.65):

$$\frac{\partial \widehat{p}_{\text{rev}}}{\partial z} = i\omega\rho_1 \int_{-\infty}^{\infty} \widehat{g}_{\text{rev}}\left[\omega; \mathbf{x}, \mathbf{X}(\tau)\right] Q(\tau) e^{i\omega\tau}\, d\tau\,. \tag{5.1}$$

Equation (5.1) reveals that the function to explore is $\widehat{g}_{\text{rev}}(\omega)$ since the volume velocity Q is an explicit bubble parameter. In addition, all of the effects due to the interface are contained in $\widehat{g}_{\text{rev}}(\omega)$. Therefore, instead of investigating the phase of the reverberant pressure gradient, the phase of $\widehat{g}_{\text{rev}}(\omega)$ is investigated in more detail.

Figure 5.1 shows $\widehat{g}_{\text{rev}}(\omega_0)$ a distance $22.5\,\mu\text{m}$[†] from a water-air interface, a water-steel interface, and various interfaces between water and a tissue-like medium. The material properties for water, air, and steel were given previously in Table 4.1. The tissue-like media are all assigned a density $\rho_2 = 1050\,\text{kg/m}^3$, compressional wave speed $c_2 = 1560\,\text{m/s}$, shear viscosity $\eta_2 = 5 \times 10^{-4}\,\text{Pa·s}$, and zero bulk viscosity. Young's modulus for the tissue-like media is varied from $E = 10^4\,\text{Pa}$ to $10^7\,\text{Pa}$. As in previous chapters, we normalize these spectra by Eq. (2.67) to emphasize the variations in amplitude and phase of $\widehat{g}_{\text{rev}}(\omega)$ in comparison to an image source. We reiterate that the frequency spectra are evaluated at very high frequencies so that the very small distance between the interface and the bubble center is resolved during time-domain simulations.

For a bubble of radius $3\,\mu\text{m}$, the natural frequency is within the region

[†]In this chapter, we principally consider a bubble with a $3\,\mu\text{m}$ radius. Using this particular bubble size, the distance from the interface is thus $7.5R_0$.

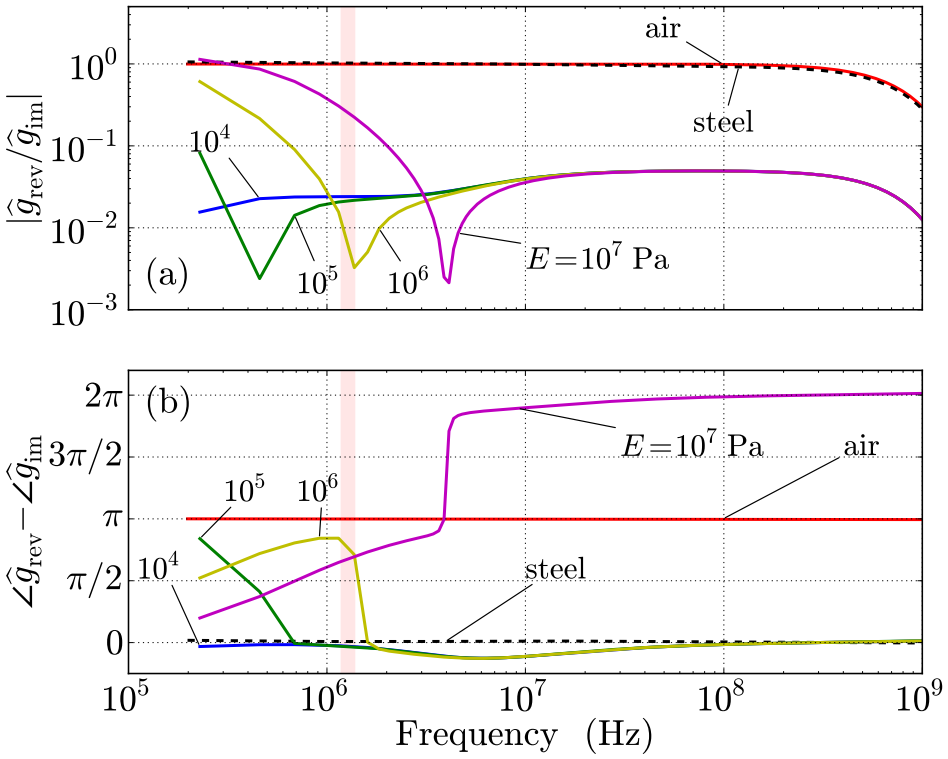

Figure 5.1: The (a) magnitude and (b) phase of $\widehat{g}_{\rm rev}(\omega)$, normalized with respect to Eq. (2.67), and calculated at distance 22.5 μm ($7.5R_0$ for $R_0 = 3\,\mu$m) from a water-air interface, a water-steel interface, and various interfaces between water and tissue-like media with varying shear modulus. Material properties for water, air, and steel are listed in Table 4.1. The tissue-like media all have density $\rho_2 = 1050\,\text{kg/m}^3$, compressional wave speed $c_2 = 1560\,\text{m/s}$, shear viscosity $\eta_2 = 5 \times 10^{-4}\,\text{Pa·s}$, and zero bulk viscosity. Young's modulus ranges from 10^4 Pa to 10^7 Pa. The region of the axes shaded in pink corresponds to the approximate location of the oscillation frequency of a bubble of radius 3 μm.

of the axes in Fig. 5.1 shaded in pink.[†] By analyzing low-amplitude free bubble

[†]We do not explicitly annotate where the natural frequency is since the bubble may oscillate at a different frequency, depending on the properties of the viscoelastic medium and its distance from the interface.

oscillation, the only frequency of interest in the spectrum presented in Fig. 5.1 is the oscillation frequency of the bubble. For an interface between water and soft tissue, this frequency is very close to the natural frequency of the bubble in free space, ω_0, since the reflected pressure field is very low in amplitude. Near ω_0, the phases of $\widehat{g}_{\text{rev}}(\omega)$ for $E = 10^4\,\text{Pa}$ and $10^5\,\text{Pa}$ align with that for a water-steel interface, while the phases of $\widehat{g}_{\text{rev}}(\omega)$ for $E = 10^6\,\text{Pa}$ and $10^7\,\text{Pa}$ are closer to that for a water-air interface. The issue regarding how the phase of $\widehat{g}_{\text{rev}}(\omega)$ is more like that for a water-air interface (instead of a water-steel interface) at higher Young's modulus is addressed later in this chapter. Currently, we are only concerned with how $\widehat{g}_{\text{rev}}(\omega)$ is correlated with direction of bubble translation—regardless of the chosen parameters.

Figure 5.2 displays the time-domain simulations of the bubble dynamics produced with the spectra shown in Fig. 5.1. We emphasize that the spectra shown in Fig. 5.1 are used to calculate the reverberant pressure gradient. The direction of bubble translation for the curves corresponding to $E = 10^4\,\text{Pa}$ and $10^5\,\text{Pa}$ is toward the interface. We note that the phase of $\widehat{g}_{\text{rev}}(\omega)$—at the natural frequency of the bubble—for the two curves align with that for a water-steel interface. On the other hand, the direction of bubble translation for the curves corresponding to $E = 10^6\,\text{Pa}$ and $10^7\,\text{Pa}$ is away from the interface. Again, we see that the phase of $\widehat{g}_{\text{rev}}(\omega_0)$ for these curves is similar to that for a water-air interface. In addition, overall translational distance is qualitatively described by the magnitudes of $\widehat{g}_{\text{rev}}(\omega)$, shown in Fig. 5.1(a). Only considering the frequency spectra calculated for an interface between water and a tissue-

like solid, the spectrum with the largest amplitude at the natural oscillation frequency of the bubble ($E = 10^7$ Pa) corresponds to the temporal simulation in Fig. 5.2(b) with the largest overall translation. While the magnitude of $\widehat{g}_{\text{rev}}(\omega_0)$ for $E = 10^6$ Pa in Fig. 5.1(a) is lower than those for $E = 10^4$ Pa or 10^5 Pa, the overall distance translated by the bubble is about the same. This is likely due to the fact that the reverberant field for $E = 10^6$ Pa is similar to that for a water-air interface, which facilitates a larger translation distance. This was seen in Fig. 4.7, where the overall distance traveled by a bubble near a water-air interface was more than that for a bubble near a water-steel interface. We point out that overall translation of the bubble for these simulations is quite small (less than a hundredth of a bubble radius); however, such a small amount of translation allows us to consider the bubble to be stationary—when computing the reverberant pressure and its gradient—thus simplifying the computation.

A comparison of the direction of bubble translation in Fig. 5.2(b) with the phase of $\widehat{g}_{\text{rev}}(\omega_0)$ in Fig. 5.1(b) is one example (of the many that have been tested) to show that the two parameters are connected. Thus, the direction of bubble translation may be determined more quickly by evaluating $\widehat{g}_{\text{rev}}(\omega)$ near the natural oscillation frequency of the bubble rather than performing the time-domain simulations. This is a substantial simplification of the study of bubble translation when $\widehat{g}_{\text{rev}}(\omega)$ must be computed numerically. A time-domain simulation already involves the computation of $\widehat{g}_{\text{rev}}(\omega)$ [and $\widehat{\phi}_{\text{rev}}(\omega)$] at a number of different frequencies, in addition to the numerical integration

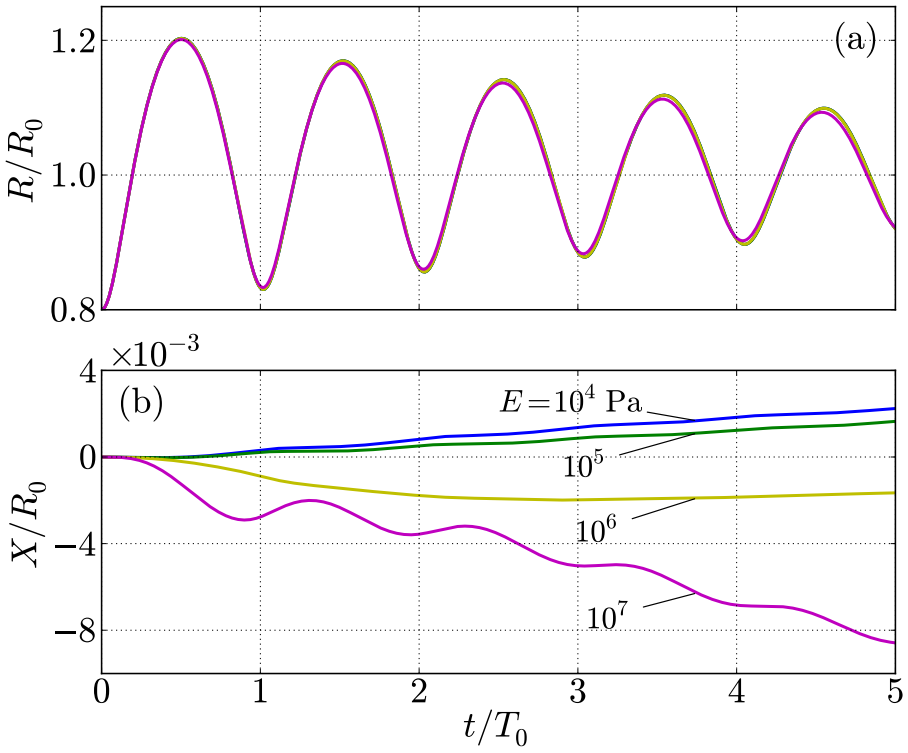

Figure 5.2: Bubble (a) pulsation and (b) translation calculated using the various frequency spectra in Fig. 5.1 for an interface between water and a tissue-like medium.

involved for the time-domain simulation itself. On the other hand, by evaluating only the phase of $\widehat{g}_{\text{rev}}(\omega_0)$, we eliminate the time-domain simulation altogether and calculate $\widehat{g}_{\text{rev}}(\omega)$ at a single frequency. This simplification allows us to evaluate several different combinations of material parameters for both the fluid and the viscoelastic medium, as well as vary the distance of the bubble from the interface, to ultimately draw a clearer picture with regard to direction of bubble translation. Indeed, by only calculating $\widehat{g}_{\text{rev}}(\omega_0)$ we were able to compute over 18,000 different simulations; performing this number of

time-domain simulations would, at best, take a little less than a month of computation time.

By only evaluating the phase of $\widehat{g}_{\text{rev}}(\omega)$ at a single frequency, the solution is theoretically relevant only for a stationary bubble in steady state. In other words, the effects present in a time-domain simulation due to the pulsation and translation of the bubble starting at rest, for example, are not present in this analysis. Thus, studying bubble translation within this context restricts us to low-amplitude pulsation, for which translation is sufficiently weak such that a single bubble location may be assumed when calculating $\widehat{g}_{\text{rev}}(\omega_0)$. We reiterate that this restriction is valid in Fig. 5.2, where the maximum distance traveled by the bubble for all the simulations presented is less than a hundredth of a bubble radius.[†] Since the time-domain simulations begin with the bubble at rest, they do not perfectly reflect the analysis gleaned from the phase of $\widehat{g}_{\text{rev}}(\omega_0)$. However, calculating $\widehat{g}_{\text{rev}}(\omega_0)$ is an appropriate first step to quickly determining the relation of material and bubble parameters with regard to direction of bubble translation.

5.2 Material Parameters

In order to compute $\widehat{g}_{\text{rev}}(\omega)$ at the natural frequency of the bubble, we must determine relevant ranges for the material parameters describing the

[†]Even for rigid and air-like boundaries, where the magnitude of $\widehat{g}_{\text{rev}}(\omega_0)$ is higher, the maximum distance traveled for a freely oscillating bubble at low amplitudes is approximately a tenth of a bubble radius (Fig. 4.7), and is a sufficiently small distance for this approximation.

viscoelastic medium. For tissue, these parameters can vary greatly, and depend strongly on frequency and the type of tissue. Tissue is characterized in several different ways, varying from standard mechanical compression tests[1] to acoustical characterization methods such as elastography,[72] shear wave elasticity imaging,[73] or exploitation of tissue inhomogeneities.[74] One advantage of an acoustical approach is that both tissue moduli and viscosity may be inferred, making it more comprehensive than mechanical tissue-characterization methods. Once the tissue has been measured, analytical[75] or computational[76] models can be fit to the data to determine the density, bulk and shear modulus, and bulk and shear viscosity.

Ranges of material parameters for soft tissue reported in the literature are highly frequency dependent. Low-frequency (hertz to kilohertz region) material parameters are ubiquitous in the literature;[1,72–76] however, they are likely inappropriate for the frequencies at which contrast agents resonate (i.e., around a megahertz). The reported material parameters at low megahertz frequencies can vary from those obtained at low frequencies (e.g., tens of kilohertz or lower) by several orders of magnitude.[77–80] We thus attempt to analyze several combinations of material parameters, using the phase of $\widehat{g}_{\mathrm{rev}}(\omega_0)$ as an indicator for finding relevant combinations which correspond to bubble translation away from the interface.

The values for density and compressional wave speed are taken from the those reported in Table 1 of Brujan et al.[1] These values describe six different tissue phantoms created by Brujan et al.,[1] and represent a range

of the differing types of tissue. We use these values to give six physically realizable combinations for these parameters. The parameters are provided here in Table 5.1. For soft tissue, the shear modulus is approximately one third

Medium	1	2	3	4	5	6
Density (kg/m^3)	1012	1032	1050	1073	1095	1123
Comp. wave speed (m/s)	1518	1560	1575	1605	1623	1634
Young's modulus (MPa)	0.017	0.124	0.252	0.405	1.04	2.03

Table 5.1: Density, longitudinal sound speed, and Young's modulus measured for six different tissue phantoms reported by Brujan et al.[1]

of Young's modulus: $\mu_2 = E/3$; thus, shear modulus may be inferred from Table 5.1 as well. However, because other work has shown this parameter to affect strongly the bubble translation,[1] the shear modulus (and shear viscosity) of the tissue-like solid are varied along the axes of the upcoming plots and are thus different at times than what is listed in Table 5.1. The bulk viscosity is set to zero since this parameter has a negligible effect on the results forthcoming.

5.2.1 The Voigt model

The majority of models that have been used to represent the viscoelastic properties of tissue are one of following three: the Voigt, Kelvin, or Maxwell model.[81] We implicitly assumed a Voigt model in the derivation of the dynamical equation for the viscoelastic medium presented in Section 2.2 [Eqs. (2.27) and (2.28)]; thus, we first study the phase of $\widehat{g}_{\text{rev}}(\omega_0)$ using this model. Figure 5.3 shows the mechanical systems representation of the dynamical behavior

of tissue for the Voigt model.[†] This model accounts for both compression and damping through the spring and dashpot, respectively. The dynamical equation for this mechanical system is

$$f = \mu_m u + \eta_m \frac{\partial u}{\partial t}\,, \tag{5.2}$$

where f is the force, u is the displacement, μ_m is the spring constant, and η_m is the coefficient of viscosity. We emphasize that μ_m and η_m have different units than those for μ_2 and η_2, respectively, though they play identical roles in describing the physics of their respective models. In the frequency domain, Eq. (5.2) becomes

$$\widehat{f} = (\mu_m - i\omega\eta_m)\widehat{u}\,, \tag{5.3}$$

and a complex spring constant may be defined as $\tilde{\mu}_m = \mu_m - i\omega\eta_m$. This complex spring constant is phenomenologically the same as $\tilde{\mu}_2$ [defined after Eq. (2.28)] for the viscoelastic medium.

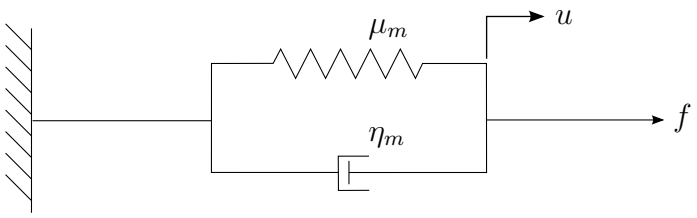

Figure 5.3: Mechanical systems representation of the Voigt model.

[†]The Voigt, Kelvin, and Maxwell models are all explained in Sec. (2.10) of Fung.[81]

If we use the Voigt model to describe the dynamics of the viscoelastic medium when calculating the phase of $\widehat{g}_{\text{rev}}(\omega_0)$, Fig. 5.4 shows the manner in which we quantify the results presented in later figures [Figs. 5.5–5.8]. Figure 5.4(a) is divided into two different sections by the black dashed line. The region shaded in pink represents a region where the magnitude of the imaginary component of the complex shear modulus (composed of the shear modulus and shear viscosity) of the viscoelastic medium is greater than its real component, $\text{Re}\{\tilde{\mu}_2\} < |\text{Im}\{\tilde{\mu}_2\}|$. Figure 5.4(b) is also divided into two sections; the region highlighted in pink in this figure describes where the magnitude of the complex shear modulus describing the fluid is greater than the real component of the complex shear modulus describing the viscoelastic medium, $\text{Re}\{\tilde{\mu}_2\} < |\,\tilde{\mu}_1|$. Because the complex shear modulus in the fluid is imaginary, the magnitude of the complex shear modulus for the fluid is equivalent to the magnitude of only the imaginary component. Thus, the regions shaded in pink in Figs. 5.4(a) and 5.4(b) both illustrate where the real part of the complex shear modulus for the viscoelastic medium is greater than the magnitude of the imaginary component of the complex shear moduli for either the viscoelastic medium or the fluid, respectively. These regions are indicated in Figures 5.5–5.8 as the white dashed lines overlaying the color plots which represent the phase of $\widehat{g}_{\text{rev}}(\omega_0)$.

Figures 5.5 to 5.8 show the phase of $\widehat{g}_{\text{rev}}(\omega)$ at the natural frequency of the bubble while we vary several different bubble and material parameters. The abscissa for all of these figures shows the shear viscosity of the viscoelastic

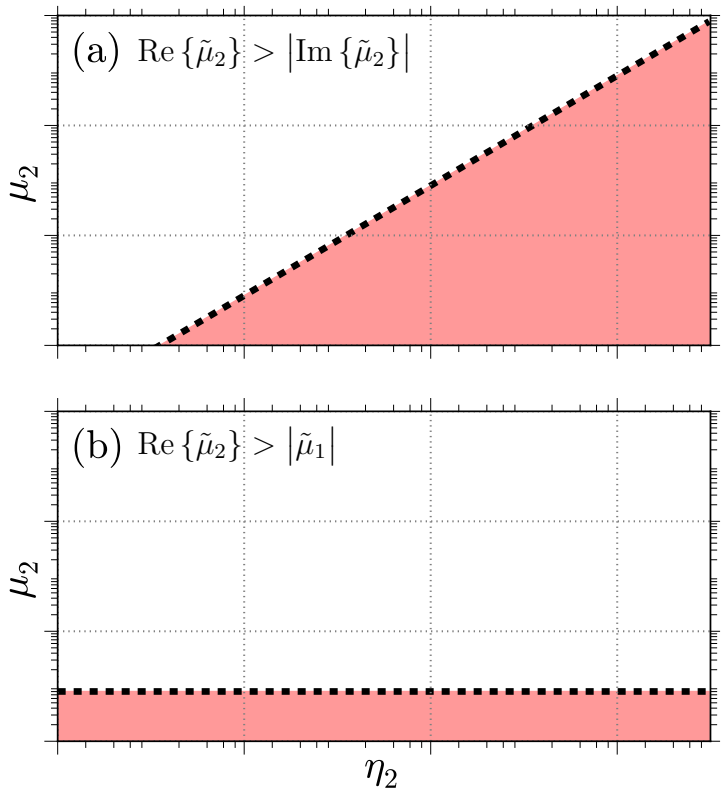

Figure 5.4: Illustration of typical regions seen in the following figures (Figs. 5.5–5.8) of the phase of $\widehat{g}_{\mathrm{rev}}(\omega)$, calculated using the Voigt model. The black dashed lines represent where (a) $\mathrm{Re}\{\tilde{\mu}_2\} = |\mathrm{Im}\{\tilde{\mu}_2\}|$ and (b) $\mathrm{Re}\{\tilde{\mu}_2\} = |\tilde{\mu}_1|$ and help to illustrate where bubble translation away from the interface generally occurs. These same regions are indicated by white dashed lines in Figures 5.5–5.8.

medium, which is varied logarithmically from 10^{-5} to 10^{2} Pa·s. The shear modulus along the ordinate varies logarithmically from 10^{3} to 10^{9} Pa. The ranges of these parameters cover the range of values reported in the literature for tissue,[73] and helps us correlate combinations of shear modulus and shear viscosity of the viscoelastic medium which correspond to bubble translation

away from the interface. We identify these combinations as the regions where the phase of $\widehat{g}_{\text{rev}}(\omega_0)$ is near π (regions of red in these figures). We note that this value of the phase is similar to that for a water-air interface and therefore bubble translation is directed away from the interface. Bubble translation in this direction is consistent with experiments involving bubbles immersed in a liquid and near soft-tissue.[1,3]

Each plot in Figs. 5.5–5.8 contains three subplots, where a single parameter is varied to show its effect on the phase of $\widehat{g}_{\text{rev}}(\omega_0)$. Figure 5.5 shows the evolution of the phase of $\widehat{g}_{\text{rev}}(\omega_0)$ for a bubble of radius $3\,\mu$m at distance $5R_0$ from the interface, while density and compressional wave speed are varied. Figure 5.5(a) shows the phase of $\widehat{g}_{\text{rev}}(\omega_0)$ for the least dense medium, which also has the slowest compressional wave speed and which values are closest to the respective values of density and sound speed for water (listed in Table 4.1). As reported by others,[1] direction of bubble translation away from the interface is a function of shear modulus. At a constant shear viscosity, the entire range of shear modulus in any subplot shows the effect of the shear modulus on direction of bubble translation. For negligible shear viscosity in the viscoelastic medium, Fig. 5.5(a) shows that bubble translation away from the interface occurs when the shear modulus is approximately between $\mu_2 = 10^4\,\text{Pa}$ and $10^6\,\text{Pa}$. While these values are somewhat higher than those reported by Brujan et al.,[1] the natural frequency of the bubble sized used here is several orders of magnitude higher,[†] and therefore increases the expected

[†]This assumes that the laser-generated bubbles used by Brujan et al.[1] are measured

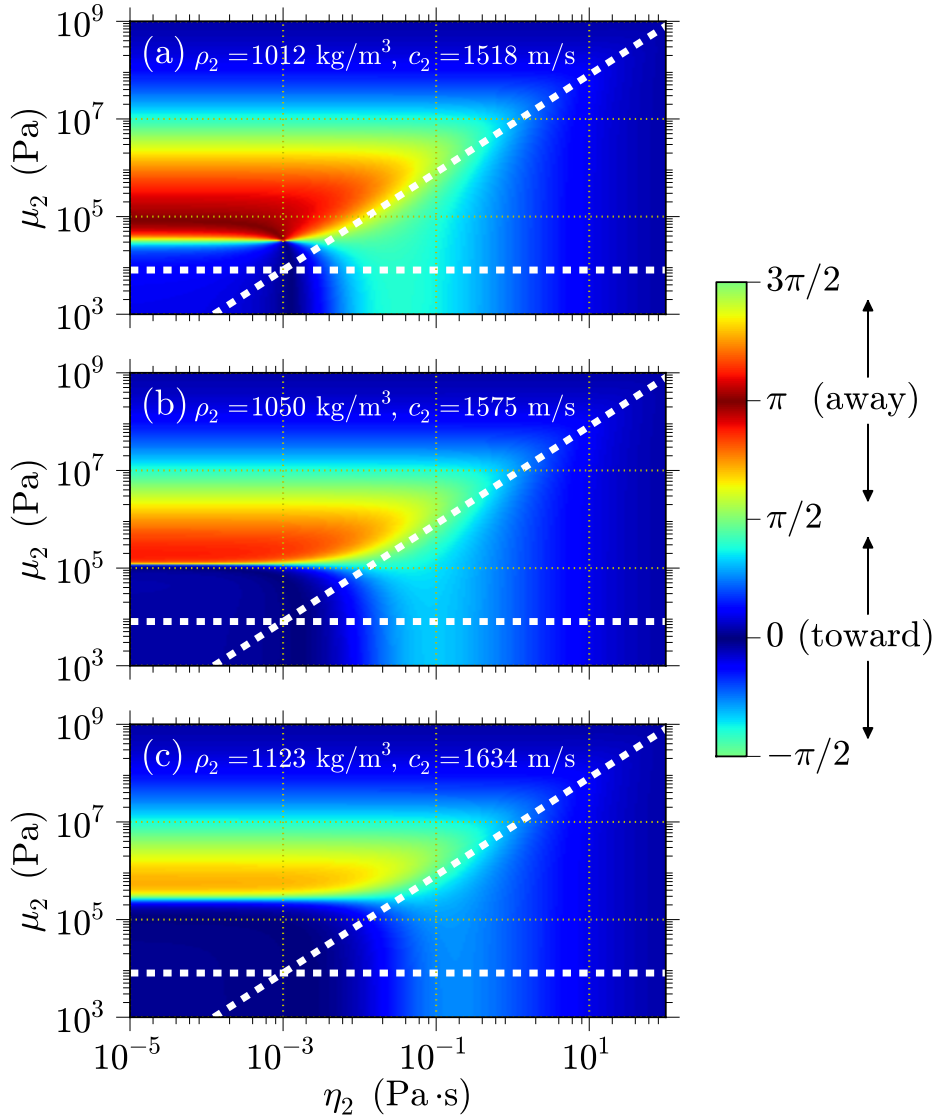

Figure 5.5: The phase of $\widehat{g}_{\text{rev}}(\omega_0)$ for a bubble of radius $3\,\mu$m immersed in water a distance $5R_0$ from a viscoelastic medium (Voigt) with varying density and compressional wave speed. Various shades of blue or red correspond to bubble translation toward or away from the interface, respectively.

after they have been generated by the laser and expanded to an equilibrium state, close to a millimeter.

value of the shear modulus.[3,82] The important effect of the shear viscosity of the viscoelastic medium on the phase of $\widehat{g}_{\text{rev}}(\omega)$ is seen by analyzing its range of values for a constant shear modulus. For all of the plots in Fig. 5.5, we note that the effect of the shear viscosity of the viscoelastic medium on direction of bubble translation is negligible until its value—multiplied by the natural frequency of the bubble—is approximately equal to the shear modulus. This value, $\omega_0\eta_2 = |\text{Im}\{\tilde{\mu}_2\}|$, is equal to the shear modulus of the viscoelastic medium along the diagonal, white, dashed line. When this value is greater than a given shear modulus, the phase of $\widehat{g}_{\text{rev}}(\omega_0)$ is near zero and bubble translation is consequently directed toward the interface. Thus, bubble translation away from the interface occurs when the shear viscosity of the tissue-like solid is less than approximately 10^{-3} Pa·s and its shear modulus falls between 10^4 to 10^6 Pa. As the density and sound speed increase [Figs. 5.5(b) and 5.5(c)], this region of phase corresponding to bubble translation away from the interface diminishes. We note that medium 6 of Table 5.1, used to define the material properties of the viscoelastic medium in Fig. 5.5(c), only represents about a 12% increase in the density over that of water and a 10% greater sound speed. Thus, the density and compressional wave speed of the viscoelastic medium must be closely matched to those of the liquid for bubble translation away from the interface to be observed—as is the case with soft tissue.

Another parameter shown to induce significant variance in the direction of bubble translation is the distance of the bubble from the interface.[1,3] Figure 5.6 shows the phase of $\widehat{g}_{\text{rev}}(\omega_0)$ for a bubble of radius 3 μm at distances

ranging from R_0 to $10R_0$ from the interface. Because we are interested in a soft-tissue interface, we consider the viscoelastic medium to be as soft as possible; however, the trends for more dense viscoelastic media display the same trends. As with the previous figure, the values for water are given in Table 4.1. Figure 5.6 shows that the red regions of the plot, corresponding to the regions where $\widehat{g}_{\text{rev}}(\omega_0)$ is near π (i.e., where bubble translation is directed away from the interface), move to higher values of shear modulus for distances farther from the interface. Thus, we note that bubble translation can change direction entirely depending on the distance of the bubble from the interface.[†] Even for much larger distances (e.g., $100R_0$), a region of the phase of $\widehat{g}_{\text{rev}}(\omega_0)$ exhibits combinations of μ_2 and η_2 which correspond to bubble translation away from the interface; however, at distances this large the magnitude of $\widehat{g}_{\text{rev}}(\omega_0)$ is insignificant, apart from the fact that the combination of values are likely unachievable.

The next parameter varied is the bubble size, which affects the natural frequency of the bubble. Figure 5.7 shows the phase of $\widehat{g}_{\text{rev}}(\omega_0)$ for an equilibrium bubble radius ranging from $3\,\mu$m to $300\,\mu$m. For all of these plots the bubble is located at distance $2.5R_0$ from the interface and the tissue-like solid is given the density and sound speed parameters listed for medium 1 in Table 5.1. The values for water are, again, those listed in Table 4.1. From smallest to largest, the considered bubble radii correspond to natural frequencies

[†]This was also observed by Brujan et al.;[1] see their Fig. 12.

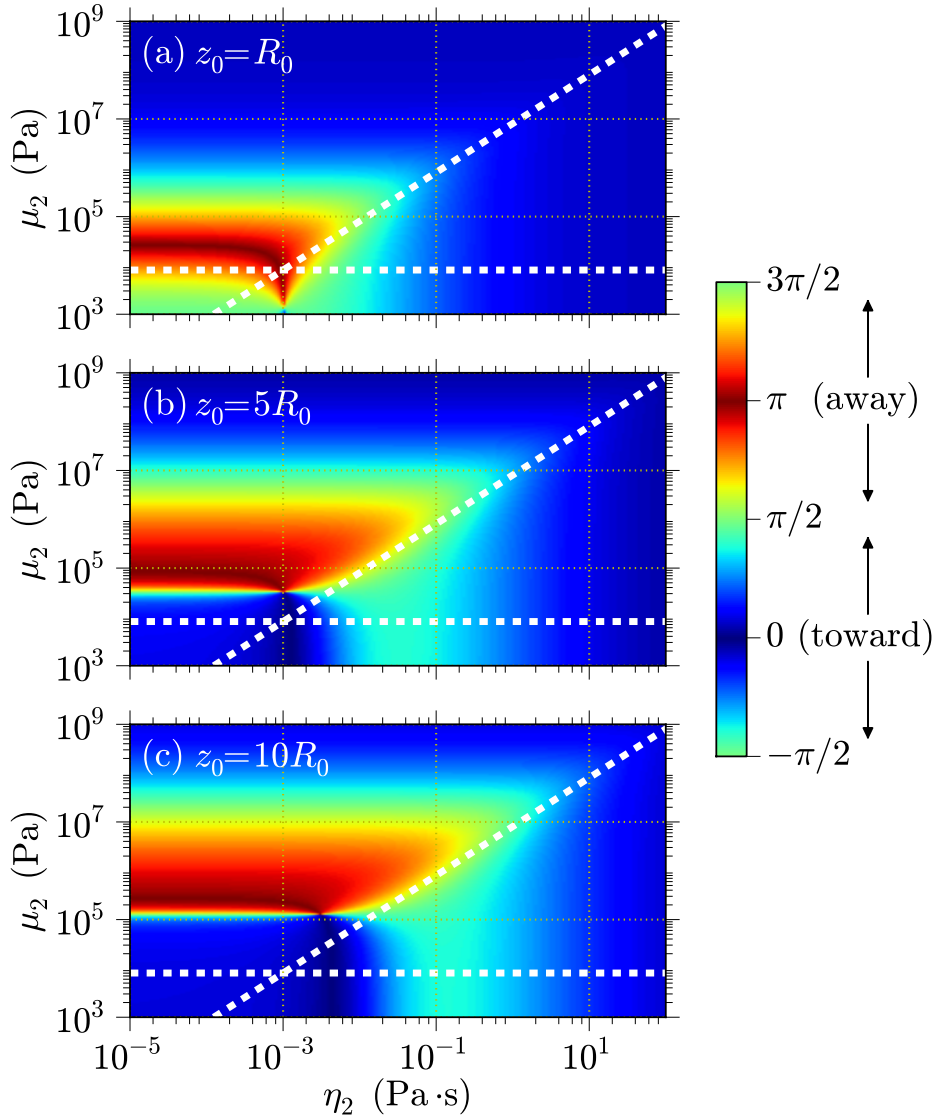

Figure 5.6: The phase of $\widehat{g}_{\text{rev}}(\omega_0)$ for a bubble of radius $3\,\mu$m immersed in water and at varying distances from a viscoelastic medium (Voigt) with density $\rho_2 = 1012\,\text{kg/m}^3$ and compressional wave speed $c_2 = 1518\,\text{m/s}$ (material 1 of Table 5.1). Various shades of blue or red correspond to bubble translation toward or away from the interface, respectively.

of approximately 1.28 MHz, 111.5 kHz, and 10.9 kHz.[†] As the bubble radius increases, the region of viable shear moduli—corresponding to bubble translation away from the interface—shifts to slightly lower values. The range of shear viscosity values corresponding to bubble translation away from the interface increases for larger bubble radius. This increase is a direct consequence of the lower natural frequency, which therefore requires a larger shear viscosity before the product of $\omega_0\eta_2$ is again equivalent to a given shear modulus. We also note that Fig. 5.7(c) does not contain a region where the phase is almost exactly π (the darkest red), as seen in Fig. 5.7(a).

The final parameter varied while using the Voigt model is the value of the shear viscosity of the fluid. Figure 5.8 illustrates the phase of $\widehat{g}_{\text{rev}}(\omega_0)$ for a bubble of radius 3 μm immersed in water with fluid shear viscosity ranging from $\mu_1 = 10^{-9}$ Pa·s to 10^{-1} Pa·s. The bubble is located at distance $2.5R_0$ from a viscoelastic medium with density $\rho_2 = 1012\,\text{kg/m}^3$ and compressional wave speed $c_2 = 1518\,\text{m/s}$ (material 1 of Table 5.1). Fluid viscosity significantly alters the range of the shear modulus associated with bubble translation away from the interface. As the fluid viscosity increases, this region narrows substantially, and seems to converge to the horizontal white line—indicating where the fluid viscosity times the oscillation frequency of the bubble, $\omega_0\eta_1 = |\tilde{\mu}_1|$, is equal to the shear modulus of the viscoelastic medium. Generally, μ_2 corresponding to a phase of $\widehat{g}_{\text{rev}}(\omega_0)$ near π occurs when it is larger than $\omega_0\eta_1$.

[†] The horizontal, white dashed line does not appear in Figs. 5.7(b) and 5.7(c) because $\omega_0\eta_1$ is less than 10^3 Pa.

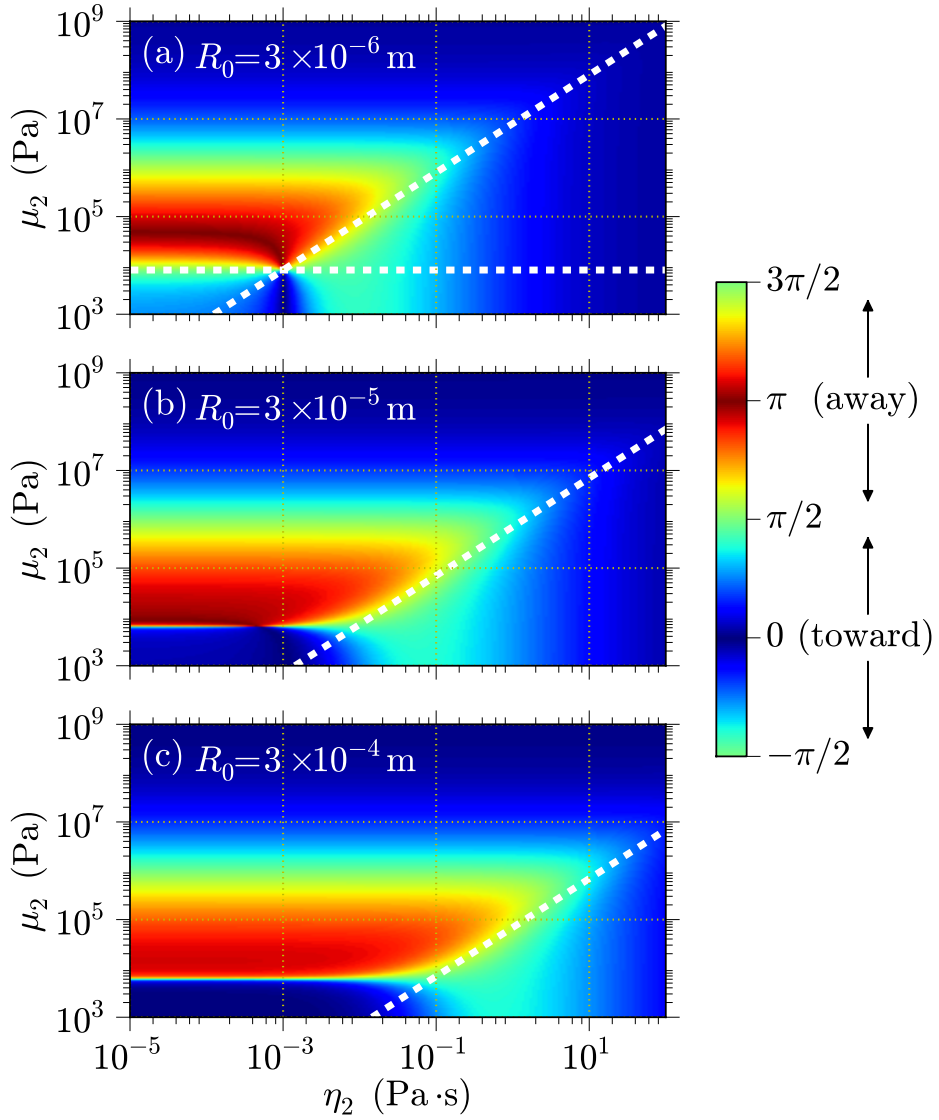

Figure 5.7: The phase of $\widehat{g}_{\text{rev}}(\omega_0)$ for a bubble of varying radius immersed in water and near a viscoelastic medium (Voigt) with density $\rho_2 = 1012\,\text{kg/m}^3$ and compressional wave speed $c_2 = 1518\,\text{m/s}$ (material 1 of Table 5.1) at distance $2.5R_0$ from the interface. Various shades of blue or red correspond to bubble translation toward or away from the interface, respectively.

While there is a small region in Fig. 5.8(c) where the phase of $\widehat{g}_{\text{rev}}(\omega_0)$ indicates bubble translation away from the interface outside of the upper left quadrant created by the white lines, this occurs where the shear viscosity of the liquid and tissue-like solid are equal, and corresponds to a very low magnitude of $\widehat{g}_{\text{rev}}(\omega_0)$.

In summary, bubble translation away from the interface frequently occurs under two conditions: (1) $\text{Re}\{\tilde{\mu}_2\} > \left|\tilde{\mu}_1\right|$ and (2) $\text{Re}\{\tilde{\mu}_2\} > \left|\text{Im}\{\tilde{\mu}_2\}\right|$, ultimately restricting values of μ_2 and η_2—which correspond to bubble translation away from the interface—to the upper left quadrant created by the white lines in Figs. 5.5–5.8. Visually, this is the region that is not pink after overlaying Figs. 5.4(a) and 5.4(b). While this is not a sufficient condition for bubble translation away from the interface, it seems to be generally necessary—assuming, of course, that the viscoelastic medium is accurately represented by the Voigt model.

5.3 Alternative Tissue Models

While the form of the complex shear modulus, $\tilde{\mu}_2 = \mu_2 - i\omega\eta_2$, is consistent with that presented for the Voigt model, it does not contain two important features observed in experiments. First, experiments have shown that the shear viscosity (i.e., the magnitude of $\text{Im}\{\tilde{\mu}_2/\omega\}$) of the tissue decreases as frequency increases,[77] which is the exact opposite of what the Voigt model predicts. Second, experiments also show that the shear modulus of the tissue increases as frequency increases,[82] whereas the shear modulus remains

constant using the Voigt model. Because of these inconsistencies, we consider other models that address these issues, the first of which is the Kelvin model.

5.3.1 The Kelvin model

Figure 5.9 depicts the one-dimensional mechanical systems representation of the Kelvin model. This model differs from the Voigt model due to the extra spring $\mu_{m,M}$ included with the dashpot η_m. In the frequency domain, the dynamical expression relating displacement to force using the Kelvin model is

$$\begin{aligned}\widehat{f} &= \left(\mu_m - \frac{i\omega\eta_m}{1 - i\omega\tau}\right)\widehat{u} \\ &= \left(\mu_m + \mu_{m,M}\frac{(\omega\tau)^2}{1+(\omega\tau)^2} - i\mu_{m,M}\frac{(\omega\tau)}{1+(\omega\tau)^2}\right)\widehat{u}\,, \end{aligned} \tag{5.4}$$

where $\tau = \eta_m/\mu_{m,M}$. As frequency becomes large enough such that $\omega\tau \gg 1$, then Eq. (5.4) becomes purely governed by the stiffness of the springs, increasing the effective stiffness of the entire system by $\mu_{m,M}$, and eliminating the damping of the system:

$$\widehat{f} = (\mu_m + \mu_{m,M})\,\widehat{u}\,. \tag{5.5}$$

When the frequency or shear viscosity become small enough such that $\omega\tau \ll 1$, Eq. (5.4) reduces to the Voigt model [Eq. (5.3)]. These limits better describe the dynamics of tissue observed in experiment since at high frequencies the stiffness increases and damping decreases. Thus, we incorporate the Kelvin model into the model presented in Section 2.3 by letting

$$\tilde{\mu}_2 = \mu_2 + \mu_{2,M}\frac{(\omega\tau)^2}{1+(\omega\tau)^2} - i\mu_{2,M}\frac{(\omega\tau)}{1+(\omega\tau)^2}\,, \tag{5.6}$$

where now $\tau = \eta_2/\mu_{2,M}$.

Figure 5.10 shows an illustration similar to that in Fig. 5.4, but for the Kelvin model. By modifying the definition of $\tilde{\mu}_2$ to be consistent with the Kelvin model, we note that the straight lines in Fig. 5.4 now decay for higher values of shear viscosity. Hence, one consequence of employing the Kelvin model is that higher values of the shear viscosity of the viscoelastic medium now contain regions where $\left|\tilde{\mu}_1\right| < \mathrm{Re}\left\{\tilde{\mu}_2\right\}$ and $\left|\mathrm{Im}\left\{\tilde{\mu}_2\right\}\right| < \mathrm{Re}\left\{\tilde{\mu}_2\right\}$ (i.e., the conditions of the Voigt model which correspond to bubble translation away from the interface). We reiterate that these two conditions (while employing the Voigt model) where met for almost all of the regions correlated to bubble translation away from the interface in Figs. 5.5–5.8. These conditions for the Kelvin model are indicated by white lines in the subsequent figures [Figs. 5.11–5.15], to again help correlate direction of bubble translation with specific ranges of material parameters for the viscoelastic medium.

Figures 5.11–5.15 show the phase of $\widehat{g}_{\mathrm{rev}}(\omega_0)$ for several variations of material/bubble parameters. However, before we alter the same parameters varied in Figs. 5.5–5.8, we first analyze the effect of the new parameter $\mu_{2,M}$. All six plots in Fig. 5.11 show the phase of $\widehat{g}_{\mathrm{rev}}(\omega_0)$ for a bubble of radius $3\,\mu$m, located at distance $5R_0$ from the interface. The density and sound speed of the viscoelastic medium are $\rho_2 = 1012\,\mathrm{kg/m^3}$ and $c_2 = 1518\,\mathrm{m/s}$, respectively (material 1 of Table 5.1). The new stiffness parameter $\mu_{m,M}$ is varied from $1.1 \times 10^4\,\mathrm{Pa}$ to $10^9\,\mathrm{Pa}$, where the specific values are listed on each plot in Fig. 5.11. As $\mu_{2,M}$ becomes large, the quantity $\omega\tau$ in Eq. (5.4)

becomes insignificant and the Kelvin model converges to the Voigt model; this is observed as the phase of $\widehat{g}_{\text{rev}}(\omega_0)$ in Fig. 5.11(f) converges to that shown in Fig. 5.6(b), where we had assigned identical material parameters, but employed the Voigt model.

In order to present the phase of $\widehat{g}_{\text{rev}}(\omega_0)$ for the Kelvin model in a similar format to that in Figs. 5.5–5.8, we must choose a single value for $\mu_{2,M}$. Because this parameter defines additional stiffness for the viscoelastic medium at high frequencies, we choose its value such that the equivalent stiffness (i.e., $\mu_2 + \mu_{2,M}$) is similar to what is reported in the literature at low-megahertz frequencies. Thus, if we consider the analysis around a megahertz, the equivalent stiffness is in the range of 0.1 MPa to 10 MPa.[78,79] Because this range of values is orders of magnitude larger than the corresponding values reported for lower frequencies, the parameter $\mu_{2,M}$ must therefore be much larger than μ_2—essentially corresponding to the values reported in the literature at megahertz frequencies. Thus, Figs. 5.11(b) and 5.11(c) correspond most closely with the values reported in the literature, and the remainder of the figures presented for the Kelvin model are therefore assigned $\mu_{m,M} = 1.3\,\text{MPa}$.

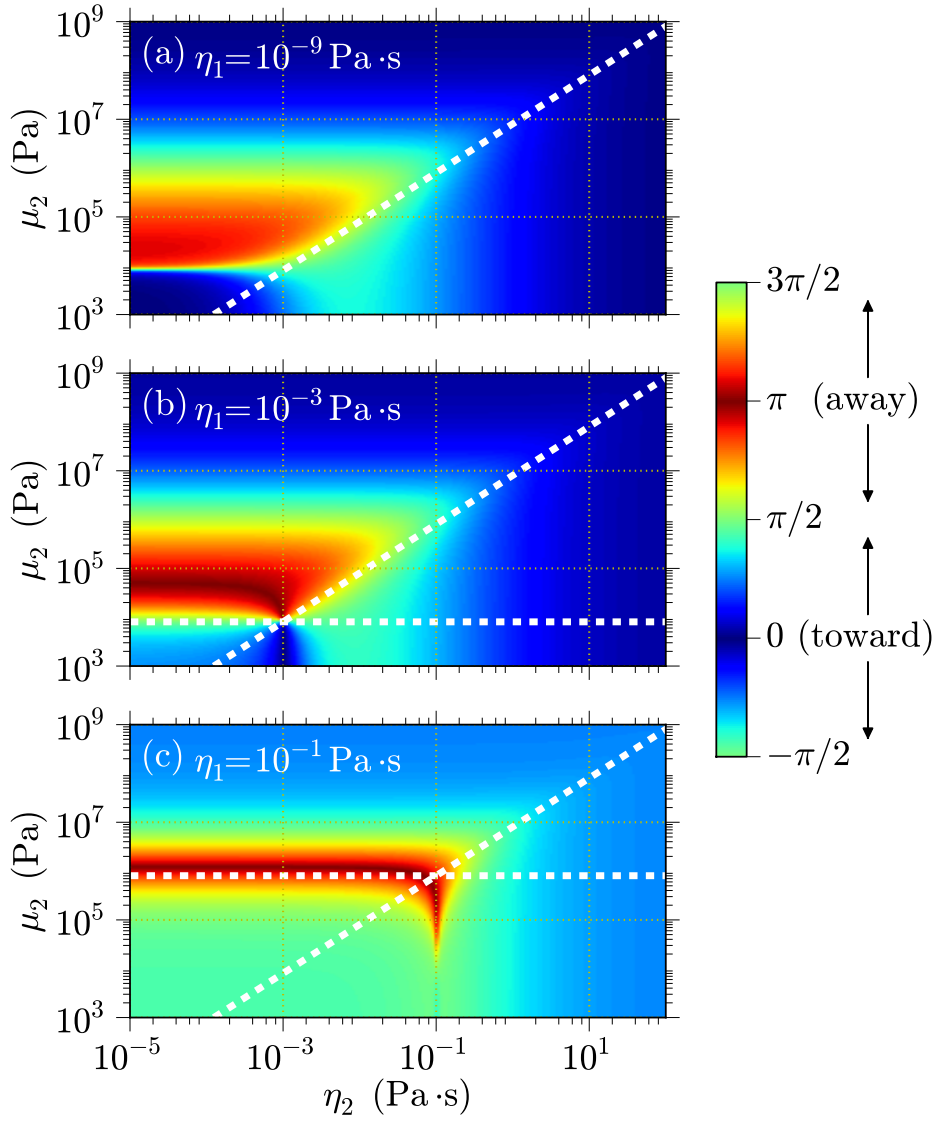

Figure 5.8: The phase $\widehat{g}_{\text{rev}}(\omega_0)$ for a bubble of radius 3 μm immersed in water with varying shear viscosity and near a viscoelastic medium (Voigt) with density $\rho_2 = 1012\,\text{kg/m}^3$ and compressional wave speed $c_2 = 1518\,\text{m/s}$ (material 1 of Table 5.1) at distance $2.5R_0$ from the interface. Various shades of blue or red correspond to bubble translation toward or away from the interface, respectively.

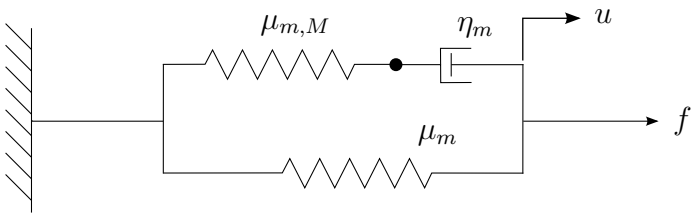

Figure 5.9: Mechanical systems representation of the Kelvin model.

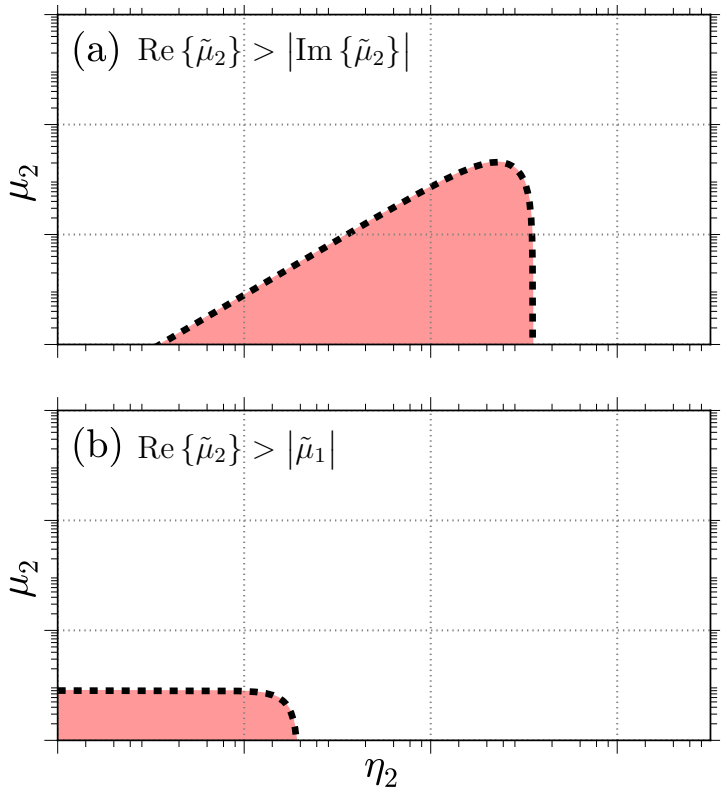

Figure 5.10: Illustration of typical regions seen in the following figures of the phase of $\widehat{g}_{\mathrm{rev}}(\omega_0)$ using the Kelvin model [Figs. 5.11–5.15]. The black dashed lines represent where (a) $\mathrm{Re}\{\tilde{\mu}_2\} = |\mathrm{Im}\{\tilde{\mu}_2\}|$ and (b) $\mathrm{Re}\{\tilde{\mu}_2\} = |\tilde{\mu}_1|$ and help to define regions where bubble translation away from the interface generally occurs. These same regions are indicated by the white dashed lines in Figures 5.11–5.15.

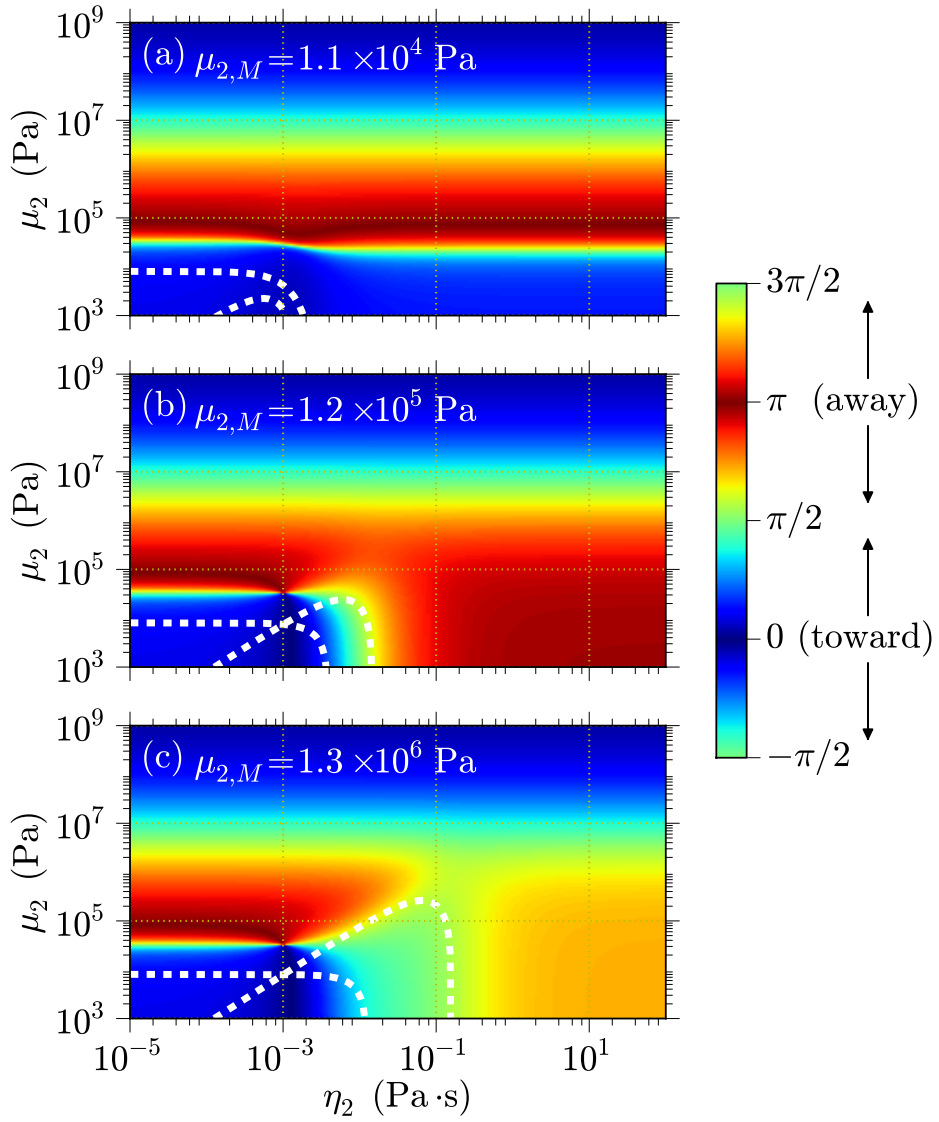

Figure 5.11: The phase of $\widehat{g}_{\text{rev}}(\omega_0)$ for a bubble of radius $3\,\mu$m immersed in water and a distance $5R_0$ from a viscoelastic medium (Kelvin) with density $\rho_2 = 1012\,\text{kg/m}^3$ and compressional wave speed $c_2 = 1518\,\text{m/s}$ (material 1 of Table 5.1) while $\mu_{m,M}$ is varied. Various shades of blue or red correspond to bubble translation toward or away from the interface, respectively. Plots continue on the next page.

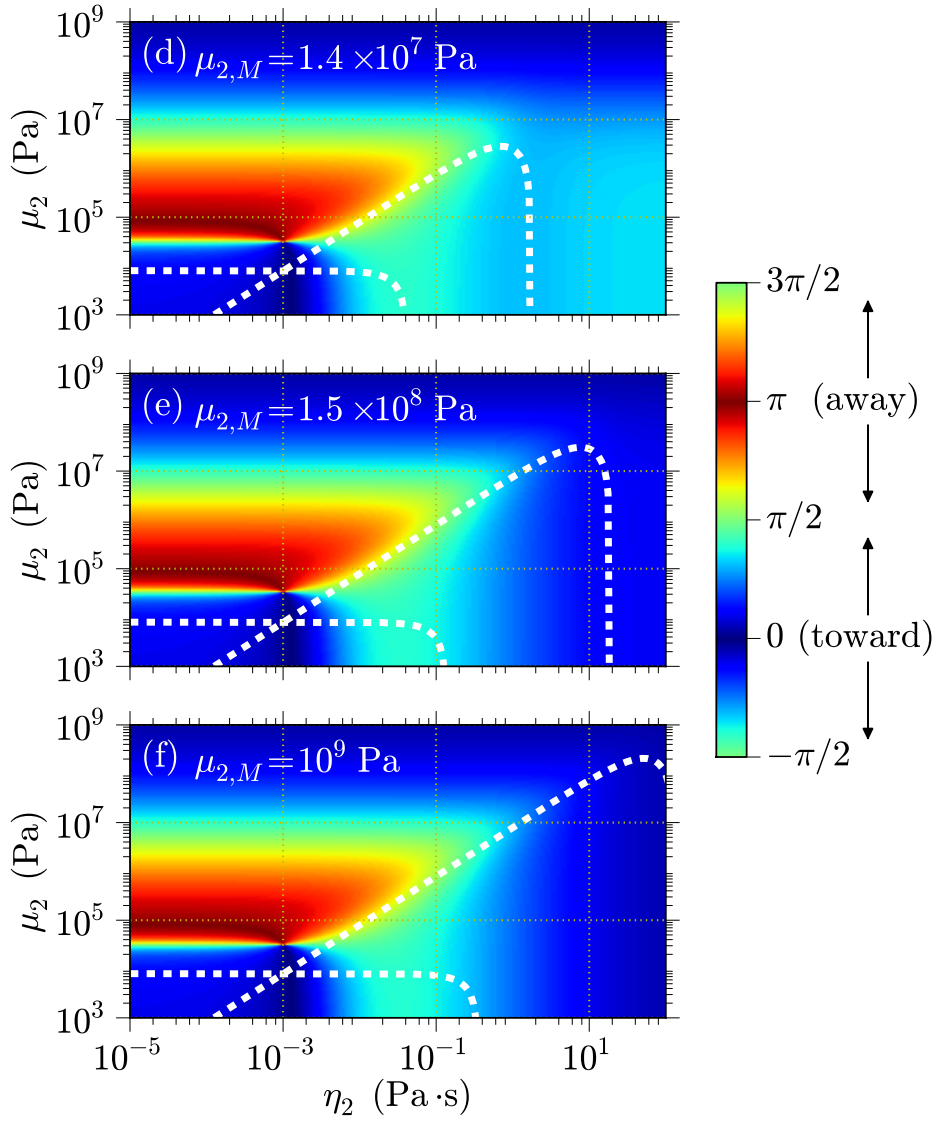

Figure 5.11: Plots continued from the previous page.

As with the Voigt model, the first parameters varied are the density and compressional wave speed of the viscoelastic medium. Figure 5.12 displays the phase of $\widehat{g}_{\text{rev}}(\omega_0)$ for a bubble of radius $3\,\mu$m, located at distance $5R_0$ from an interface between water and a viscoelastic medium with varying density and compressional wave speeds. As shown in Fig. 5.5, the increase in density and sound speed in Fig. 5.12 gradually diminishes the region where bubble translation away from the interface is expected. The regions of Fig. 5.12 which correspond to bubble translation away from the interface are much broader than those for the corresponding figure of the Voigt model [Fig. 5.5]. These regions, in the left half of both Figs. 5.5 and 5.12, are nearly identical; however, Fig. 5.12 shows an additional region which corresponds to bubble translation away from interface with high shear viscosity and low shear modulus (the orange region in the bottom right corner of each plot in Fig. 5.12).

Figure 5.13 shows the phase of $\widehat{g}_{\text{rev}}(\omega_0)$ for a bubble of radius $3\,\mu$m immersed in water at distances ranging from $2.5R_0$ to $7.5R_0$ from a viscoelastic medium with density $\rho_2 = 1012\,\text{kg/m}^3$ and compressional wave speed $c_2 = 1518\,\text{m/s}$ (material 1 of Table 5.1). An interesting feature of the Kelvin model for varying distance is that the lower-right corner of each plot (corresponding to high shear viscosity and low shear modulus in the viscoelastic medium) changes phase fairly uniformly as the bubble moves farther from the interface. More specifically, while the phase in the region where $\eta_2 > 10^{-1}\,\text{Pa·s}$ and $\mu_2 < 10^6\,\text{Pa}$ is approximately $\pi/2$ when the bubble is at distance $2.5R_0$ from the interface, the phase becomes roughly $3\pi/4$ at distance $7.5R_0$ from the

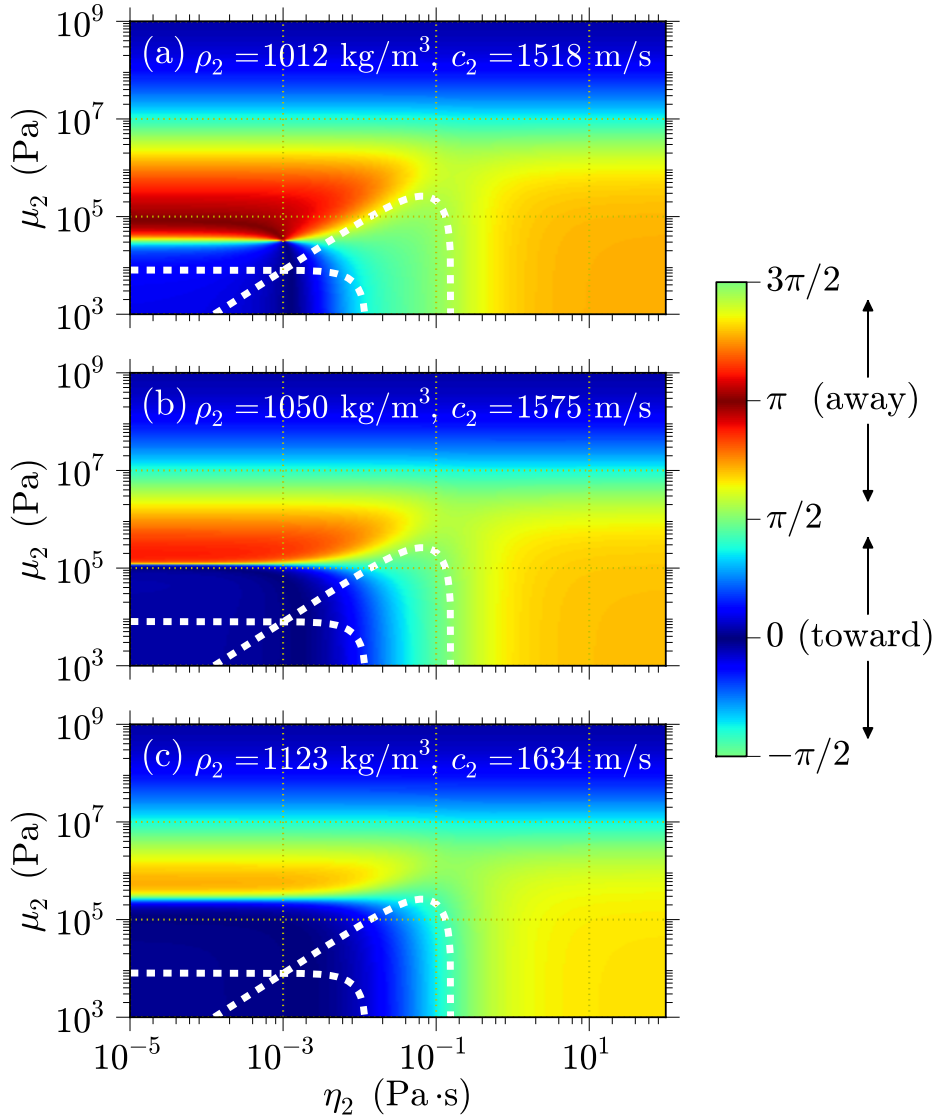

Figure 5.12: The phase of $\widehat{g}_{\text{rev}}(\omega_0)$ for a bubble of radius 3 μm immersed in water and at distance $5R_0$ from a viscoelastic medium (Kelvin) with varying density and compressional wave speed. Various shades of blue or red correspond to bubble translation toward or away from the interface, respectively.

interface. The phase of $\widehat{g}_{\text{rev}}(\omega_0)$ corresponding to bubble translation away from the interface—located up and to the left of the pink region in Fig. 5.10—behaves like Fig. 5.6, where bubble distance was varied using the Voigt model.

Figure 5.14 shows the phase of $\widehat{g}_{\text{rev}}(\omega_0)$ for a bubble of varying size, where the bubble is immersed in water and located at distance $5R_0$ from a viscoelastic medium with density $\rho_2 = 1012\,\text{kg/m}^3$ and compressional wave speed $c_2 = 1518\,\text{m/s}$ (material 1 of Table 5.1). Comparable to Fig. 5.7, when the bubble radius increases, the frequency ω_0 decreases. Hence, for larger R_0, the region where the shear viscosity of the viscoelastic medium corresponds to bubble translation away from the interface expands to include higher values of shear viscosity.

Last, Fig. 5.15 displays the phase of $\widehat{g}_{\text{rev}}(\omega_0)$ for a bubble of radius $3\,\mu\text{m}$, located a distance $5R_0$ from an interface between water with varying shear viscosity and a viscoelastic medium with density $\rho_2 = 1012\,\text{kg/m}^3$ and compressional wave speed $c_2 = 1518\,\text{m/s}$ (material 1 of Table 5.1). For $\eta_2 < 10^{-3}\,\text{Pa·s}$, Fig. 5.15 is similar to Fig. 5.8; as the shear viscosity of the liquid increases, the region where the phase of $\widehat{g}_{\text{rev}}(\omega_0)$ corresponds to bubble translation away from the interface narrows. In addition, for higher fluid viscosity, this region occurs nearer to the white dashed line, where the magnitude of the complex shear modulus in the fluid is equal to the real part of the complex shear modulus in the viscoelastic medium, $\text{Re}\,\{\tilde{\mu}_2\} = |\,\tilde{\mu}_1|$. The phase of $\widehat{g}_{\text{rev}}(\omega_0)$ corresponding to bubble translation away from the interface for $\eta_2 > 10^{-1}\,\text{Pa}$ becomes similar to the phase of $\widehat{g}_{\text{rev}}(\omega_0)$ seen for a water-air interface as the shear viscosity in

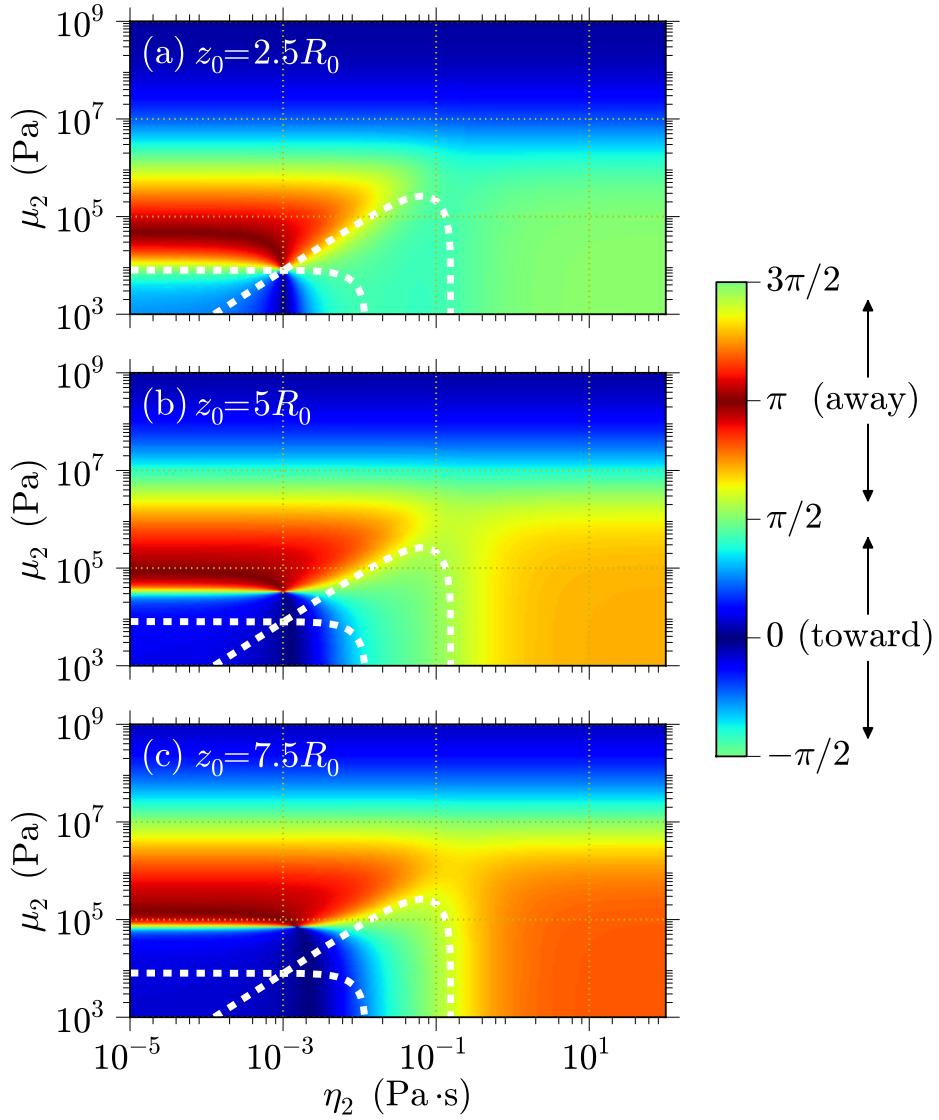

Figure 5.13: The phase of $\widehat{g}_{\text{rev}}(\omega_0)$ for a bubble of radius 3 μm immersed in water at varying distances from a viscoelastic medium (Kelvin) with density $\rho_2 = 1012\,\text{kg/m}^3$ and compressional wave speed $c_2 = 1518\,\text{m/s}$ (material 1 of Table 5.1). Various shades of blue or red correspond to bubble translation toward or away from the interface, respectively.

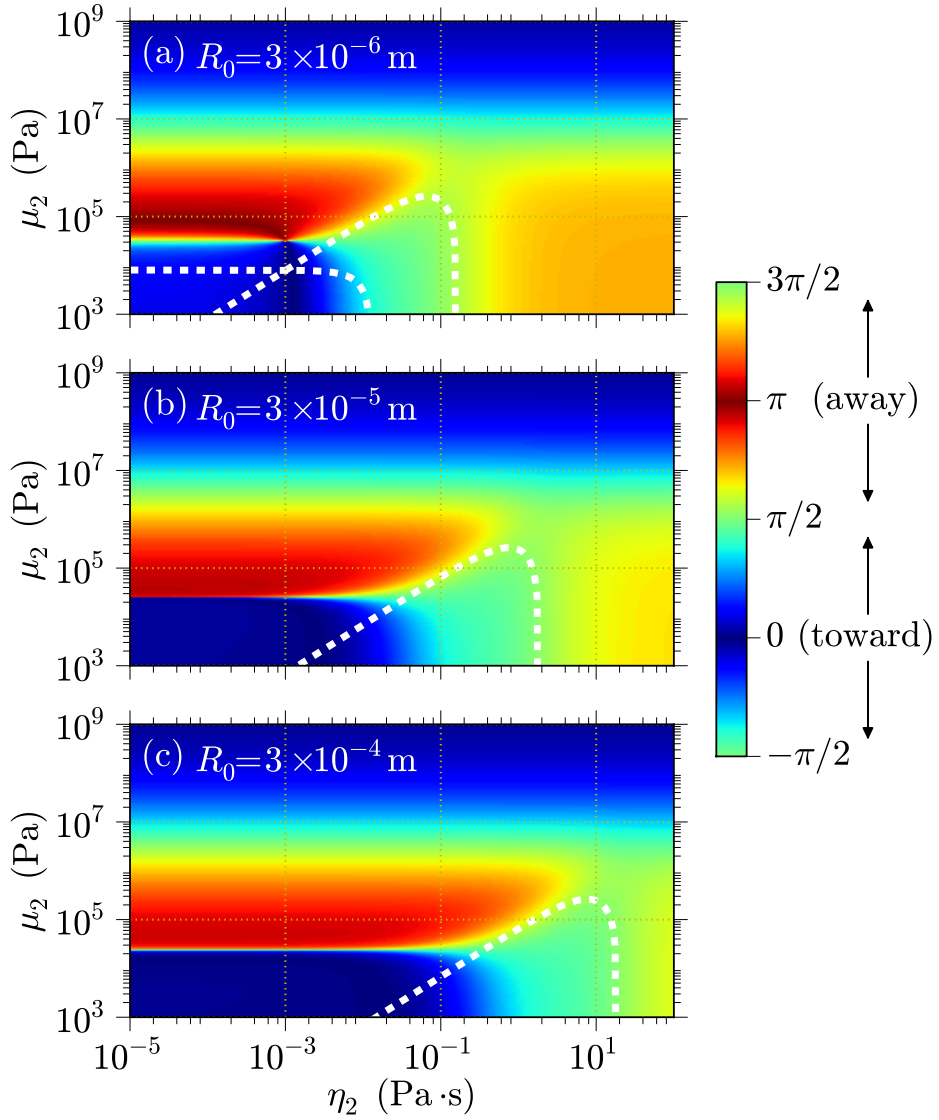

Figure 5.14: The phase of $\widehat{g}_{\text{rev}}(\omega_0)$ for a bubble of varying radius immersed in water and at distance $5R_0$ from a viscoelastic medium (Kelvin) with density $\rho_2 = 1012\,\text{kg/m}^3$ and compressional wave speed $c_2 = 1518\,\text{m/s}$ (material 1 of Table 5.1). Various shades of blue or red correspond to bubble translation toward or away from the interface, respectively.

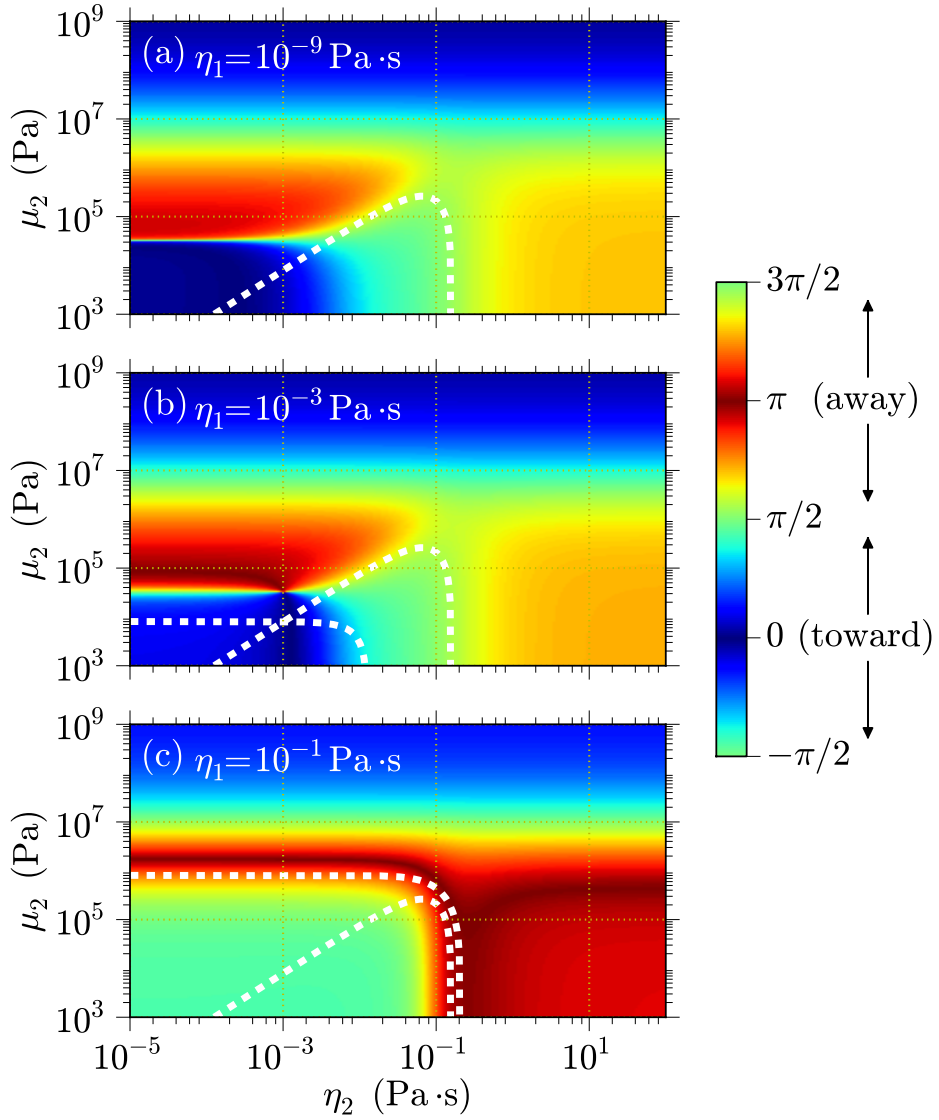

Figure 5.15: The phase of $\widehat{g}_{\text{rev}}(\omega_0)$ for a bubble of radius 3 μm immersed in water with varying shear viscosity at distance $5R_0$ from a viscoelastic medium (Kelvin) with density $\rho_2 = 1012\,\text{kg/m}^3$ and compressional wave speed $c_2 = 1518\,\text{m/s}$ (material 1 of Table 5.1). Various shades of blue or red correspond to bubble translation toward or away from the interface, respectively.

the liquid increases. This effect is not observed in Fig. 5.8, the corresponding figure employing the Voigt model.

By using the Kelvin model, the possibility exists to assign either low or high values for η_2 to induce bubble translation away from the interface; however, if we employ the Voigt model, then regions of phase which correspond to bubble translation away from the interface only exist for lower values for η_2. In addition, the general dynamical features of tissue are more accurate with the Kelvin model—specifically, that shear viscosity decreases, and shear modulus increases, as frequency increases. Because of these features, the Kelvin model seems more complete than the Voigt model.

5.3.2 The Maxwell model

The last model presented is the Maxwell model. It is, in essence, akin to the Kelvin model, but without the stiffness that acts independent of the damping. Figure 5.16 shows the mechanical systems representation of the Maxwell model. Thus, the frequency-domain equation describing the dynamics of tissue using the Maxwell model is

$$\begin{aligned}\widehat{f} &= -\frac{i\omega\eta_m}{1-i\omega\tau}\widehat{u} \\ &= \left(\mu_{m,M}\frac{(\omega\tau)^2}{1+(\omega\tau)^2} - i\mu_{m,M}\frac{(\omega\tau)}{1+(\omega\tau)^2}\right)\widehat{u}\,. \end{aligned} \tag{5.7}$$

We employ the Maxwell model in the dynamics of the tissue model presented in Section 2.3 by letting

$$\tilde{\mu}_2 = \left(\mu_{2,M} \frac{(\omega\tau)^2}{1+(\omega\tau)^2} - i\mu_{2,M} \frac{(\omega\tau)}{1+(\omega\tau)^2} \right) \widehat{u}\,, \tag{5.8}$$

where $\tau = \eta_2/\mu_{2,M}$. Because the Maxwell model does not contain the stiffness parameter μ_2, a direct comparison in terms of the previously presented plots of the phase of $\widehat{g}_{\text{rev}}(\omega_0)$ (i.e., Figs. 5.5–5.8 and 5.11–5.15) is not possible. However, the Kelvin model converges to the Maxwell model as $\mu_2 \to 0$ in Eq. (5.6). Hence, the results for the phase of $\widehat{g}_{\text{rev}}(\omega_0)$ for the Maxwell model are approximately those over the range of η_2 when $\mu_2 = 10^3$ Pa in Figs. 5.11–5.15. While $\mu_2 = 0$ is not included in these plots for the Kelvin model, the shear modulus 10^3 Pa is likely low enough. Therefore, the Maxwell model indicates that η_2 must be greater than approximately 10^{-1} Pa·s for the phase of $\widehat{g}_{\text{rev}}(\omega_0)$ to correspond with bubble translation away from the interface. Consequently, the Maxwell model misses the left-hand region (i.e., approximately when $\eta_2 < 10^{-2}$ Pa·s and 10^4 Pa$< \mu_2 < 10^6$ Pa) corresponding to bubble translation away from the interface seen in the Voigt and Kelvin models.

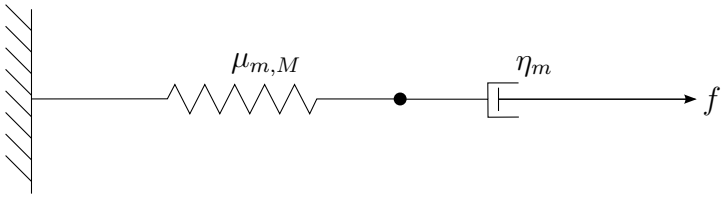

Figure 5.16: Mechanical system representation of the Maxwell model.

5.4 External and Reverberant Fields

Because none of the time-domain simulations in this chapter has taken into account an incident field, one may reasonably wonder how the translational force of the incident wave on the bubble compares with that due to the interface. While a rigorous comparison of these two fields involves further numerical simulations, a qualitative analysis is considered here. If an incident plane wave traveling parallel to the interface (in the $+x$ direction) is assumed, the magnitude of the corresponding external pressure gradient is

$$\left|\frac{\partial \widehat{p}_e}{\partial x}\right| = k_0 |\widehat{p}_e| \,, \tag{5.9}$$

where $k_0 = \omega_0/c_1$. The magnitude of the reverberant pressure gradient is expressed as

$$\left|\frac{\partial \widehat{p}_{\text{rev}}}{\partial z}\right| \approx \left(\kappa^2 - k_0^2\right)^{1/2} |\widehat{p}_{\text{rev}}| \,, \tag{5.10}$$

where κ represents the horizontal wavenumber near the maximum in the angular spectrum, where the field is evanescent and thus $\kappa > k_0$. Unlike the pressure gradient produced by the external field, the reverberant pressure gradient is not comprised of a single plane wave at a single frequency. An example of the spectrum associated with the reverberant pressure gradient is shown in Fig. 3.3. In this figure, the maximum value of the magnitude of the spectrum occurs where κ/k_0 is between approximately 30 and 50, where the value largely depends on the distance from the interface. The reverberant pressure gradient is thus one to two orders of magnitude greater than the external pressure gradient. The ratio of the external pressure gradient to the reverberant pressure

gradient may thus be expressed as

$$\left|\frac{\partial\widehat{p}_{\rm rev}/\partial z}{\partial\widehat{p}_e/\partial x}\right| \gg \left|\frac{\widehat{p}_{\rm rev}}{\widehat{p}_e}\right| = \frac{|\widehat{p}_{\rm rev}/\widehat{p}_{\rm im}|}{|\widehat{p}_e/\widehat{p}_{\rm im}|}\,, \tag{5.11}$$

where we have normalized by the pressure due to an image source since the reverberant pressure is frequently evaluated in terms of this ratio.

Because the bubble is always considered to be very close to the interface, the time for acoustic propagation between the bubble and its image is negligible, and the pressure from the image (due to a rigid interface) is approximately the same as the pressure generated at the bubble wall. The pressure produced by an externally driven bubble is obtained from the linear equation for a spherical bubble in an unbounded viscous medium,

$$\ddot{\xi} + \frac{\omega_0}{\rm QF}\dot{\xi} + \omega_0^2\xi = -\frac{p_e}{\rho_1 R_0}\,, \tag{5.12}$$

where $\xi(t)$ is the bubble wall displacement and QF is the quality factor of the resonance behavior of the bubble. If we assume $p_e = \widehat{p}_e e^{-i\omega t}$, then $\xi = \Xi(\omega)e^{-i\omega t}$, and Eq. (5.12) yields

$$\Xi(\omega) = -\frac{\widehat{p}_e}{\rho_1 R_0\omega_0^2}\left(1 - \omega^2/\omega_0^2 - i\frac{\omega/\omega_0}{\rm QF}\right)^{-1}\,. \tag{5.13}$$

With the particle displacement in hand, and with the volume velocity given by $Q(t) = 4\pi R_0^2\dot{\xi}(t)$, the pressure at the bubble wall due to the bubble image, a distance D from the actual bubble, is given by

$$p_{\rm im} = \rho_1\frac{\dot{Q}(t - D/c_1)}{4\pi D} \tag{5.14}$$

$$= \rho_1\frac{4\pi R_0^2\,\ddot{\xi}(t - D/c_1)}{4\pi D}\,, \tag{5.15}$$

where substitution of the solution for $\xi(t)$ yields

$$\widehat{p}_{\text{im}} = -\rho_1 \frac{R_0^2}{D} \omega^2 \Xi(\omega) e^{ikD} \,, \tag{5.16}$$

where $p_{\text{im}} = \widehat{p}_{\text{im}} e^{-i\omega t}$. Substitution of Eq. (5.13) into the right-hand side of Eq. (5.16), and evaluating the resulting expression at $\omega = \omega_0$, gives

$$\widehat{p}_{\text{im}} = i\,\text{QF} \frac{R_0}{D} \widehat{p}_e e^{ikD} \,, \tag{5.17}$$

and Eq. (5.17) may be rewritten as the ratio $|\widehat{p}_e/\widehat{p}_{\text{im}}|$, yielding

$$\left| \frac{\widehat{p}_e}{\widehat{p}_{\text{im}}} \right| = \frac{D}{R_0} \cdot \frac{1}{\text{QF}} \,. \tag{5.18}$$

For a bubble of only a few microns the quality factor is $O(10)$. Thus, the value of $|\widehat{p}_e/\widehat{p}_{\text{im}}|$ is $O(1)$ or less for $D/R_0 \leq 10$.

The ratio $\widehat{p}_{\text{rev}}/\widehat{p}_{\text{im}}$ in Eq. (5.11) may be written equivalently as $\widehat{g}_{\text{rev}}/\widehat{g}_{\text{im}}$. It is convenient to express Eq. (5.11) in terms of this ratio of Green's functions since $|\widehat{g}_{\text{rev}}/\widehat{g}_{\text{im}}|$ is plotted in several places in this dissertation (e.g., Figs. 2.3, 5.1, or 6.2). Hence, if $|\widehat{p}_e/\widehat{p}_{\text{im}}| \leq 1$ is assumed, then the ratio of the reverberant pressure gradient to the external pressure gradient is, when normalized by $|\widehat{g}_{\text{rev}}/\widehat{g}_{\text{im}}|$,

$$\frac{|\partial \widehat{p}_{\text{rev}}/\partial z| \,/\, |\partial \widehat{p}_e/\partial x|}{|\widehat{g}_{\text{rev}}/\widehat{g}_{\text{im}}|} = O(10) \,. \tag{5.19}$$

Note that in Figs. 2.3, 5.1, or 6.2, even for an interface between water and soft tissue, $|\widehat{g}_{\text{rev}}/\widehat{g}_{\text{im}}|$ is $O(10^{-2})$ or greater near the natural frequency of the bubble. Thus, we conclude that the reverberant pressure gradient is likely

of the same order as the pressure gradient produced by an external source. In addition, experiments do show that the reverberant fields dictate a large portion of the overall bubble dynamics.[3]

5.5 Conclusions

This chapter outlined the basic motivation necessary for exploring bubble translation without explicitly performing time-domain simulations. This was accomplished by correlating the phase of $\widehat{g}_{\text{rev}}(\omega)$ at the natural frequency of the bubble with the direction of bubble translation. We showed that when the phase of $\widehat{g}_{\text{rev}}(\omega_0)$ for an interface between water and a tissue-like solid was similar to that for a water-steel interface, bubble translation was directed toward the tissue-like solid. On the other hand, when the phase of $\widehat{g}_{\text{rev}}(\omega_0)$ for an interface between water and a tissue-like solid was similar to that for a water-air interface, bubble translation was directed away from the interface.

The phase of $\widehat{g}_{\text{rev}}(\omega_0)$ was then explored using both the Voigt and Kelvin models for various viscoelastic media. The red regions of the several two-dimensional plots of the phase of $\widehat{g}_{\text{rev}}(\omega_0)$ illustrate which combinations of material parameters correspond to bubble translation away from the interface. These regions generally occur where the real part of the complex shear modulus for the viscoelastic medium was greater than the magnitude of the imaginary part of the complex shear modulus for either the fluid or the viscoelastic medium, $\text{Re}\{\tilde{\mu}_2\} > |\text{Im}\{\tilde{\mu}_2\}|$, $|\text{Im}\{\tilde{\mu}_1\}|$. The only exception to this condition in over 18,000 different combinations of bubble/material parame-

ters tested was either when the bubble was very close to the interface (i.e., $z_0 < 2.5R_0$), or when fluid shear viscosity was high (i.e., $\eta_1 > 10^{-2}$ Pa·s). Under these circumstances, combinations of μ_2 and η_2 corresponding to bubble translation away from the interface occurred for $\eta_2 \approx \eta_1$ and $\mu_2 < \omega_0\eta_1$ [e.g., see Fig. 5.6(a), 5.8(c), or 5.15(c)] Changes in the phase of $\widehat{g}_{\text{rev}}(\omega_0)$ were illustrated with several figures by varying material properties of the viscoelastic medium, the distance of the bubble from the interface, or the shear viscosity in the fluid. The Kelvin model was very similar to the Voigt model for $\eta_2 < 10^{-2}$ Pa·s; however, the Kelvin model displayed additional regions correlating bubble translation away from the interface which were not displayed in the corresponding figures for the Voigt model. The Kelvin model was shown to be a more appropriate model for a tissue-like solid since the effective shear viscosity value decreases, and the effective shear modulus increases, as frequency increases.

While experiments have shown that shear modulus and standoff distance from the interface are two main constituents in predicting direction of bubble translation, we showed that the shear viscosity in both the fluid and the tissue-like medium are equally important parameters. In fact, almost all the material parameters for the viscoelastic medium play significant roles in affecting bubble translation. Evaluating the phase of $\widehat{g}_{\text{rev}}(\omega_0)$, instead of running a time-domain simulation, helped to quickly determine which combinations of material parameters result in bubble translation in a particular direction.

Variations in these results may be considerable once other external

variables are included in the model. For instance, the pressure changes are assumed here to be nearly adiabatic; however, heat exchange is a relevant effect involved when the bubbles are laser-generated,[1] or undergo violent collapse. We also note that while we were able to focus on mild bubble pulsation dominated by one oscillation frequency, a more violent collapse will involve many additional frequencies. Regardless, these results are consistent mathematically with the results obtained by others,[46] in that the phase of the field produced by some external object (i.e., the fluid-solid interface) relative to the pulsation of the bubble will dictate overall direction of translation.

Chapter 6

High-Amplitude Bubble Dynamics Simulations

The previous chapter showed that the direction of bubble translation for a linearly pulsating bubble near a fluid-solid interface depends on the phase of $\widehat{g}_{\text{rev}}(\omega_0)$, which is the frequency spectrum of the portion of the Green's function corresponding to the reverberant pressure gradient evaluated at the natural frequency of the bubble, ω_0. However, the question regarding the direction of bubble translation as bubble pulsation becomes nonlinear still remains. Hence, in this chapter we explore the direction of bubble translation for high-amplitude bubble pulsation near an interface between water and a tissue-like viscoelastic medium.

Before performing simulations involving high-amplitude bubble simulations, we must reevaluate the equations of motion for bubble pulsation and translation. Specifically, we are interested to know if the term that was originally neglected from the bubble translation equation [the last term within the parentheses on the right-hand side of Eq. (2.2)] is now important for these highly nonlinear dynamics. We also analyze a more accurate equation for bubble pulsation. We then study the direction of bubble translation for a

freely oscillating bubble near a liquid-solid interface, with the bubble initially compressed in size. We analyze this scenario for various levels of compression, standoff distances from the interface, and shear moduli of the viscoelastic medium.

6.1 Reevaluating the Bubble Dynamics Equations

The equations for bubble pulsation and translation introduced in Chapter 2 [Eqs. (2.1) and (2.2)] are repeated here for convenience:

$$R\ddot{R} + \frac{3}{2}\dot{R}^2 = \frac{P_{\text{liq}} - P_0}{\rho_1} - \left(\frac{p_e + p_{\text{rev}}}{\rho_1} - \frac{1}{4}\left|\dot{\mathbf{X}} - (\dot{\mathbf{u}}_e + \dot{\mathbf{u}}_{\text{rev}})\right|^2\right), \quad (6.1)$$

$$\frac{d}{dt}\left\{R^3\left[\dot{\mathbf{X}} - (\dot{\mathbf{u}}_e + \dot{\mathbf{u}}_{\text{rev}})\right]\right\} = -2R^3\boldsymbol{\nabla}\left(\frac{p_e + p_{\text{rev}}}{\rho_1} - \frac{1}{4}\left|\dot{\mathbf{X}} - (\dot{\mathbf{u}}_e + \dot{\mathbf{u}}_{\text{rev}})\right|^2\right) + \frac{3\mathbf{F}_d}{2\pi\rho_1}, \quad (6.2)$$

Equation (6.1) was unmodified in the preceding chapters, but the higher-order term $\frac{1}{4}\boldsymbol{\nabla}\left|\dot{\mathbf{X}} - (\dot{\mathbf{u}}_e + \dot{\mathbf{u}}_{\text{rev}})\right|^2$ in Eq. (6.2) was previously ignored. Even without this neglected term, we may describe nonlinear pulsation and translation of a spherical bubble using Eqs. (6.1) and (6.2); however, by doing so we must quantify the loss in accuracy. In previous chapters, this analysis was unimportant since we considered only mild bubble pulsation. Thus, in this chapter we determine the relevance of each of the terms in Eqs. (2.1) and (2.2) when the bubble dynamics are highly nonlinear.

6.1.1 High-amplitude bubble pulsation

Equation (6.1) can be modified to account for bubble pulsation to order $O(1/c_1)$:[52]

$$\left(1-\frac{\dot{R}}{c_1}\right)R\ddot{R}+\frac{3}{2}\left(1-\frac{\dot{R}}{3c_1}\right)\dot{R}^2 = \frac{1}{\rho_1}\left(1+\frac{\dot{R}}{c_1}+\frac{R}{c_1}\frac{d}{dt}\right)\left(P_{\text{liq}}-P_0-p_e-p_{\text{rev}}\right)\,, \tag{6.3}$$

which is equivalent to Keller's equation to the same order.[23] The derivation of Eq. (6.3) accounts for liquid compressibility, and is explained in detail by Ilinskii et al.[26] While including terms of higher accuracy can be important when pulsation includes bubble collapse, incorporating the extra terms introduced in Eq. (6.3) requires us to calculate a derivative of the reverberant pressure with respect to time. By using the Green's function presented in this dissertation to calculate the reverberant pressure, the time derivative of the reverberant pressure exacerbates the numerical instabilities introduced using our numerical approach (e.g., see Fig. 3.7). Therefore, Eq. (6.3) is much less stable for the problem at hand. For this reason we choose to leave Eq. (6.1) unmodified. This simplifies the computational burden for the radial dynamics, allowing us to focus on the translational dynamics.

6.1.2 High-amplitude bubble translation

In Chapter 2 we reasoned that the higher-order term in Eq. (6.2) (the last term within the parentheses on the right-hand side) could be ignored on

the grounds that we consider only moderately low-amplitude bubble pulsation. Thus, before simulating highly nonlinear bubble translation we must reevaluate the importance of this term. By solving Eq. (6.2) for bubble acceleration, we put it in the form used computationally (before nondimensionalization). After expanding the left-hand side of Eq. (6.2), dividing by R^3, and solving for $\ddot{\mathbf{X}}$, we obtain

$$\ddot{\mathbf{X}} = -3\frac{\dot{R}}{R}\left[\dot{\mathbf{X}} - (\dot{\mathbf{u}}_e + \dot{\mathbf{u}}_{\text{rev}})\right] - \frac{3}{\rho_1}\boldsymbol{\nabla}(p_e + p_{\text{rev}}) + \frac{1}{2}\boldsymbol{\nabla}\left|\dot{\mathbf{X}} - (\dot{\mathbf{u}}_e + \dot{\mathbf{u}}_{\text{rev}})\right|^2 + \frac{3\mathbf{F}_d}{2\pi\rho_1 R^3}\,. \tag{6.4}$$

The magnitude of each term on the right-hand side of Eq. (6.4), at each instant in time, gives us an estimate of the relevance of each term in calculating the overall bubble translation. In other words, at a specific instance in time the magnitude of each term on the right-hand side of Eq. (6.4) indicates which terms are most important. Terms several orders of magnitude lower than other terms are unimportant in the overall computation of the bubble acceleration at that instant in time. Therefore, we gauge the importance of including the third term on the right-hand side of Eq. (6.4) when simulating nonlinear bubble translation by comparing its magnitude to the corresponding magnitudes of the first and second terms at each instant in time.

Figure 6.1 shows the (a) pulsation and (b) translation of a bubble of radius $3\,\mu$m at distance $7.5R_0$ from an interface between water and a viscoelastic medium with density $\rho_2 = 1012\,\text{kg/m}^3$, compressional wave speed $c_2 = 1518\,\text{m/s}$, shear modulus $\mu_2 = 10^7\,\text{Pa}$, shear viscosity $\eta_2 = 2\times10^{-3}\,\text{Pa·s}$,

and zero bulk viscosity. We define the dynamics of all the viscoelastic media in this chapter with the Kelvin model [Eq. (5.4)]; for this simulation, the parameter $\mu_{2,M} = 10^5\,\text{Pa}$. The simulation begins with the bubble initially compressed to a radius of $R(0) = 0.2R_0$. Once released, the bubble radius grows to a few times the size of the equilibrium radius and then quickly collapses. Figure 6.1(c) compares the magnitudes of the first, second, and third terms on the right-hand side of Eq. (6.4) for the duration of the simulation. We note that the magnitudes of the first and second terms (the black and red lines, respectively) are of the same order, and are both the predominant term at various stages of the simulation. For example, the term involving the reverberant pressure (term 2) is largest when the bubble radius is large ($0.25 \leq t/T_0 \leq 1.25$), whereas the first term dominates during bubble collapse ($t/T_0 \geq 1.25$). Note that the magnitude of the third term is several orders of magnitude lower than the other two terms for all time. This disparity, to varying degrees, was observed in all other simulations which were checked, which included different types of interfaces, driven versus free bubble oscillation, as well as various distances from the interfaces and amounts of initial compression. The third term is more important at closer distances to the interface and for higher degrees of nonlinearity, but was never found to be significant when compared to the first and second terms. On average, the third term was about six orders of magnitude smaller than the most significant term at any point in time of the simulation. Thus, to the degree of nonlinearity observed in Fig. 6.1, the third term on the right-hand side of Eq. (6.4) may still be

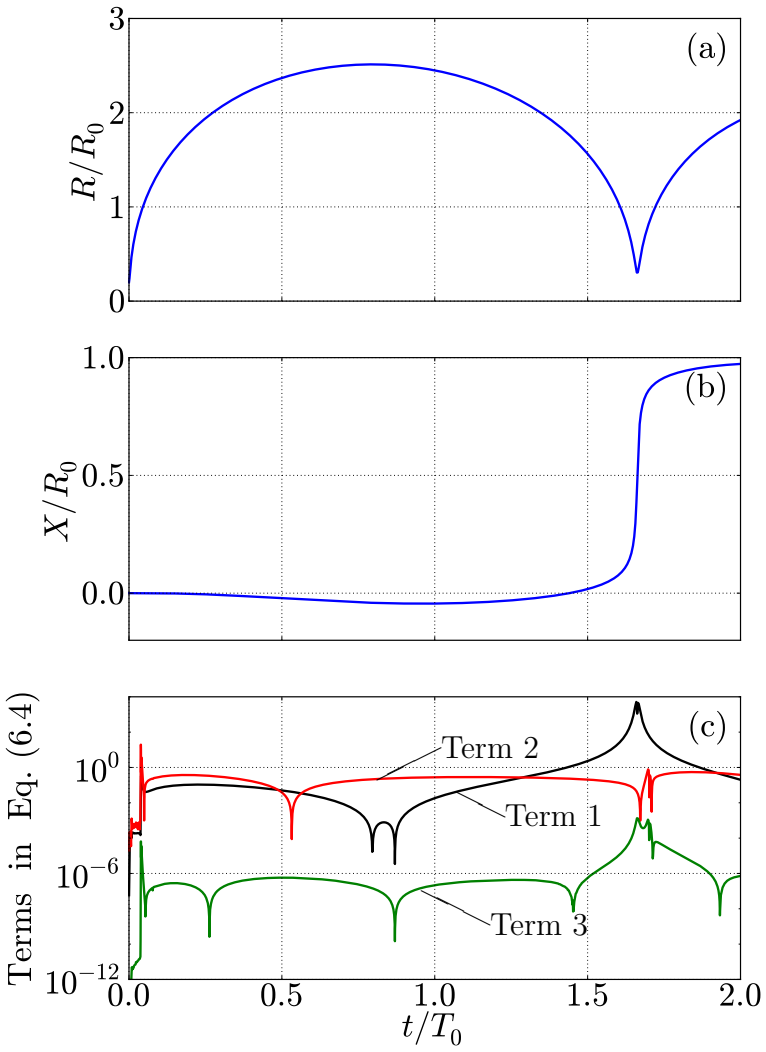

Figure 6.1: Simulation of the (a) pulsation and (b) translation of a bubble of radius $3\,\mu$m, initially compressed to $0.2R_0$, at distance $7.5R_0$ from an interface between water and a viscoelastic medium with density $\rho_2 = 1012\,\mathrm{kg/m^3}$, compressional wave speed $c_2 = 1518\,\mathrm{m/s}$, shear modulus $\mu_2 = 10^7\,\mathrm{Pa}$, shear viscosity $\eta_2 = 2 \times 10^{-3}\,\mathrm{Pa{\cdot}s}$, zero bulk viscosity, and $\mu_{2,M} = 10^5\,\mathrm{Pa}$. Plot (c) shows the magnitudes of the first, second, and third terms on the right-hand side of Eq. (6.4).

dropped from the calculations, and the translation equation is left unmodified from its form used in previous chapters. Hence, with no modifications to the bubble dynamics equations used in the preceding chapters, we now analyze higher-amplitude simulations.

6.2 High-Amplitude Simulations

To better understand the role that the reverberant pressure gradient plays in determining direction of bubble translation, we slowly increase the amplitude of bubble oscillation (i.e., the amount of nonlinearity in the bubble pulsation) and compare this with the magnitude and phase of $\widehat{g}_{\text{rev}}(\omega)$. While the phase of $\widehat{g}_{\text{rev}}(\omega)$ at the natural oscillation frequency of the bubble indicates the direction of bubble translation during free oscillation, both the magnitude and phase of this frequency spectrum are important when we introduce multiple frequencies. We gradually introduce more frequency content into the bubble dynamics by initially compressing the bubble to a smaller and smaller initial radius. For low amounts of initial compression, the bubble will pulsate linearly, and the only frequencies of interest are those very close to the oscillation frequency of the bubble. However, as the bubble is compressed by larger amounts, the group of frequencies involved in the computation increases.

Figure 6.2 shows the (a) magnitude and (b) phase of $\widehat{g}_{\text{rev}}(\omega)$ calculated at distance $7.5\,\mu$m ($2.5R_0$ for $R_0 = 3\,\mu$m) from an interface between water and a tissue-like viscoelastic medium. The shear modulus of the viscoelastic medium is varied from $\mu_2 = 10^4\,$Pa to $10^7\,$Pa, while density $\rho_2 = 1012\,\text{kg/m}^3$,

compressional wave speed $c_2 = 1518\,\mathrm{m/s}$, shear viscosity $\eta_2 = 2 \times 10^{-3}\,\mathrm{Pa{\cdot}s}$, bulk viscosity is zero, and $\mu_{2,M} = 10^5\,\mathrm{Pa}$. The range in shear moduli may seem somewhat high when compared to conventional values used for soft tissue, but we reemphasize that this parameter is highly frequency dependent,[78,79] and can be much larger at higher frequencies.[77,82] The frequency spectra produced for $\widehat{g}_{\mathrm{rev}}(\omega)$ are normalized with the corresponding spectra for an image source, given in Eq. (2.67) and repeated here for convenience:

$$\widehat{g}_{\mathrm{im}} = \left(i\frac{\omega}{c_1} - \frac{1}{D} \right) \frac{e^{i\omega D/c_1}}{4\pi D}\,, \tag{6.5}$$

where $D = z_0 - z$ and we evaluate the field at the location of the bubble, $z = -z_0$. We remind the reader that the frequency spectra are evaluated at very high frequencies so that the very small distance between the interface and the bubble center is resolved during time-domain simulations.

The pink vertical bands in Fig. 6.2 indicate the approximate oscillation frequency of a bubble of radius $3\,\mu\mathrm{m}$. We note that near this frequency the phase for each spectrum shown in Fig. 6.2(b) exhibits various qualities to help show the contribution of multiple frequencies during high-amplitude bubble dynamics simulations. For example, the lines corresponding to $\mu_2 = 10^5\,\mathrm{Pa}$ and $10^7\,\mathrm{Pa}$ have roughly constant phase ranging from $0.8\,\mathrm{MHz}$ to $2\,\mathrm{MHz}$ (which covers the natural frequency of the bubble), with values similar to those produced by a water-air or water-steel interface, respectively. The line for $\mu_2 = 10^4\,\mathrm{Pa}$ has a phase which decreases with increasing frequency, and is at a phase near $\pi/2$ at the resonance frequency of the bubble. This is significant since a phase

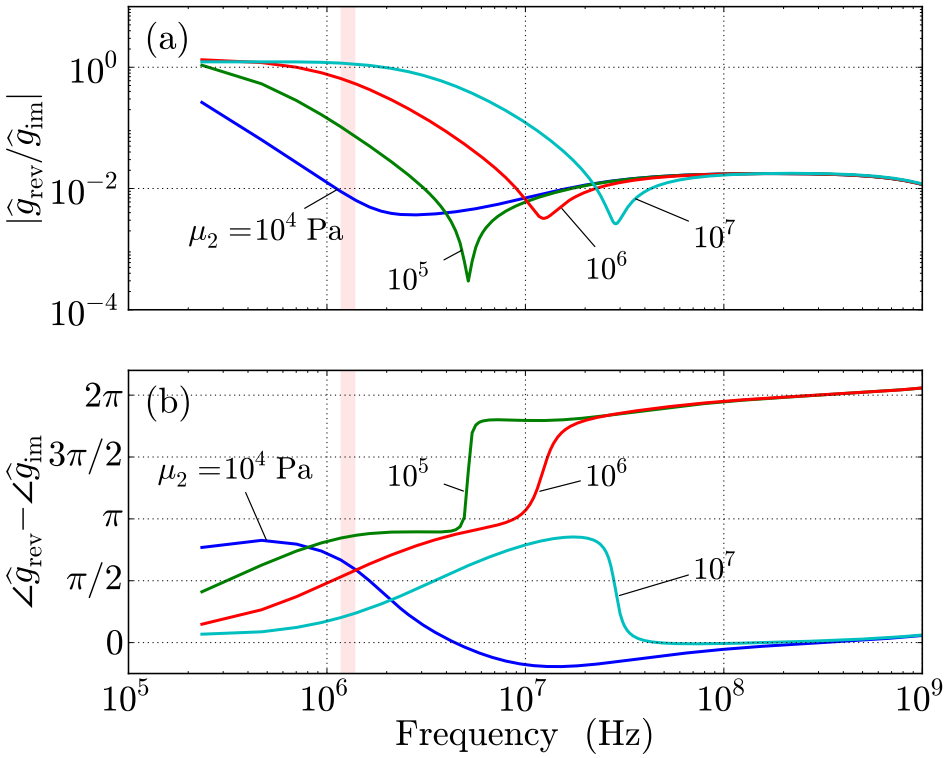

Figure 6.2: The (a) magnitude and (b) phase of $\widehat{g}_{\rm rev}(\omega)$, normalized by the corresponding image source [Eq. (6.5)], a distance 7.5 μm from the interface. The fluid is water and the viscoelastic medium is tissue-like. The shear modulus of the tissue μ_2 ranges from 10^4 Pa to 10^7 Pa, with density $\rho_2 = 1012\,\mathrm{kg/m^3}$, compressional wave speed $c_2 = 1518\,\mathrm{m/s}$, shear viscosity $\eta_2 = 2 \times 10^{-3}\,\mathrm{Pa{\cdot}s}$, and bulk viscosity is zero. The Kelvin model is used to define the dynamics of the tissue [Eq. (5.4)], where $\mu_{2,M} = 10^5$ Pa.

of $\pi/2$ lies exactly in between the phases for a water-air interface (a phase of π radians) and water-steel interface (a phase of 0 radians). Thus, for the line where $\mu_2 = 10^4$ Pa the phase of $\widehat{g}_{\rm rev}(\omega)$ at frequencies lower than those shaded in pink is more similar to that for a water-air interface, while the phase is more similar to a water-steel interface for frequencies greater than the region

of frequencies shaded in pink. The line for $\mu_2 = 10^6\,\mathrm{Pa}$ slopes the opposite direction of the line for $\mu_2 = 10^4\,\mathrm{Pa}$, where the phase of $\widehat{g}_{\mathrm{rev}}(\omega)$ for the line for $\mu_2 = 10^6\,\mathrm{Pa}$ is more like a water-steel interface at lower frequencies and approaches the phase for a water-air interface at high frequencies (less than $10^7\,\mathrm{Hz}$). How important $\widehat{g}_{\mathrm{rev}}(\omega)$ is at a particular frequency, in terms of determining the overall translation of the bubble, depends on the corresponding magnitude of $\widehat{g}_{\mathrm{rev}}(\omega)$, shown in Fig. 6.2(a).

Another factor to consider when evaluating $\widehat{g}_{\mathrm{rev}}(\omega)$ is the spectrum of the volume velocity of the bubble, the function with which g_{rev} is convolved to produce the reverberant pressure gradient. For a stationary bubble, the spectrum of the reverberant pressure gradient can be expressed as

$$\frac{\partial \widehat{p}_{\mathrm{rev}}}{\partial z} = i\omega\rho\widehat{g}_{\mathrm{rev}}(\omega)\widehat{Q}\,, \tag{6.6}$$

where, for low-amplitude pulsation, $\widehat{Q}$ is essentially a delta function in frequency at ω_0. Thus, restricting the analysis of the reverberant pressure gradient to low-amplitude pulsation, as in Chapter 5, allows us to analyze $\widehat{g}_{\mathrm{rev}}$ at only ω_0. However, as bubble is more nonlinear, $\widehat{Q}$ is no longer similar to a delta function and the product $\widehat{g}_{\mathrm{rev}}\widehat{Q}$ must be analyzed instead. Figure 6.3 shows the (a) pulsation of a stationary bubble of $3\,\mu\mathrm{m}$ immersed in water and in free space. The bubble is compressed initially by varying amounts such that the initial bubble radius ranges from $R(0) = 0.9R_0$ to $0.2R_0$. The time domain simulations are computed for $100T_0$, from which the spectrum of the volume velocity $\widehat{Q}(\omega)$ is calculated. The normalized magnitude of $\widehat{Q}(\omega)$ corresponding to each simulation in Fig. 6.3(a) is shown in Fig. 6.3(b). As the bubble

begins at a smaller initial radius, we note the presence of higher harmonics at frequencies above the natural frequency of the bubble. In addition, the peak amplitude of $|\widehat{Q}(\omega)|$ shifts to a lower frequency. While $\widehat{Q}(\omega)$ is determined for a stationary bubble in a free field, it gives us a qualitative feel for which regions of the phase of $\widehat{g}_{\text{rev}}(\omega)$ correspond to a large amplitude of $|\widehat{g}_{\text{rev}}\widehat{Q}|$. In other words, predicting direction of bubble translation when bubble pulsation is highly nonlinear likely requires us to evaluate the phase of $\widehat{g}_{\text{rev}}(\omega)$ at frequencies lower than the natural frequency of the bubble. We also stress that while we have neglected radiation damping in the simulation with a significant degree of nonlinearity, the spectra produced here are qualitatively the same when this effect is included. Regardless, changing the spectrum of $\widehat{Q}$ with more accurate models of the bubble pulsation does not change the outlined logic.

An example of how one would use the phase of $\widehat{g}_{\text{rev}}(\omega)$, along with the magnitude of $\widehat{g}_{\text{rev}}\widehat{Q}$, to predict the direction of bubble translation is illustrated by considering a bubble near a viscoelastic medium and under various amounts of compression. Figure 6.4 shows four different simulations of $R(t)$ and $X(t)$ for a bubble of radius $3\,\mu$m immersed in water and at distance $2.5R_0$ from each of the viscoelastic media defined in Fig. 6.2. Bubble pulsation is illustrated on the left [Figs. 6.4(a)–6.4(d)], and bubble translation on the right [Figs. 6.4(e)–6.4(h)]. Bubble translation toward the interface is represented when $X > 0$, while $X < 0$ is when the bubble translates away from the interface. The bubble oscillates freely near the liquid-solid interface, and is

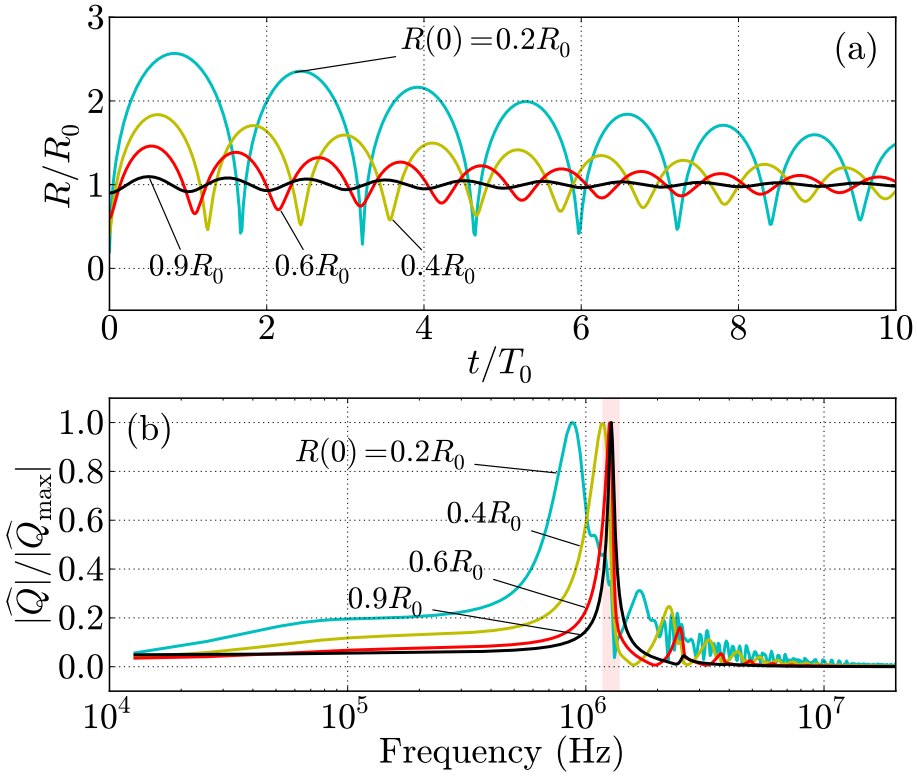

Figure 6.3: Temporal (a) pulsation of a bubble of radius 3 μm in free space and initially compressed such that the initial bubble radius ranges from $R(0) = 0.2R_0$ to $0.9R_0$. The normalized magnitude of the spectrum of the volume velocity $\widehat{Q}(\omega)$ is shown for each time-domain simulation in plot (b).

compressed initially by various amounts, as indicated in the column on the right. Like all the analysis in Chapter 5, mild compression (e.g., an initial bubble radius of $0.9R_0$) induces linear bubble pulsation, from which bubble translation can be inferred by evaluating only the phase of $\widehat{g}_{\text{rev}}(\omega_0)$. Thus, the direction of bubble translation for $\mu_2 = 10^4$ Pa to 10^7 Pa illustrated in Fig. 6.4(a) is predicted by evaluating the phase of the corresponding spectrum displayed in Fig. 6.2(b) at the oscillation frequency of the bubble (the region

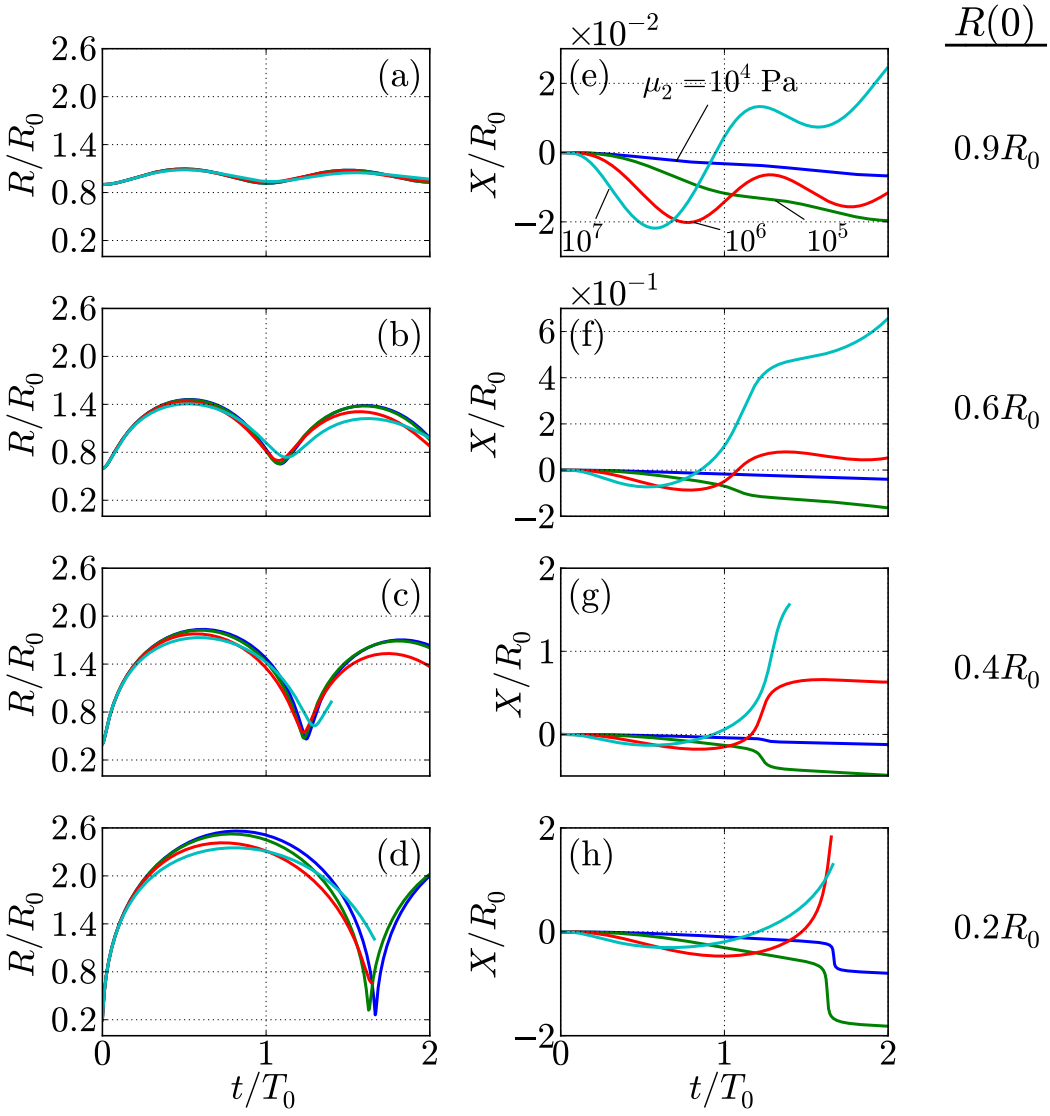

Figure 6.4: Pulsation (left) and translation (right) of an initially compressed bubble of radius $3\,\mu$m in free oscillation a distance $2.5R_0$ from an interface between water and a viscoelastic medium. The viscoelastic medium is assigned density $\rho_2 = 1012\,\mathrm{kg/m^3}$, compressional wave speed $c_2 = 1518\,\mathrm{m/s}$, shear viscosity $\eta_2 = 2 \times 10^{-3}\,\mathrm{Pa{\cdot}s}$, modulus $\mu_{2,M} = 10^5\,\mathrm{Pa}$ corresponding to the Kelvin model [Eq. (5.4)], and zero bulk viscosity.

shaded in pink). However, by increasing the amount of initial compression of the bubble, Fig. 6.3(b) shows that the spectrum of $\widehat{Q}$ is much broader, where the majority of the energy in the spectrum is lower in frequency than ω_0.

An notable feature of the line corresponding to $\mu_2 = 10^6$ Pa in Fig. 6.4 is the apparent change in direction of bubble translation as the amount of initial compression is increased. More specifically, we note that the direction of translation for line corresponding to $\mu_2 = 10^6$ Pa in Fig. 6.4(a) is directed away from the interface; however, for smaller initial bubble radii [Figs. 6.4(b)–6.4(d)], the direction of bubble translation is toward the interface.[†] This change in direction is understood by analyzing the phase of $\widehat{g}_{\text{rev}}(\omega)$ for $\mu_2 = 10^6$ Pa in Fig. 6.2, along with the various spectra shown in Fig. 6.3(b). For $R(0) = 0.9R_0$ in Fig. 6.3(b), the spectrum of the volume velocity is a narrow spike near the natural frequency of the bubble, and we anticipate that the phase of $\widehat{g}_{\text{rev}}(\omega)$ is only important at ω_0. However, for $R(0) < 0.9R_0$ the frequency corresponding to the maximum magnitude of $\widehat{Q}$ occurs at frequencies less than ω_0. Below ω_0 (i.e., below the portion of the axes shaded in pink), the phase of $\widehat{g}_{\text{rev}}(\omega)$ for $\mu_2 = 10^6$ Pa in Fig. 6.2 approaches that for a water-steel interface, where the magnitude of $\widehat{g}_{\text{rev}}(\omega)$ is also higher. Thus, as the bubble is compressed more, these lower frequencies play a more important role in the response of this dynamical system, and can result in a change in the direction of bubble

[†]One may argue that translation appears to trend toward the interface later in the simulation ($t/T_0 > 0.8$); however, the final amount of gross translation (at $t/T_0 = 2$) is away from the interface. Other simulations shown later will illustrate this change in direction of bubble translation more convincingly.

translation.

The direction of bubble translation for several more simulations is presented in Fig. 6.5. Hence, the overall translation of the bubble is indicated qualitatively by a blue (up) or red (down) arrow, which indicates bubble translation toward (up) or away (down) from the interface, respectively. Simulations were performed for each of the four different viscoelastic media considered in Figs. 6.2 and 6.4; thus, the shear modulus for the viscoelastic medium is varied in the plots in Fig. 6.5, ranging from $\mu_2 = 10^4\,\text{Pa}$ to $10^7\,\text{Pa}$. The bubble is initially compressed such that the radius of the bubble at time $t = 0$ ranges from $R(0) = 0.2R_0$ to $0.9R_0$ in increments of $0.1R_0$, with $R_0 = 3\,\mu\text{m}$. A smaller initial bubble radius corresponds to a larger maximum radius in the overall simulation. The initial distance from the interface is also varied, ranging from $z_0 = 2.5R_0$ to $15R_0$ in increments of $2.5R_0$. The gray lines connecting groups of six arrows constitute an identical initial bubble radius over the various distances from the bubble to the interface. The vertical axis is shown in terms of the maximum radius of the bubble over the life of the simulation. For example, simulations where the bubble begins at a radius of $0.2R_0$ correspond to the arrows displayed near $R_{\text{max}}/R_0 = 2.5$.

Several comments regarding Fig. 6.5 are in order. First, for all shear moduli considered, the direction of bubble translation changes as the distance of the bubble from the interface changes; however, the initial and final directions of translation depend on which shear modulus is considered. For instance, when $\mu_2 = 10^4\,\text{Pa}$ [Fig. 6.5(a)], the direction of bubble translation

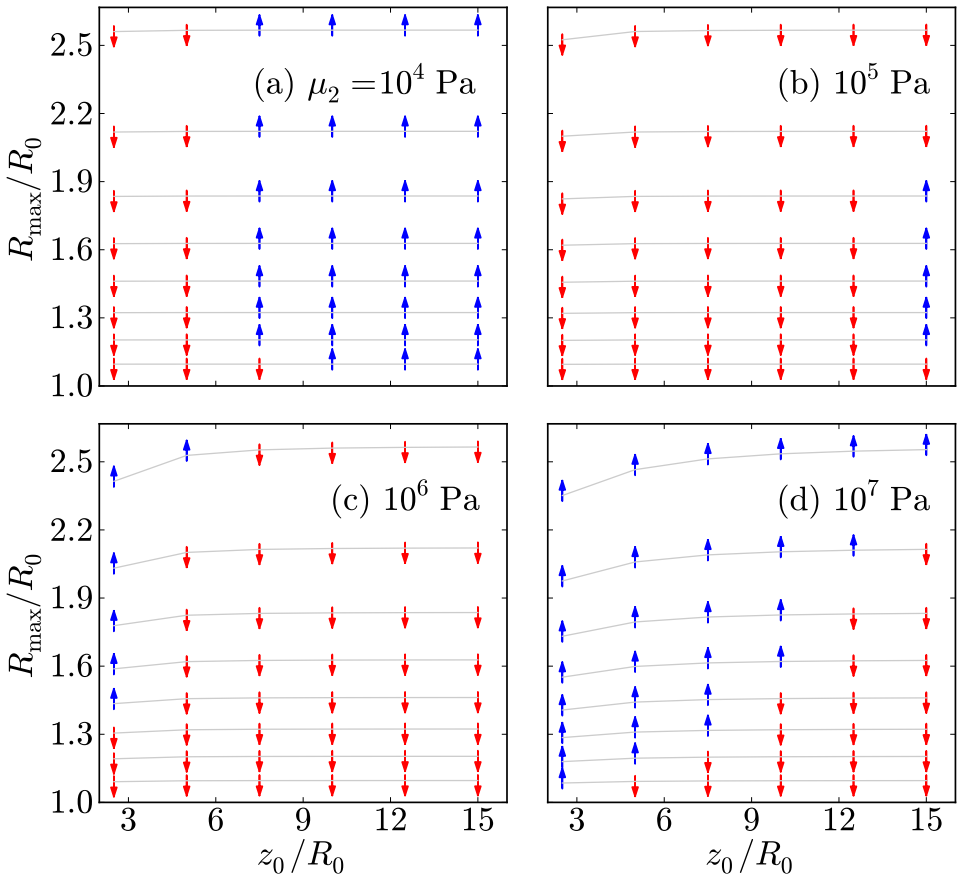

Figure 6.5: Direction of bubble translation for a bubble in free oscillation, compressed to an initial bubble radius ranging between $R(0) = 0.2R_0$ and $0.9R_0$ in increments of $0.1R_0$, where $R_0 = 3\,\mu$m. Smaller values of the initial bubble radius correspond to larger maximum radius values on the y axis. The distance z_0, which describes the distance from the interface to the bubble center, is also varied between $2.5R_0$ to $15R_0$ in increments of $2.5R_0$. The bubble is immersed in water, near a viscoelastic medium with density $\rho_2 = 1012\,\text{kg/m}^3$, compressional wave speed $c_2 = 1518\,\text{m/s}$, shear viscosity $\eta_2 = 2\times10^{-3}\,\text{Pa·s}$, zero bulk viscosity, and shear modulus ranging from $\mu_2 = 10^4\,\text{Pa}$ to $10^7\,\text{Pa}$ in (a) through (d). The Kelvin model is used to define the dynamics of the solid [Eq. (5.4)], where $\mu_{2,M} = 10^5\,\text{Pa}$. The gray lines connect the simulations with the same initial bubble radius.

is away from the interface when the bubble is nearer to it, and toward the interface when the bubble is farther away from it. On the other hand, when $\mu_2 = 10^7\,\text{Pa}$ [Fig. 6.5(d)], the direction of bubble translation is toward the interface when the bubble is nearer to it, and away from the interface when the bubble is farther away from it. This effect was previously highlighted in Figs. 5.6 and 5.13, where the region defining bubble translation away from the interface moves to higher values of shear modulus as the bubble moves away from the interface. Therefore, lower shear moduli transition out of the region corresponding to bubble translation away from the interface, while higher shear moduli transition into this region.

Second, the direction of bubble translation observed for $\mu_2 = 10^6\,\text{Pa}$ and $10^7\,\text{Pa}$ [in Figs. 6.5(c) and 6.5(d), respectively] is directed toward the interface at closer distances and away from the interface at farther distances. This feature of bubble translation was also observed experimentally by Brujan et al.[1] (their Figure 12), and is shown here in Fig. 6.6. The horizontal axis represents nondimensional distance (γ, which nominally spans a range of z_0/R_0 from 0 to approximately 12.5), while the vertical axis represents which direction, and to what degree, translation from the interface occurs. For values where $b_{R_{\min}}/s > 1$ in Fig. 6.6, Brujan et al.[1] observed bubble translation away from the interface, and for values where $b_{R_{\min}}/s < 1$, bubble translation toward the interface was observed. The horizontal purple dashed line in Fig. 6.6 separates where the change in direction of bubble translation occurs. The red and orange dotted lines correspond qualitatively to the change in di-

rection of bubble translation observed in Figs. 6.5(c) and 6.5(d), respectively. In addition, the trends seen for $\mu_2 = 10^5$ Pa [Fig. 6.5(b)] correspond to those overlaid by the green dotted line. Bubble translation is directed away from the interface for all the distances simulated for z_0/R_0 from 2.5 to 12.5. While the pattern of bubble translation shown for $\mu_2 = 10^4$ Pa [Fig. 6.5(a)] is not

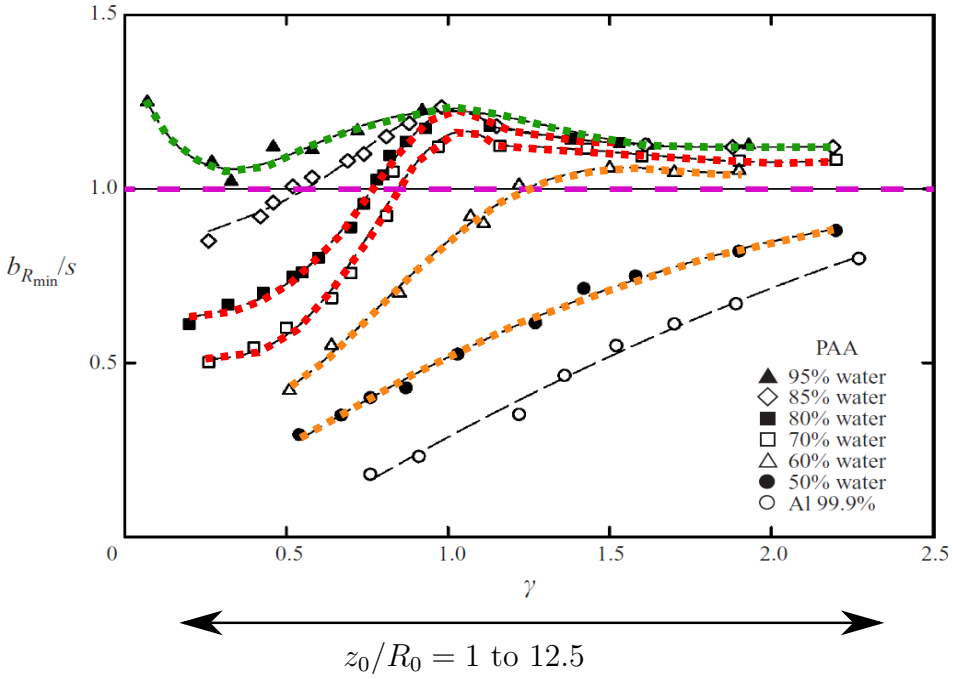

Figure 6.6: Taken from Figure 12 of Brujan et al.[1] This figure summarizes the relationship between distance from the interface and the direction of bubble translation. The colored dashed lines have been added here for emphasis. In the legend, the PAA samples (a type of tissue mimicking material) with higher water content correspond to softer tissue phantoms. Bubble translation toward the interface corresponds to values of the vertical axis which are less than unity (i.e., below the purple dashed line), whereas bubble translation away from the interface occurs for values of the vertical axis which are greater than unity.

observed in the data presented by Brujan et al.,[1] the high-amplitude pressure waves radiated from the laser-generated cavitation bubbles in their experiment likely increased the modulus of the sample to exceed this value.

There are other differences between these simulations and their experiment, making it difficult to perform a rigorous comparison with them. One notable difference is the maximum bubble radius, which was measured to be around a millimeter in the experiments performed by Brujan et al.,[1] whereas in the present work it is only a few microns. This difference in bubble radius alters the natural frequency of the bubble by many orders of magnitude, changing the distances of the bubble from the interface, since the distances here are measured in terms of equilibrium bubble radius.[†] The discrepancy in the natural frequency of the bubble may also indicate that their experiment involved substantial alterations of the reverberant pressure and its gradient since the tissue phantom was only 20 mm thick. Because we have assumed a viscoelastic half-space, this possibility is not accounted for in our model. In Chapter 2 it was shown that effects of the layer may be ignored for thicknesses larger than about $100R_0$. Thus, the samples used by Brujan et al.[1] likely create different reverberant spectra than those produced here. Regardless of the discrepancies between the two scenarios, the simulations in Figs. 6.5(b)–6.5(d)

[†]Matching the parameters set forth by Brujan et al.[1] has been attempted. However, a nominal equilibrium radius is not given in their paper since the bubbles were generated by a focused laser. In addition, a larger equilibrium bubble radius makes our numerical simulations more difficult since the number of frequencies needed to resolve portion of the spectrum near resonance, while still maintaining a maximum frequency near a gigahertz, is very large.

show qualitative agreement with the results published by Brujan et al.[1]

The third observation regarding Fig. 6.5 is a qualitative comparison with Chen et al.[3] They reported, for their experiments involving micron-sized bubbles within actual tissue vessels, that translation was always directed away from nearest vessel wall. Their results are summarized in their Fig. 6, and shown here in Fig. 6.7. The horizontal axis is a nondimensional distance which is comparable to a range of z_0/R_0 from 1 to 10. This result is largely portrayed for $\mu_2 = 10^5$ Pa in Fig. 6.5, where, for all standoff distances but the

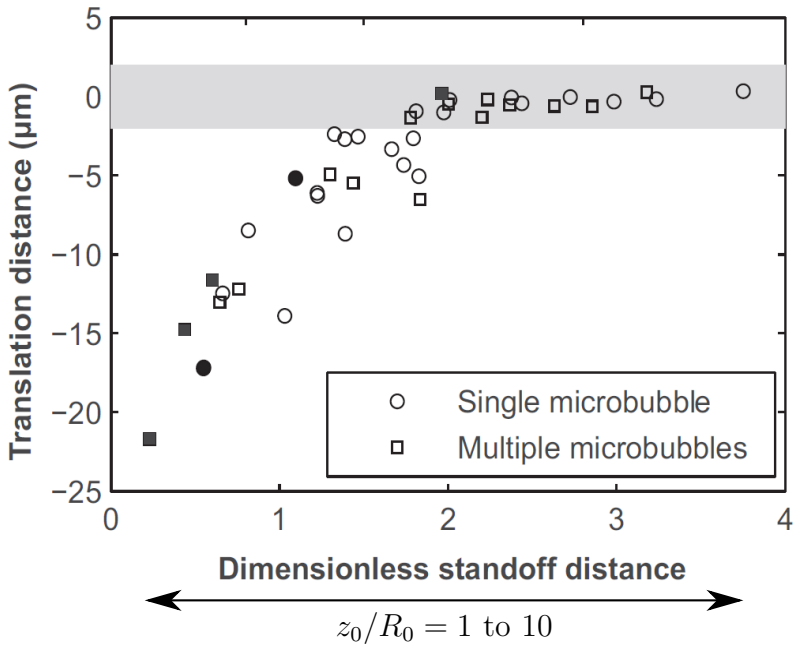

Figure 6.7: Taken from Figure 6 of Chen et al.[3] This figure summarizes the relationship between distance from the interface and the amount of bubble translation, where translation is always directed away from the interface.

farthest, bubble translation is directed away from the interface. As for the largest standoff distance, the reverberant fields are almost completely negligible at $15R_0$, making the overall translation observed at this distance likely unobservable in experiments and outside the distance explored by Chen et al.[3] As with Brujan et al.,[1] a direct comparison with results reported by Chen et al.[3] is difficult since their experiment involved a bubble entrained by surrounding tissue layers and driven by an external source. In the present work, the viscoelastic medium is only present on one side of the bubble, and the bubble is in free oscillation. While adding a source to drive the bubble oscillation is trivial, surrounding the bubble with a tissue-like vessel is not.

The fourth observation regarding Fig. 6.5 is that the oscillation amplitude of the bubble affects the overall direction of bubble translation. This is seen more clearly in the eight simulations shown in Fig. 6.5 for $\mu_2 = 10^7\,\text{Pa}$ and at distance $z_0/R_0 = 12.5$, where the corresponding time-domain simulations for $R(t)$ and $X(t)$ are shown in Figs. 6.8 and 6.9, respectively. Figure 6.8 shows the pulsation of a freely oscillating bubble of radius $3\,\mu\text{m}$ at distance $12.5R_0$ from an interface between water and a viscoelastic solid for $0.2 \leq R(0)/R_0 \leq 0.9$. The viscoelastic medium has a density $\rho_2 = 1012\,\text{kg/m}^3$, compressional wave speed $c_2 = 1518\,\text{m/s}$, shear viscosity $\eta_2 = 2 \times 10^{-3}\,\text{Pa·s}$, zero bulk viscosity, and shear moduli $\mu_2 = 10^7\,\text{Pa}$ and $\mu_{2,M} = 10^5\,\text{Pa}$. While bubble translation is our main focus, visualizing the bubble pulsation helps to qualitatively reference the level of nonlinearity under consideration. We reiterate that as the bubble pulsation becomes more nonlinear, the maximum

amplitude of the corresponding spectrum of the volume velocity will lower in frequency [Fig. 6.3(b)]. Thus, as the pulsation becomes more nonlinear, the phase of $\widehat{Q}(\omega)$, which helps us predict the direction of bubble translation, covers a broader region of frequencies below the natural frequency of the bubble. Figure 6.9 shows the corresponding translation of the bubble pulsation in Fig. 6.8. As with the simulations for $\mu_2 = 10^6$ Pa in Fig. 6.4, we note that the direction of bubble translation changes from away to toward the interface for $R(0)/R_0 \leq 0.5$. Thus, we expect that the phase of $\widehat{g}_{\text{rev}}(\omega_0)$ is greater than $\pi/2$, while it is closer to 0 for frequencies below w_0.[†] In other words, the phase of the reverberant pressure gradient is more similar to that for a water-air interface than that for a water-steel interface.

[†]The limits of the vertical axis for bubble pulsation are constant, but change for bubble translation; the limits of the vertical axis were modified for bubble translation so that smaller amounts of translation (corresponding to mild amount of initial compression of the bubble) are visible.

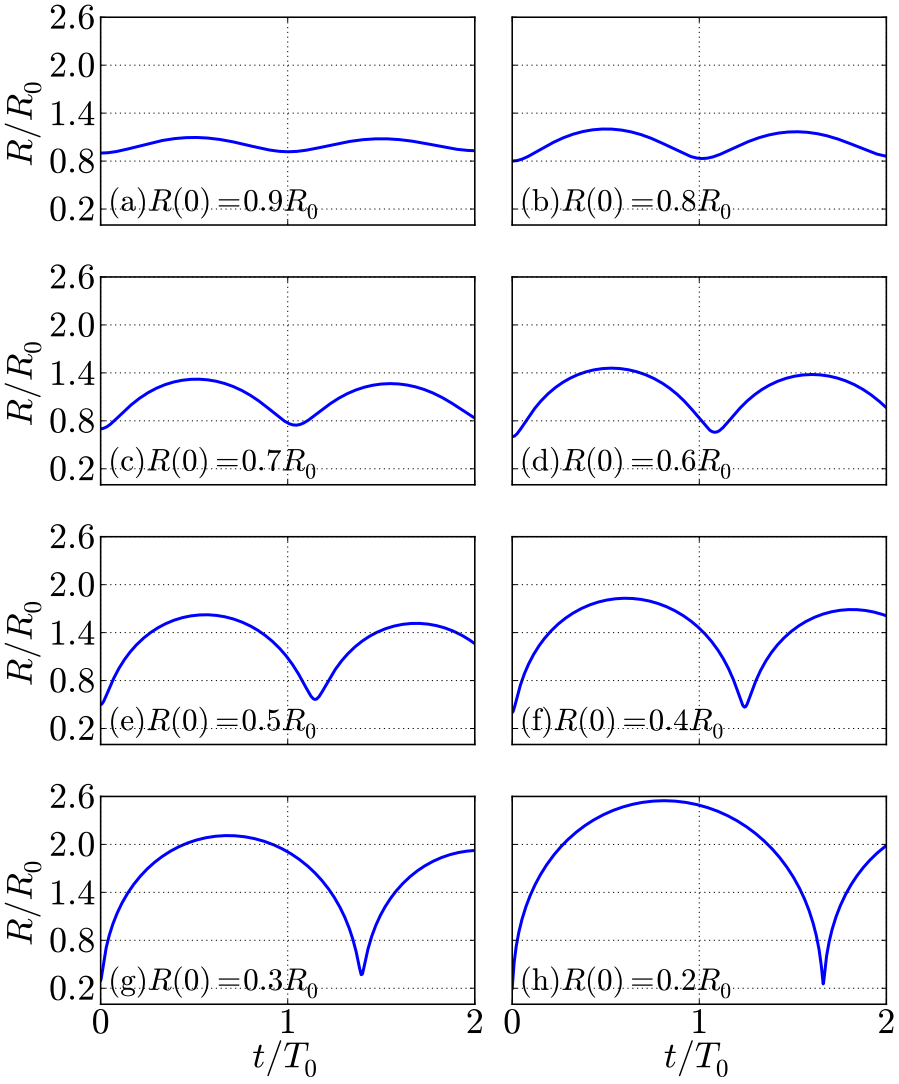

Figure 6.8: Pulsation of a bubble of radius 3 μm in free oscillation at distance $12.5R_0$ from an interface between water and a viscoelastic medium with $\rho_2 = 1012\,\mathrm{kg/m^3}$, $c_2 = 1518\,\mathrm{m/s}$, $\mu_2 = 10^7\,\mathrm{Pa}$, $\eta_2 = 2\times10^{-3}\,\mathrm{Pa{\cdot}s}$, zero bulk viscosity, and $\mu_{2,M} = 10^5\,\mathrm{Pa}$. The corresponding bubble translation is shown in Fig. 6.9.

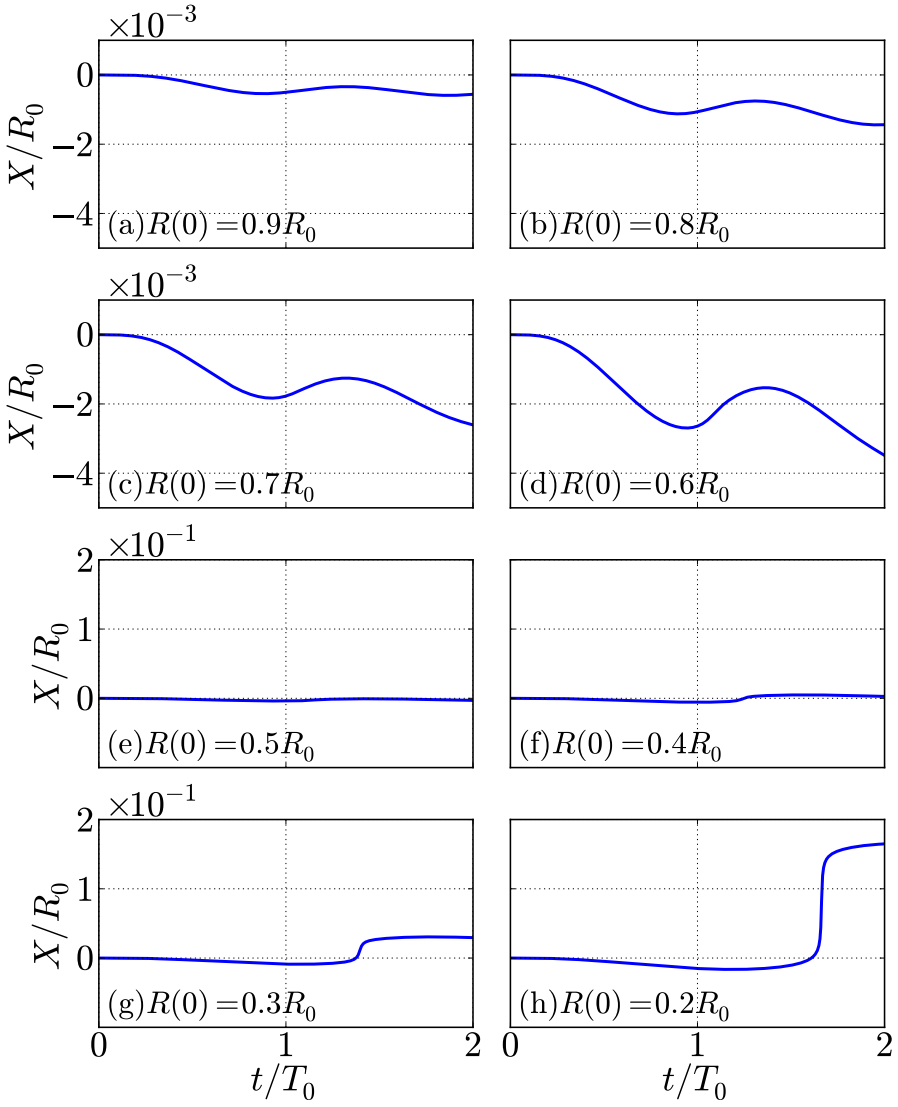

Figure 6.9: Translation of a bubble of radius 3 μm in free oscillation at distance $12.5R_0$ from an interface between water and a viscoelastic medium with $\rho_2 = 1012\,\mathrm{kg/m^3}$, $c_2 = 1518\,\mathrm{m/s}$, $\mu_2 = 10^7$ Pa, $\eta_2 = 2\times10^{-3}$ Pa·s, zero bulk viscosity, and $\mu_{2,M} = 10^5$ Pa. Bubble translation is directed away from the interface for $R(0)/R_0 \geq 0.6$, but toward the interface otherwise. The corresponding bubble pulsation is shown in Fig. 6.8.

In order to verify that the phase of $\widehat{g}_{\mathrm{rev}}(\omega)$, at and below ω_0, would have correctly inferred the direction of bubble translation in Fig. 6.9, Fig. 6.10 shows the (a) magnitude and (b) phase of $\widehat{g}_{\mathrm{rev}}(\omega)$ corresponding to the time-domain simulations shown in Figs. 6.8 and 6.9. Hence, the spectrum is evaluated at a distance of $37.5\,\mu$m ($12.5R_0$ for $R_0 = 3\,\mu$m) from an interface between water and a tissue-like solid with density $\rho_2 = 1012\,\mathrm{kg/m^3}$, compressional wave speed

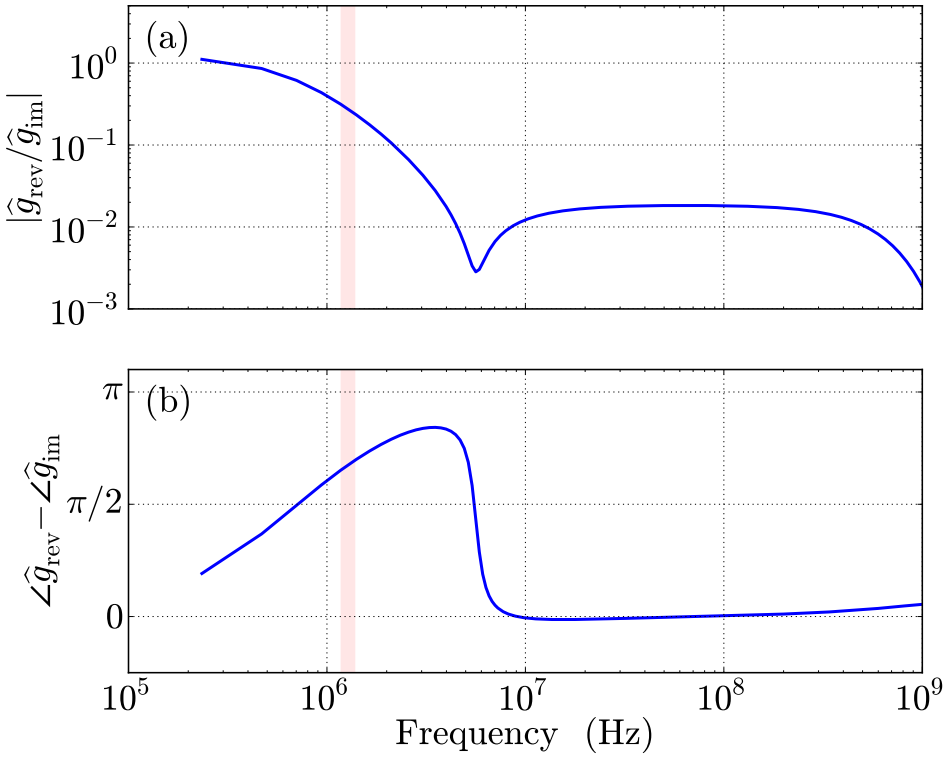

Figure 6.10: The (a) magnitude and (b) phase of $\widehat{g}_{\mathrm{rev}}(\omega)$, normalized by the corresponding image source [Eq. (6.5)], at a distance $37.5\,\mu$m ($12.5R_0$ for $R_0 = 3\,\mu$m) from the interface. The bubble is immersed in water and near a tissue-like solid with $\rho_2 = 1012\,\mathrm{kg/m^3}$, $c_2 = 1518\,\mathrm{m/s}$, $\mu_2 = 10^7\,\mathrm{Pa}$, $\eta_2 = 2{\times}10^{-3}\,\mathrm{Pa{\cdot}s}$, zero bulk viscosity, and $\mu_{2,M} = 10^5\,\mathrm{Pa}$.

$c_2 = 1518\,\mathrm{m/s}$, shear viscosity $\eta_2 = 2 \times 10^{-3}\,\mathrm{Pa{\cdot}s}$, zero bulk viscosity, shear modulus $\mu_2 = 10^7\,\mathrm{Pa}$, and modulus $\mu_{2,M} = 10^5\,\mathrm{Pa}$ associated with the Kelvin model [Eq. (5.4)]. For low initial compressions, the bubble oscillates linearly and the phase of $\widehat{g}_{\mathrm{rev}}(\omega_0)$ (within the region of frequencies shaded in pink) is closer to that for an water-air interface ($\angle\widehat{g}_{\mathrm{rev}}(\omega_0) = \pi$) than that for a water-steel interface ($\angle\widehat{g}_{\mathrm{rev}}(\omega_0) = 0$). Thus, modest translation directed away from the interface is expected. However, for higher amounts of initial compression, the frequencies present in the bubble pulsation are predominantly lower than ω_0 (e.g., see Fig. 6.3), where the phase of $\widehat{g}_{\mathrm{rev}}(\omega)$ is more similar to that for a water-steel interface. Thus, the direction of translation changes. The only difference in the spectrum shown in Fig. 6.10 and the spectrum for $\mu_2 = 10^7\,\mathrm{Pa}$ in Fig. 6.2 is the distance from the interface. We note that increasing the distance seems to shift the entire spectrum downward in frequency, such that the region of $\widehat{g}_{\mathrm{rev}}(\omega)$ with phase similar to that for a water-air interface is closer to the natural frequency of the bubble.

6.3 Conclusions

This chapter presented qualitative analysis of bubble translation for moderately nonlinear bubble pulsation. We showed that the higher-order term originally given in the bubble-translation equation [the third term on the right-hand side of Eq. (6.4)] was still sufficiently small, compared to other terms, to be ignored. In addition, because our primary focus was on bubble translation, the equation describing bubble pulsation was also left unmodified.

The direction of bubble translation was determined for standoff distances ranging from $z_0 = 2.5R_0$ to $15R_0$, initial compression of the bubble radius between $0.2 \leq R(0)/R_0 \leq 0.9$, and shear modulus for a tissue-like viscoelastic medium varying from $\mu_2 = 10^4\,\text{Pa}$ to $10^7\,\text{Pa}$. The phase of $\widehat{g}_{\text{rev}}$ was still helpful to predict direction of bubble translation; however, the spectrum of the volume velocity of the bubble was also necessary to determine which frequencies were present in the bubble pulsation. Although one cannot assume the reverberant pressure gradient is proportional to the product of $\widehat{g}_{\text{rev}}(\omega)$ and $\widehat{Q}$ without also assuming a stationary bubble, using both these spectra was necessary to qualitatively approximate the frequency band at which the phase of $\widehat{g}_{\text{rev}}$ was most important. For increasingly nonlinear pulsation, the frequency band associated with the peak magnitude of $|\widehat{Q}|$ grew wider and occurred at lower frequencies. Hence, the phase of $\widehat{g}_{\text{rev}}$ used to predict the direction of bubble translation for more nonlinear simulations was, at times, significantly lower then ω_0. Regardless, the phase of $\widehat{g}_{\text{rev}}$ over the region of frequencies corresponding to a maximum in $|\widehat{Q}|$ correctly predicts the direction of bubble translation, where approximately $\pi/2 < \angle\widehat{g}_{\text{rev}} < 3\pi/2$ corresponds to translation away from the interface and $-\pi/2 < \angle\widehat{g}_{\text{rev}} < \pi/2$ corresponds to translation toward the interface.

A lowering in frequency of the peak amplitude of $|\widehat{Q}|$ for larger amounts of initial compression also caused, in some cases, a change in the direction of bubble translation. This change in direction occurred in this chapter when the phase of $\widehat{g}_{\text{rev}}$ at ω_0 was slightly greater than $\pi/2$, and then changed to a

value less than $\pi/2$ for $\omega < \omega_0$. The research outlined in this chapter only begins to scratch the surface regarding the physics that may be gleaned from these types of numerical simulations. It also represents a necessary stepping stone to better understand bubble translation due to interaction between the bubble and the fluid-solid interface.

Chapter 7

Summary and Future Work

The research embodied in this dissertation is two-fold. First, we have developed a numerical model to simulate a translating and spherically pulsating bubble in a viscous fluid near a viscoelastic medium. Second, we have determined that direction of bubble translation, and hence the likely direction of jetting, can be inferred from the phase of $\widehat{g}_{\text{rev}}(\omega)$ at the oscillation frequency of the bubble. While this inherently restricts the analysis to low-amplitude pulsation, this is a first step in developing a model which can quickly determine direction of bubble translation. For high-amplitude pulsation, the phase of $\widehat{g}_{\text{rev}}(\omega)$ is still a viable tool to predict bubble translation; however, the frequency at which the phase is evaluated is considerably lower than ω_0.

Chapter 2 introduced the mathematical theory required to model the radial and translational dynamics of a spherical bubble near a liquid-solid interface. The nonlinear temporal differential equations describing spherical pulsation of the bubble and its translation were introduced. In addition, linear differential equations describing the particle displacement of the liquid and the viscoelastic medium were presented. The linear differential equations were solved for the portion of the field being reflected from the interface and

coming back onto the bubble by using a Green's function method. An analytical expression was obtained for this portion of the pressure and its gradient (referred to in this dissertation as the reverberant pressure and reverberant pressure gradient) in the angular-spectrum domain, where a derivation of the specific boundary conditions and algebraic manipulations used to obtain this result were found in Appendices A and B, respectively.

Chapter 3 covered the details regarding numerical implementation of the equations outlined in Chapter 2. Relevant nondimensionalization was discussed for the bubble dynamics equations, and the details of obtaining a temporal expression for the reverberant pressure and its gradient were also detailed. In addition, this chapter also outlined possible simplifications to simulations involving a translating bubble. It was shown that the reverberant pressure and its gradient may be computed with enough accuracy with a stationary Green's function, where the point of evaluation is altered depending on the actual bubble location. In other words, once the equation for bubble translation indicated that the bubble had moved outside of a predefined tolerance, the bubble location used to compute the reverberant fields was updated to a new location closer to the actual bubble location. In this way, the computation was greatly simplified.

The last topic in Chapter 3 detailed the many inaccuracies which are likely to be encountered during these numerical simulations. The first topic covered was a possible numerical instability introduced into the computation of the reverberant fields by using discrete bubble locations. This instability

was correlated with the separation of the discrete bubble locations and the distance of the bubble from the interface. While this was minimally precarious while simulating a bubble near a rigid wall, more care must be taken when considering a bubble near a tissue-like solid since the direction of bubble translation may change entirely over a distance of only a few bubble radii.[1] The other specifications outlined were the aliasing that is introduced into the reverberant spectra when the bubble nears the interface, the zero-frequency component of the frequency spectra of the time derivative of ϕ_{rev} and g_{rev}, and proper resolution of the spectra near the resonance frequency of the bubble.

Chapter 4 showed that, despite all of the numerical difficulties, this problem can be correctly simulated. Verification of the simulation occurred over three steps. First, bubble translation was neglected while bubble pulsation was checked. We showed that the natural oscillation frequency was altered due to the presence of a rigid or pressure-release boundary. We also showed that the time of collapse for high-amplitude bubble pulsation was very close to the Rayleigh collapse time. Second, the function $\widehat{\phi}_{\text{rev}}(\omega)$ (which is used to compute the reverberant pressure) for a water-steel interface and compared to that for a water-rigid interface. We also compared $\widehat{\phi}_{\text{rev}}(\omega)$ for a water-air interface with the that for a water-vacuum interface. Both of these comparisons were graphically identical. Third, we performed temporal simulations of the bubble dynamics including translation and showed that the frequency of oscillation was still correctly altered when using the reverberant fields calculated via the Green's function outlined in Section 2.3.3, and that direction bubble

translation due to the liquid-solid interface was consistent with experiment.

Chapter 5 presented several studies regarding direction of bubble translation near tissue-like media. In this chapter, we first show that the phase of $\widehat{g}_{\text{rev}}(\omega)$ at the oscillation frequency of the bubble is indicative of the overall direction of bubble translation—when considering low-amplitude pulsation. Thus, this metric was computed for different circumstances by varying the bubble size, the distance of the bubble from the interface, the shear viscosity of the liquid, and all of the material properties of the viscoelastic medium. This chapter reported regions where the phase of $\widehat{g}_{\text{rev}}(\omega_0)$ corresponds to bubble translation away from the interface.

In addition, Chapter 5 presented the phase of $\widehat{g}_{\text{rev}}(\omega_0)$ for various models used for tissue-like solids. We began with the Voigt model, but also employed the Kelvin and Maxwell models. The results for the Kelvin model were presented in almost identical form as those for the Voigt model, while the results for the Maxwell model were inferred from the Kelvin model. Both the Kelvin and Maxwell models displayed two basic features that have been observed experimentally: increased shear modulus, and decreased shear viscosity, for increasing frequency. Thus, the Kelvin model was shown to be the most realistic and was therefore used in the time-domain simulations presented in Chapter 6. For all of the tissue models studied, the phase of $\widehat{g}_{\text{rev}}(\omega_0)$ corresponding to bubble translation away from the interface nearly always occurred in regions where the real part of the complex shear modulus for the viscoelastic medium was greater than the magnitude of the imaginary part

of the complex shear modulus for either the fluid or the viscoelastic medium: $\mathrm{Re}\{\tilde{\mu}_2\} > |\mathrm{Im}\{\tilde{\mu}_2\}|, |\tilde{\mu}_1|$.

Chapter 6 focused on the direction of bubble translation for moderately nonlinear bubble pulsation. This chapter showed that the phase of $\widehat{g}_{\mathrm{rev}}(\omega)$ was still useful in predicting direction of bubble translation; however, only after the magnitude of the volume velocity $\widehat{Q}$ was analyzed in conjunction with the magnitude of $\widehat{g}_{\mathrm{rev}}(\omega)$. While the product of these two spectra is only valid in predicting the reverberant pressure gradient for a stationary bubble, this tool was shown to still be helpful in the context of a moving bubble. Direction of bubble translation was summarized for several simulations of a bubble in free oscillation, where the simulations began with the bubble initially compressed to varying sizes and located at various distances from many different tissue-like solids. We found that direction of bubble translation could be understood, even for high-amplitude bubble pulsation, after understanding the frequency spectrum of the bubble pulsation in conjunction with the phase of $\widehat{g}_{\mathrm{rev}}(\omega)$ at those frequencies.

In addition to these chapters, there were several appendices written to support the information presented in the main text. Appendix A covered the derivation of the remaining boundary conditions used in Chapter 2, while Appendix B used these boundary conditions to derive an analytical expression of the coefficient defining the portion of the scalar potential in the fluid which propagates back onto the bubble, the coefficient B. Appendix C justified the use of a different momentum equation to compute the reverberant pressure

than that used to solve the Green's function in Chapter 2. Appendix D outlined the steps to move an analytically-tractable angular-spectrum solution of the coefficient B—for a moving source—to the time domain. Appendix E derived analytical expressions for the reverberant spectra when the angular frequency $\omega = 0$. Last, Appendix F simplified the expression obtained for the coefficient B for several different limiting cases, which were used in Chapter 4 to validate the computation of the general form of the coefficient B.

Any future work for this project should be carefully considered. While it is possible to continue to develop the time-domain bubble dynamics simulations to increasing levels of accuracy, there is other low-hanging fruit which involves less computational rigor. For example, most of Chapter 5 explored direction of bubble translation by computing the phase of $\widehat{g}_{\text{rev}}(\omega)$ [related to the reverberant pressure gradient in Eq. (2.65)]. However, this was only done for a single frequency and a single geometry. Exploring the effect of the phase of $\widehat{g}_{\text{rev}}(\omega_0)$ at frequencies below ω_0 (the frequencies which correspond to larger magnitudes of $\widehat{Q}$ during moderately nonlinear bubble pulsation) could yield valuable insight. Additionally, more work could be done on analyzing the analytical results in the angular-spectrum domain. This dissertation correlated direction of bubble translation with the phase of $\widehat{g}_{\text{rev}}(\omega)$ in the spatial and frequency domains; however, it may be possible to correlate direction of bubble translation with various regions of angular spectrum. An attractive side of more rigorously exploring the angular-spectrum domain is that the analysis could be performed almost entirely analytically.

Experimental work may also be a possible future extension of the work in this dissertation, since the overall number of experiments supporting this type of work are relatively few. In order to create a model which better represents the physical system, we require a more thorough understanding of the dynamics of tissue-like media—particularly at ultrasonic frequencies. Since reflection coefficients have previously been employed to characterize tissue at ultrasonic frequencies,[78,79] perhaps one way to obtain a related quantity is through tracking the direction of bubble translation.

Appendix A

Derivation of Interface Boundary Conditions

In this appendix we derive Eqs. (2.50) and (2.51), starting with the basic equations of elasticity. These equations are used to formulate the expressions for continuity of normal and shear stress at the liquid-solid interface.[†]

We begin by expressing the stress tensor in terms of scalar and vector displacement potentials. In index notation, the stress-strain relationship is

$$\sigma_{ij} = \lambda \epsilon_{kk} \delta_{ij} + 2\mu \epsilon_{ij} \,, \tag{A.1}$$

where λ and μ are the Lamé parameters, δ_{ij} is the Kronecker delta, and ϵ_{ij} is a component of the strain tensor, related to the displacement field by

$$\epsilon_{ij} = \frac{1}{2}\left(\frac{\partial u_i}{\partial x_j} + \frac{\partial u_j}{\partial x_i}\right) .$$

In cylindrical coordinates, the relevant components of the strain tensor are

[†]The boundary conditions which impose continuity of displacement were derived in Section 2.3.1 of the main text of the dissertation.

[Eq. (1.8) of Landau and Lifshitz[83]]

$$\epsilon_{rr} = \frac{\partial u_r}{\partial r}\,,$$
$$\epsilon_{\varphi\varphi} = \frac{1}{r}\frac{\partial u_\varphi}{\partial \varphi} + \frac{u_r}{r}\,,$$
$$\epsilon_{zz} = \frac{\partial u_z}{\partial z}\,,$$
$$\epsilon_{rz} = \frac{1}{2}\left(\frac{\partial u_r}{\partial z} + \frac{\partial u_z}{\partial r}\right)\,,$$

where substitution of these strains into Eq. (A.1) gives

$$\sigma_{zz} = \lambda\left(\boldsymbol{\nabla}\cdot\mathbf{u}\right) + 2\mu\frac{\partial u_z}{\partial z} \tag{A.2}$$

for the normal stress, and

$$\sigma_{rz} = \mu\left(\frac{\partial u_r}{\partial z} + \frac{\partial u_z}{\partial r}\right) \tag{A.3}$$

for the shear stress. A Helmholtz decomposition of the displacement field ($\mathbf{u} = \boldsymbol{\nabla}\phi + \boldsymbol{\nabla}\times\boldsymbol{\psi}$), where the field variables are assumed axially symmetric, produces

$$\sigma_{zz} = \lambda\nabla^2\phi + 2\mu\left[\frac{\partial^2\phi}{\partial z^2} + \frac{1}{r}\frac{\partial(r\psi)}{\partial r}\right]\,, \tag{A.4}$$
$$\sigma_{rz} = \mu\left[2\frac{\partial^2\phi}{\partial r\partial z} - \frac{\partial^2\psi}{\partial z^2} + \frac{1}{r}\frac{\partial(r\psi)}{\partial r}\right]\,, \tag{A.5}$$

where $\boldsymbol{\psi} = \psi\mathbf{e}_\varphi$. In order to use the general solutions for the angular spectra of the potential functions ϕ and ψ [Eqs. (2.42)–(2.45)], we must transform these equations into the angular-spectrum domain. A temporal Fourier transform of Eq. (A.4) allows the first term to be simplified since $\nabla^2\widehat{\phi} = -k_l\widehat{\phi}$, and a

zero-order Hankel transform allows us to simplify the second term, giving

$$\mathcal{H}_0\{\mathcal{F}_\omega[\sigma_{zz}]\} = \left(-\lambda k_l^2 + 2\mu\kappa_l^2\right)\Phi + 2\mu\mathcal{H}_0\left\{\frac{1}{r}\frac{\partial}{\partial r}\left(r\widehat{\psi}\right)\right\}, \tag{A.6}$$

where the coefficient multiplying Φ can be rewritten as $\mu(\kappa^2 + \kappa_t^2) = \alpha$. Using integration by parts, we express the Hankel transform on the right-hand side of Eq. (A.6) in terms of a first-order Hankel transform:

$$\begin{aligned}
\mathcal{H}_0\left\{\frac{1}{r}\frac{\partial}{\partial r}\left(r\widehat{\psi}\right)\right\} &= \int_0^\infty \frac{\partial}{\partial r}\left(r\widehat{\psi}\right) J_0(\kappa r)\, dr \\
&= \widehat{\psi} J_0(\kappa r) r\Big|_0^\infty - \int_0^\infty \widehat{\psi}\frac{\partial}{\partial r} J_0(\kappa r) r\, dr \\
&= \kappa \int_0^\infty \widehat{\psi} J_1(\kappa r) r\, dr \\
&= \kappa\mathcal{H}_1\left\{\widehat{\psi}\right\}. \qquad \text{(A.7)}
\end{aligned}$$

Therefore, the second term on the right-hand side of Eq. (A.6) can be written as $\beta\Psi$, where $\beta = 2\mu\kappa$, yielding

$$\mathcal{H}_0\left\{\mathcal{F}_\omega[\sigma_{zz}]\right\} = \alpha\Phi + \beta\frac{\partial}{\partial z}\Psi,$$

which is consistent with Eq. (7.226) of Achenbach.[60] Equating the normal stress in the fluid with that in the solid and evaluating these expressions at the interface ($z = 0$), and in the angular-spectrum domain, produces

$$\begin{aligned}
\alpha_1\Phi^{(1)} + \beta_1\frac{\partial}{\partial z}\Psi^{(1)} &= \alpha_2\Phi^{(2)} + \beta_2\frac{\partial}{\partial z}\Psi^{(2)}, \\
\alpha_1\left(A + B\right) + \beta_1\kappa_{t,1}D &= \alpha_2 E - \beta_2\kappa_{t,2}F, \qquad \text{(A.8)}
\end{aligned}$$

where Eq. (A.8) matches Eq. (2.51).

For the shear stress, we follow a similar method by moving Eq. (A.5) into the angular-spectrum domain. This time, however, we employ a first-order Hankel transform. Thus,

$$\mathcal{H}_1\{\mathcal{F}_\omega[\sigma_{rz}]\} = 2\mu\frac{\partial}{\partial z}\mathcal{H}_1\left\{\frac{\partial\widehat{\phi}}{\partial r}\right\} - \mu\frac{\partial^2\Psi}{\partial z^2} + \mathcal{H}_1\left\{\frac{\partial}{\partial r}\left[\frac{1}{r}\frac{\partial}{\partial r}\left(r\widehat{\psi}\right)\right]\right\} . \tag{A.9}$$

The first-order Hankel transform in the first term on the right-hand side of Eq. (A.9) is expressed in terms of a zero-order Hankel transform by using integration by parts and a recurrence relation for derivatives of Bessel functions:[†]

$$\begin{aligned}
\mathcal{H}_1\left\{\frac{\partial\widehat{\phi}}{\partial r}\right\} &= \int_0^\infty \frac{\partial\widehat{\phi}}{\partial r} J_1(\kappa r) r\, dr \\
&= \widehat{\phi} J_1(\kappa r) r\Big|_0^\infty - \int_0^\infty \widehat{\phi}\frac{\partial}{\partial r}[J_1(\kappa r) r]\; dr \\
&= -\kappa\int_0^\infty \widehat{\phi} J_0(\kappa r) r\, dr \\
&= -\kappa\mathcal{H}_0\left\{\widehat{\phi}\right\} .
\end{aligned} \tag{A.10}$$

Equation (A.9) is further simplified by considering Bessel's equation of order one:[84]

$$\frac{\partial^2\widehat{\psi}}{\partial r^2} + \frac{1}{r}\frac{\partial\widehat{\psi}}{\partial r} - \frac{\widehat{\psi}}{r^2} = -\kappa^2\widehat{\psi} . \tag{A.11}$$

Substitution of Eq. (A.11) into the last term on the right-hand side of Eq. (A.9) yields $-\mathcal{H}_1\left\{\kappa^2\widehat{\psi}\right\}$. Thus, Eq. (A.9) can be rewritten as

$$\mathcal{H}_1\{\mathcal{F}_\omega[\sigma_{rz}]\} = -\beta\frac{\partial}{\partial z}\Phi - \mu\left(\kappa^2 + \frac{\partial^2}{\partial z^2}\right)\Psi , \tag{A.12}$$

[†]The recurrence relation is $\frac{\partial}{\partial x}[xJ_1(x)] = xJ_0(x)$, Eq. (11.15) of Arfken and Weber.[84]

which is consistent with Eq. (7.227) of Achenbach.[60] Substitution of the general solutions for the field variables in the liquid and the solid [Eqs. (2.42)–(2.45)] into Eq. (A.12) and evaluating the resulting expression at the interface ($z = 0$) yields

$$-\beta_1 \frac{\partial}{\partial z}\Phi^{(1)} - \mu_1\left(\kappa^2 + \frac{\partial^2}{\partial z^2}\right)\Psi^{(1)} = -\beta_2 \frac{\partial}{\partial z}\Phi^{(2)} - \mu_2\left(\kappa^2 + \frac{\partial^2}{\partial z^2}\right)\Psi^{(2)},$$
$$\beta_1 \kappa_{l,1}(A - B) - \alpha_1 D = \beta_2 \kappa_{l,2} E - \alpha_2 F\,. \tag{A.13}$$

where Eq. (A.13) is identical to Eq. (2.50).

Appendix B

Derivation of B

In this appendix, we solve for the unknown coefficient B in terms of the source coefficient A in Eqs. (2.48) to (2.51). These equations are repeated here for convenience:

$$\kappa(A+B)+\kappa_{t,1}D=\kappa E-\kappa_{t,2}F\,, \tag{B.1}$$

$$-\kappa_{l,1}(A-B)+\kappa D=-\kappa_{l,2}E+\kappa F\,, \tag{B.2}$$

$$\beta_1\kappa_{l,1}(A-B)-\alpha_1 D=\beta_2\kappa_{l,2}E-\alpha_2 F\,, \tag{B.3}$$

$$\alpha_1(A+B)+\beta_1\kappa_{t,1}D=\alpha_2 E-\beta_2\kappa_{t,2}F\,. \tag{B.4}$$

We begin by eliminating the coefficient E from Eqs. (B.1) to (B.4) in two steps: (1) by multiplying Eq. (B.1) by α_2 and Eq. (B.4) by κ and subtracting the two expressions, and (2) by multiplying Eq. (B.2) by β_2 and adding it to Eq. (B.3). The results of these operations yield

$$(\beta_1\kappa-\alpha_2)\kappa_{t,1}D+(\alpha_1-\alpha_2)\kappa\,(A+B)=(\alpha_2-\beta_2\kappa)\kappa_{t,2}F \tag{B.5}$$

for the first step, and

$$(\beta_2\kappa-\alpha_1)D+(\beta_1-\beta_2)\,\kappa_{l,1}(A-B)=(\beta_2\kappa-\alpha_2)F \tag{B.6}$$

for the second. In order to eliminate the coefficients D and F from Eqs. (B.5) and (B.6), we need two additional equations from Eqs. (B.1) to (B.4)—where the coefficient E has been eliminated. Thus, multiplying Eq. (B.1) by $2\mu_2\kappa_{l,2}$ and subtracting it from Eq. (B.3) gives

$$-(2\,\mu_2\,\kappa_{l,2}\,\kappa_{t,1}+\alpha_1)D-(\beta_2\kappa_{l,2}+\beta_1\,\kappa_{l,1})B+(\beta_1\,\kappa_{l,1}-\beta_2\,\kappa_{l,2})A = (2\,\mu_2\,\kappa_{l,2}\,\kappa_{t,2}-\alpha_2)F\,, \quad \text{(B.7)}$$

and multiplying Eq. (B.2) by α_2, Eq. (B.4) by $\kappa_{l,2}$, and adding these expressions together produces

$$(\beta_1\,\kappa_{l,2}\,\kappa_{t,1}+\alpha_2\,\kappa)D+(\alpha_1\,\kappa_{l,2}+\alpha_2\,\kappa_{l,1})B+(\alpha_1\,\kappa_{l,2}-\alpha_2\,\kappa_{l,1})A = (\alpha_2\,\kappa-\beta_2\,\kappa_{l,2}\,\kappa_{t,2})F\,. \quad \text{(B.8)}$$

We eliminate the coefficient F from Eqs. (B.5) to (B.8) by first multiplying Eq. (B.6) by $\kappa_{t,2}$ and adding it to Eq. (B.5),

$$\begin{aligned}&[(\beta_1\kappa-\alpha_2)\kappa_{t,1}+(\beta_2\kappa-\alpha_1)\kappa_{t,2}]D\\&\quad+[(\alpha_1-\alpha_2)\kappa-(\beta_1-\beta_2)\kappa_{l,1}\kappa_{t,2}]B\\&\quad+[(\alpha_1-\alpha_2)\kappa+(\beta_1-\beta_2)\kappa_{l,1}\kappa_{t,2}]A=0\,,\end{aligned} \quad \text{(B.9)}$$

and multiplying Eq. (B.7) by κ and adding this to Eq. (B.8), yielding

$$\begin{aligned}&[(\beta_1-\beta_2)\kappa_{l,2}\kappa_{t,1}-(\alpha_1-\alpha_2)\kappa]D\\&\quad+[(\alpha_1-\beta_2\,\kappa)\kappa_{l,2}-(\beta_1\kappa-\alpha_2)\kappa_{l,1}]B\\&\quad+[(\alpha_1-\beta_2\kappa)\kappa_{l,2}+(\beta_1\kappa-\alpha_2)\kappa_{l,1}]A=0\,.\end{aligned} \quad \text{(B.10)}$$

Last, we remove the coefficient D from Eqs. (B.9) and (B.10) by multiplying Eq. (B.9) by the expression multiplying the coefficient D in Eq. (B.10), $[(\beta_1 - \beta_2)\kappa_{l,2}\kappa_{t,1} - (\alpha_1 - \alpha_2)\kappa]$, multiplying Eq. (B.10) by the expression multiplying the coefficient D in Eq. (B.9), $[(\beta_1\kappa - \alpha_2)\kappa_{t,1} + (\beta_2\kappa - \alpha_1)\kappa_{t,2}]$, and subtracting the two resulting equations. This results in

$$[(C_1 - C_4) + (C_2 + C_3)]B + [(C_1 + C_4) + (C_2 - C_3)]A = 0\,, \tag{B.11}$$

where

$$\begin{aligned}
C_1 &= [(\beta_1 - \beta_2)\kappa_{l,2}\kappa_{t,1} - (\alpha_1 - \alpha_2)\kappa]\,(\alpha_1 - \alpha_2)\kappa\,,\\
C_2 &= [(\beta_1\kappa - \alpha_2)\kappa_{t,1} + (\beta_2\kappa - \alpha_1)\kappa_{t,2}]\,(\beta_2\kappa - \alpha_1)\kappa_{l,2}\,,\\
C_3 &= [(\beta_1\kappa - \alpha_2)\kappa_{t,1} + (\beta_2\kappa - \alpha_1)\kappa_{t,2}]\,(\beta_1\kappa - \alpha_2)\kappa_{l,1}\,,\\
C_4 &= [(\beta_1 - \beta_2)\kappa_{l,2}\kappa_{t,1} - (\alpha_1 - \alpha_2)\kappa]\,(\beta_1 - \beta_2)\kappa_{l,1}\kappa_{t,2}\,.
\end{aligned}$$

Solving for the coefficient B in Eq. (B.11) and rearranging terms thus results in Eq. (2.58):

$$B = -\frac{(C_1 + C_2) - (C_3 - C_4)}{(C_1 + C_2) + (C_3 - C_4)}A\,. \tag{B.12}$$

Appendix C

Derivation of Pressure Equation

In this appendix we discuss the assumptions required to reduce the momentum equation used to obtain the Green's function [Eq. (2.6)] to the momentum equation used to calculate the reverberant pressure [Eq. (2.63)]. For this analysis, we consider an infinite viscous fluid, and the momentum equation is thus

$$\left(\lambda + \zeta\frac{\partial}{\partial t} + \eta\frac{\partial}{\partial t}\right)\boldsymbol{\nabla}\boldsymbol{\nabla}\cdot\mathbf{u} + \eta\frac{\partial}{\partial t}\boldsymbol{\nabla}\cdot\boldsymbol{\nabla}\mathbf{u} - \rho\frac{\partial^2\mathbf{u}}{\partial t^2} = \mathbf{0}\,, \tag{C.1}$$

where λ is the first Lamé parameter, ζ is the bulk viscosity, η is the shear viscosity, and we have dropped the subscripts used in the main text (to indicate fluid parameters) for simplicity. The acoustic pressure p in the fluid can be calculated via[†]

$$p = \lambda\boldsymbol{\nabla}\cdot\mathbf{u}\,, \tag{C.2}$$

which is commonly referred to as Hooke's law. Substitution of Eq. (C.2) into Eq. (C.1) allows us to rewrite the first term of Eq. (C.1) in terms of a pressure gradient, yielding

$$\boldsymbol{\nabla}p = \left(\zeta\frac{\partial}{\partial t} + \eta\frac{\partial}{\partial t}\right)\boldsymbol{\nabla}\boldsymbol{\nabla}\cdot\mathbf{u} + \eta\frac{\partial}{\partial t}\nabla^2\mathbf{u} - \rho\frac{\partial^2\mathbf{u}}{\partial t^2}\,, \tag{C.3}$$

[†]Equation (4.9) of Landau and Lifshitz.[83]

which is given in one-dimensional form in Eq. (9B-1b) of Blackstock.[85] By assuming the displacement field is irrotational $\mathbf{u} = \boldsymbol{\nabla}\varphi$, and we simplify Eq. (C.3) to be

$$p = \left(\zeta\frac{\partial}{\partial t} + 2\eta\frac{\partial}{\partial t}\right)\nabla^2\varphi - \rho\frac{\partial^2\varphi}{\partial t^2}\,. \tag{C.4}$$

Equation (C.2) is also simplified after assuming an irrotational velocity field, producing $p = \lambda\nabla^2\varphi$. Therefore, we substitute p/λ for $\nabla^2\varphi$ in Eq. (C.4) to obtain

$$\left[1 - \left(\frac{\zeta + 2\eta}{\lambda}\right)\frac{\partial}{\partial t}\right]p = -\rho\frac{\partial^2\varphi}{\partial t^2}\,. \tag{C.5}$$

The ratio of either shear or bulk viscosity to the Lamé parameter λ for water or blood is on the order of 10^{-12} seconds. Consequently, the second term on the left-hand side of Eq. (C.5) can be dropped in this analysis, yielding

$$p = -\rho\frac{\partial^2\varphi}{\partial t^2}\,. \tag{C.6}$$

It is generally safe to disregard the term involving viscosity in Eq. (C.5) when considering free-space wave propagation over short distances (pg. 15 of Dowling and Ffowcs Williams[34]); however, the contribution of viscosity in altering the field reflected from an interface can be significant.[86,87] Thus, while we use Eq. (C.6) to calculate the reflected fields produced by the liquid-solid interface, the Green's function must necessarily include viscosity. Once the correct amplitude and phase of the portion of the Green's function corresponding to the reverberant pressure gradient are known, Eq. (C.6) may then be employed to calculate the reverberant pressure or its gradient. In other words,

only after we have computed the Green's function—incorporating viscosity—can we calculate the corresponding pressure field via Eq. (C.6).

The last step required to transform Eq. (C.6) into Eq. (2.63) is to express the scalar displacement potential as a convolution of the source function $S(t, \mathbf{X})$ [defined in Eq. (2.9)] with the scalar potential of the Green's function ϕ:

$$\varphi = \int_{-\infty}^{\infty} \int_{\mathbf{X}_0} \phi[t - \tau; \mathbf{x}, \mathbf{X}_0]\, S[\tau, \mathbf{X}(\tau)]\; d\mathbf{X}_0 d\tau \,,$$

or, equivalently,

$$\varphi = \int_{-\infty}^{\infty} \int_{\mathbf{X}_0} \phi[\tau; \mathbf{x}, \mathbf{X}_0]\, S[t - \tau, \mathbf{X}(t - \tau)]\; d\mathbf{X}_0 d\tau \,. \tag{C.7}$$

A more compact solution of Eq. (C.6) is obtained by considering the velocity potential $\dot{\varphi}$ instead of the displacement potential, where the dot indicates a derivative in time. Hence, a time derivative of Eq. (C.7) produces an expression for the velocity potential, yielding

$$\dot{\varphi} = \int_{-\infty}^{\infty} \int_{\mathbf{X}_0} \phi[\tau; \mathbf{x}, \mathbf{X}_0]\, \frac{\partial}{\partial t} S[t - \tau, \mathbf{X}(t - \tau)]\; d\mathbf{X}_0 d\tau \,, \tag{C.8}$$

where

$$\frac{\partial}{\partial t} S[t - \tau, \mathbf{X}(t - \tau)] = Q(t - \tau) \delta[\mathbf{x} - \mathbf{X}(t - \tau)] \,.$$

Substitution of (C.8) in Eq. (C.6) admits

$$\begin{aligned} p &= -\rho \frac{\partial}{\partial t} \int_{-\infty}^{\infty} \phi[\tau; \mathbf{x}, \mathbf{X}(t - \tau)]\, Q(t - \tau)\, d\tau \\ &= -\rho \frac{\partial}{\partial t} \int_{-\infty}^{\infty} \phi[t - \tau; \mathbf{x}, \mathbf{X}(\tau)]\, Q(\tau)\, d\tau \,, \end{aligned} \tag{C.9}$$

which matches Eq. (2.63) if one assumes p and ϕ are only the portion of the field variable which is reflected from the interface. This relationship between pressure and the volume velocity for a moving source is also employed by Levine et al. for a source in free-space [Eq. (4) of Levine and Candel[41]].

Appendix D

Expressing the Reverberant Fields in the Time Domain

In this appendix we solve analytically for the reverberant pressure produced by a point source near a rigid wall with a slip condition at its surface. We illustrate only the steps needed to express the solution in the time domain, beginning with in the angular-spectrum domain. To begin, we evaluate Eq. (2.63) analytically. The solution for the coefficient B is Eq. (F.13),

$$B(\mathbf{X}_0) = A \tag{D.1}$$

$$= -\frac{1}{2\kappa_{l,1}} e^{-\kappa_{l,1} z_0}\,, \tag{D.2}$$

where the coefficient A was given in Eq. (2.57) for a source located at point $(0,0,-z_0)$. Substitution of Eq. (D.1) into Eq. (2.62) produces the result for the portion of the scalar potential of the Green's function, ϕ_{rev}, which corresponds to the reverberant pressure in the fluid:

$$\begin{aligned}\phi_{\text{rev}} &= \mathcal{F}_\omega^{-1}\left\{-\frac{1}{2\pi}\int_0^\infty \frac{e^{\kappa_{l,1}(z-z_0)}}{2\kappa_{l,1}} J_0(\kappa r)\kappa\, d\kappa\right\} \\ &= \mathcal{F}_\omega^{-1}\left\{-\frac{1}{4\pi}\int_0^\infty \frac{e^{\kappa_{l,1}(z-z_0)}}{\kappa_{l,1}} \kappa\, d\kappa\right\} \quad \text{for} \quad r = 0\,.\end{aligned} \tag{D.3}$$

Because we evaluate the integrand at $r = 0$, the solution of the reverberant pressure is restricted to the z axis.[†] The inverse angular spectrum is further simplified by rewriting the integrand in terms of $\kappa_{l,1}$, where $\kappa_{l,1}^2 = \kappa^2 - k_{l,n}^2$ and $\kappa_{l,1}\, d\kappa_{l,1} = \kappa\, d\kappa$, yielding

$$\phi_{\text{rev}} = \mathcal{F}_{\omega}^{-1}\left\{ -\frac{1}{4\pi} \int_{-ik_{l,1}}^{\infty} e^{\kappa_{l,1}(z-z_0)}\, d\kappa_{l,1} \right\} . \tag{D.4}$$

The integral is now evaluated over the complex function $\kappa_{l,1}$, and the lower limit of the integrand is chosen to be $-ik_{l,1}$ since $k_{l,1} \geq 0$ and $\text{Im}\{\kappa_{l,1}\} \leq 0$. Performing the integration for the inverse spatial transform produces

$$\phi_{\text{rev}} = \mathcal{F}_{\omega}^{-1}\left\{ \frac{e^{-ik_{l,1}(z-z_0)}}{4\pi\,(z-z_0)} \right\} . \tag{D.5}$$

The coefficient B is obtained by assuming a lossless fluid, where $c_{l,1} \to c_1$ since it is not a function of frequency and $k_{l,1} = \omega/c_1$. Hence, the resulting temporal inverse transform produces[‡]

$$\phi_{\text{rev}} = \frac{\delta\left(t + \frac{z-z_0}{c_1}\right)}{4\pi\,(z-z_0)} . \tag{D.6}$$

After evaluation of Eq. (D.6) at the bubble location, substitution of the resulting expression into Eq. (2.63) gives

$$p_{\text{rev}} = -\rho_1 \frac{\partial}{\partial t} \int_{-\infty}^{\infty} \frac{\delta\left(t - \tau + \frac{z-z_b(\tau)}{c_1}\right)}{4\pi\,[z - z_b(\tau)]} Q(\tau)\, d\tau , \tag{D.7}$$

[†]The inverse transform is still analytically tractable without restriction to the axis of symmetry, known as Weyl's integral [Eq. (2.64) of Williams[64]]; however, we are interested only in the field along the axis of symmetry and therefore make the simplification in the beginning.

[‡]The inverse Fourier transform of a complex exponential is a delta function. See, for example, Eq. (1.36) of Williams.[64]

where $\mathbf{X}(\tau) = [0, 0, -z_b(\tau)]$. Equation (D.7) shows that the pressure is calculated after an arbitrary, yet known, path of translation is specified. For a stationary source $[z_b(t) = z_0]$, the reverberant pressure traveling back onto the bubble ($z = -z_0$) reduces to

$$p_{\text{rev}} = \rho_1 \frac{\dot{Q}(t - 2z_0/c_1)}{4\pi\,(2z_0)}\,,$$

which is the pressure radiated from a point source a distance $2z_0$ away (an image source), as given in Eq. (10D-7) of Blackstock.[85]

Appendix E

Zero-Frequency Limit of the Reverberant Field

In this appendix we derive expressions for the frequency spectra of the reverberant fields at $\omega = 0$. First we obtain a zero-frequency expression for $\widehat{\phi}_{\text{rev}}$, which can then be differentiated to obtain a zero-frequency expression for $\widehat{g}_{\text{rev}}$. Both spectra involve the coefficient B [Eq. (2.58)]. Thus, the coefficient is repeated here for convenience:

$$B = -\frac{(C_1 + C_2) - (C_3 - C_4)}{(C_1 + C_2) + (C_3 - C_4)} A \,, \tag{E.1}$$

where

$$\begin{aligned}
C_1 &= \left[(\beta_1 - \beta_2)\kappa_{l,2}\kappa_{t,1} - (\alpha_1 - \alpha_2)\kappa\right](\alpha_1 - \alpha_2)\kappa \,, \\
C_2 &= \left[(\beta_1\kappa - \alpha_2)\kappa_{t,1} + (\beta_2\kappa - \alpha_1)\kappa_{t,2}\right](\beta_2\kappa - \alpha_1)\kappa_{l,2} \,, \\
C_3 &= \left[(\beta_1\kappa - \alpha_2)\kappa_{t,1} + (\beta_2\kappa - \alpha_1)\kappa_{t,2}\right](\beta_1\kappa - \alpha_2)\kappa_{l,1} \,, \\
C_4 &= \left[(\beta_1 - \beta_2)\kappa_{l,2}\kappa_{t,1} - (\alpha_1 - \alpha_2)\kappa\right](\beta_1 - \beta_2)\kappa_{l,1}\kappa_{t,2} \,.
\end{aligned}$$

In the limit as $\omega \to 0$, the quantities $\kappa_{l,n}$ and $\kappa_{t,n}$ are expanded as

$$\kappa_{l,n} = \kappa\left(1 - \frac{\omega^2}{2\kappa^2 c_{l,n}^2} + \cdots\right) , \tag{E.2}$$

$$\kappa_{t,n} = \kappa\left(1 - \frac{\omega^2}{2\kappa^2 c_{t,n}^2} + \cdots\right) . \tag{E.3}$$

We remind the reader that the region of integration over κ is at $\kappa = 0$. While one may wonder if the expansions in Eqs. (E.2) and (E.3) are valid as κ becomes very small, we reiterate that ω is also going to zero. Thus, ω is assumed to be sufficiently small such that ω/κ is at most unity, and the remaining portions higher-order terms in the expansions (the ratios $1/2c_{l,n}^2$ and $1/2c_{t,n}^2$) are also assumed sufficiently small that the expansion is still valid. Because we assume $c_{t,n} \ll c_{l,n}$ (i.e., a low-shear viscoelastic medium is assumed, $\mu_2 \ll K_2$), the second term in Eq. (E.3) dominates the second term in Eq. (E.2). Hence, we retain only the first term in Eq. (E.2), while we retain the first two terms in

Eq. (E.3). Substitution of these simplifications into Eq. (E.1) gives

$$C_1 = \left[-(\beta_1 - \beta_2)\frac{\omega^2\rho_1}{2\tilde{\mu}_1} + (\rho_1 - \rho_2)\kappa\omega^2 \right] \times \left[(\beta_1 - \beta_2)\kappa^2 - (\rho_1 - \rho_2)\kappa\omega^2 \right], \tag{E.4}$$

$$C_2 = \left[-(\beta_1 - \beta_2)\frac{\omega^2}{2}\left(\frac{\rho_1}{\tilde{\mu}_1} - \frac{\rho_2}{\tilde{\mu}_2}\right) + (\rho_1 + \rho_2)\kappa\omega^2 - \frac{\omega^4\rho_1\rho_2}{2\kappa}\left(\frac{1}{\tilde{\mu}_1} + \frac{1}{\tilde{\mu}_2}\right) \right] \times \left[-(\beta_1 - \beta_2)\kappa^2 + \rho_1\kappa\omega^2 \right], \tag{E.5}$$

$$C_3 = \left[-(\beta_1 - \beta_2)\frac{\omega^2}{2}\left(\frac{\rho_1}{\tilde{\mu}_1} - \frac{\rho_2}{\tilde{\mu}_2}\right) + (\rho_1 + \rho_2)\kappa\omega^2 - \frac{\omega^4\rho_1\rho_2}{2\kappa}\left(\frac{1}{\tilde{\mu}_1} + \frac{1}{\tilde{\mu}_2}\right) \right] \times \left[(\beta_1 - \beta_2)\kappa^2 + \rho_2\kappa\omega^2 \right], \tag{E.6}$$

$$C_4 = \left[-(\beta_1 - \beta_2)\frac{\omega^2\rho_1}{2\tilde{\mu}_1} + (\rho_1 - \rho_2)\kappa\omega^2 \right] \times \left[(\beta_1 - \beta_2)\kappa^2\left(1 - \frac{\rho_2\omega^2}{2\kappa^2\tilde{\mu}_2}\right) \right], \tag{E.7}$$

where the shear wave speeds have been expressed in terms of their complex shear modulus and density. Using the preceding expressions, the denominator of Eq. (E.1) is written as

$$C_1 + C_2 + C_3 - C_4 = \frac{\rho_1\rho_2\kappa^2\omega^4\tilde{\mu}_2}{\tilde{\mu}_1}\left[1 + \frac{2\tilde{\mu}_1}{\tilde{\mu}_2} + \frac{\tilde{\mu}_1^2}{\tilde{\mu}_2^2} - \frac{\omega^2}{2\kappa^2\tilde{\mu}_2}(\rho_1 + \rho_2)\left(1 + \frac{\tilde{\mu}_1}{\tilde{\mu}_2}\right)\right], \tag{E.8}$$

and the numerator as

$$
\begin{aligned}
&-\left(C_1 + C_2 - C_3 + C_4\right) A \\
&\qquad = \Bigg[-4\rho_2\kappa^4\omega^2\tilde{\mu}_2 \left(1 - \frac{\tilde{\mu}_1}{\tilde{\mu}_2}\right) \\
&\qquad\qquad + \frac{\rho_1\rho_2\kappa^2\omega^4\tilde{\mu}_2}{\tilde{\mu}_1} \left(1 + 2\frac{\tilde{\mu}_1\rho_2}{\rho_1\tilde{\mu}_2} - 3\frac{\tilde{\mu}_1^2}{\tilde{\mu}_2^2}\right) + O(\omega^6) \Bigg] A \,, \qquad \text{(E.9)}
\end{aligned}
$$

where terms of $O(\omega^6)$ have been dropped.

In order to further simplify this expression, we recall that the shear modulus of the fluid is determined only by its shear viscosity. Thus, at low frequencies $|\tilde{\mu}_1| \ll |\tilde{\mu}_2|$. Therefore, in this limit we perform a binomial expansion of the denominator (to first order) and multiply the resulting expression with the numerator to produce the following approximate solution for coefficient B:

$$
B = -\frac{4\tilde{\mu}_1\kappa^2}{\rho_1\omega^2} B_0 A + B_1 A + O(\omega^2) \,, \qquad \text{(E.10)}
$$

where

$$
B_0 = \left(1 - 2\frac{\tilde{\mu}_1}{\tilde{\mu}_2} - 2\frac{\tilde{\mu}_1^2}{\tilde{\mu}_2^2}\right) , \qquad \text{(E.11)}
$$

$$
B_1 = \left[1 - 4\frac{\tilde{\mu}_1}{\tilde{\mu}_2} - 6\frac{\tilde{\mu}_1^2}{\tilde{\mu}_2^2}\left(1 + \frac{\rho_2}{\rho_1}\right)\right] . \qquad \text{(E.12)}
$$

Equation (E.10) is a low-frequency approximation of the coefficient B, used in the angular-spectrum integration yielding $\widehat{\phi}_{\text{rev}}$ and $\widehat{g}_{\text{rev}}$. A particularly nice feature of this approximation is that the inverse spatial transform is now analytically tractable. In addition, the source coefficient A has not been modified;

hence, Eq. (E.10) is valid for any source configuration in the fluid. Thus, $\widehat{\phi}_{\text{rev}}$ along the z axis is

$$\begin{aligned}\widehat{\phi}_{\text{rev}} &= \frac{1}{2\pi}\int_0^\infty B e^{\kappa_{l,1}z}\kappa\, d\kappa \\ &= -\frac{2\tilde{\mu}_1 B_0}{\pi\rho_1\omega^2}\int_0^\infty \kappa^3 A e^{\kappa_{l,1}z}\, d\kappa + \frac{B_1}{2\pi}\int_0^\infty A e^{\kappa_{l,1}z}\, d\kappa \\ &= \left[\frac{8\tilde{\mu}_1 B_0}{\rho_1\omega^2 D^2}(1 - ik_{l,1}D) - B_1\right]\frac{e^{ik_{l,1}D}}{4\pi D}\,, \end{aligned} \tag{E.13}$$

where $D = z_0 - z$ for $-z_0 \le z < 0$, the bubble location being $-z_0$ (see, e.g., Fig. 2.1).

The reverberant pressure and its gradient are related to ϕ_{rev} and g_{rev}, respectively, through a derivative with respect to time. Hence, we multiply $\widehat{\phi}_{\text{rev}}$ and $\widehat{g}_{\text{rev}}$ by $-i\omega$. Considering material 1 to be the fluid, we let $\tilde{\mu}_1 = -i\omega\eta_1$, yielding

$$-i\omega\widehat{\phi}_{\text{rev}} = \left[-\frac{8\eta_1 B_0}{\rho_1 D^2}(1 - ik_{l,1}D) + i\omega B_1\right]\frac{e^{ik_{l,1}D}}{4\pi D}\,, \tag{E.14}$$

and thus

$$\lim_{\omega\to 0} -i\omega\widehat{\phi}_{\text{rev}} = -\frac{\eta_1}{4\pi\rho_1(D/2)^3}\,. \tag{E.15}$$

The derivative of Eq. (E.15) with respect to z gives the zero-frequency component of $\widehat{g}_{\text{rev}}$:

$$\lim_{\omega\to 0} -i\omega\widehat{g}_{\text{rev}} = -\frac{3\eta_1}{8\pi\rho_1(D/2)^4}\,. \tag{E.16}$$

If the elastic medium is instead rigid, the same zero-frequency components given in Eqs. (E.15) and (E.16) are obtained—assuming the fluid is

viscous. This is verified by expanding the case for an interface between a fluid and a rigid wall [Eq. (F.19)] using Eqs. (E.2) and (E.3), yielding

$$B = -\left(\frac{4\tilde{\mu}_1\kappa^2}{\rho_1\omega^2} - 1\right) A + O(\omega^2)\,, \tag{E.17}$$

which is identical to Eq. (E.10) for $B_0 = B_1 = 1$. If the elastic medium were more like air, then the assumption made earlier that $|\tilde{\mu}_1| \ll |\tilde{\mu}_2|$ would no longer hold. However, the low-frequency limit for an interface between a fluid and a pressure release interface is obtained after we substitute Eqs. (E.2) and (E.3) into Eq. (F.23), producing

$$B = \left(\frac{4\tilde{\mu}_1\kappa^2}{\rho_1\omega^2} - 1\right) A + O(\omega^2)\,. \tag{E.18}$$

Equation (E.18) is equal in magnitude, and opposite in phase, to Eq. (E.17). Thus, the magnitudes of the limits given in Eqs. (E.15) and (E.16) also hold for an interface where $|\tilde{\mu}_1| \gg |\tilde{\mu}_2|$.

Appendix F

Simplifications of the Interface Equations

In this appendix we consider different simplifications of the analysis of a point source immersed in a viscous fluid near a viscoelastic half-space. For convenience, the general solutions in the angular-spectrum domain for compressional and shear wave propagation are given here [Eqs. (2.42)–(2.45)]:

$$\Phi^{(1)} = \begin{cases} Ae^{-\kappa_{l,1}z} + Be^{\kappa_{l,1}z} & \text{for } z \geq -z_0\,, \\ Ce^{\kappa_{l,1}z} & \text{for } z \leq -z_0\,, \end{cases} \tag{F.1}$$

$$\Psi^{(1)} = De^{\kappa_{t,1}z}\,, \tag{F.2}$$

$$\Phi^{(2)} = Ee^{-\kappa_{l,2}z}\,, \tag{F.3}$$

$$\Psi^{(2)} = Fe^{-\kappa_{t,2}z}\,, \tag{F.4}$$

where all variables are defined in after Eq. (2.45), and the corresponding propagation directions are shown in Fig. 2.2. Additionally, the boundary conditions written in the angular-spectrum domain and used to determine the unknown coefficients (A, B, C, D, E, and F) are also repeated here for convenience:

[Eq. (2.48) to (2.51)]:

$$\kappa(A+B)+\kappa_{t,1}D=\kappa E-\kappa_{t,2}F\,, \tag{F.5}$$

$$-\kappa_{l,1}(A-B)+\kappa D=-\kappa_{l,2}E+\kappa F\,, \tag{F.6}$$

$$\beta_1\kappa_{l,1}(A-B)-\alpha_1 D=\beta_2\kappa_{l,2}E-\alpha_2 F\,, \tag{F.7}$$

$$\alpha_1(A+B)+\beta_1\kappa_{t,1}D=\alpha_2 E-\beta_2\kappa_{t,2}F\,. \tag{F.8}$$

These equations describe continuity between the fluid and the solid at the interface, for radial particle displacement, normal particle displacement, shear stress, and normal stress, respectively.

F.1 Ideal Fluid-Fluid Interface

The first case considered is when both media are ideal fluids. Under these conditions, neither medium supports shear forces and only compressional wave fields are relevant. Consequently, only continuity of normal stress (pressure) and normal displacement are required. Therefore, only the general solutions in Eqs. (F.1) and (F.3) are needed to satisfy the boundary conditions Eqs. (F.6) and (F.8). Mathematically, the boundary conditions are simplified by setting $\tilde{\mu}_n$, D, and F to zero in Eqs. (F.6) and (F.8). Doing so produces the following simplified boundary conditions:

$$A-B=\frac{\kappa_{l,2}}{\kappa_{l,1}}E\,, \tag{F.9}$$

$$A+B=\frac{\rho_2}{\rho_1}E\,, \tag{F.10}$$

for continuity of normal particle displacement and normal stress, respectively. By adding Eq. (F.9) and (F.10) and solving for E, we obtain

$$E = \frac{2\rho_1\kappa_{l,1}}{\rho_2\kappa_{l,1} + \rho_1\kappa_{l,2}}A\,, \tag{F.11}$$

which represents the portion of the field transmitted into the second fluid. Substitution of this result back into Eq. (F.10) and solving for B produces

$$B = \frac{\rho_2\kappa_{l,1} - \rho_1\kappa_{l,2}}{\rho_2\kappa_{l,1} + \rho_1\kappa_{l,2}}A\,. \tag{F.12}$$

When the second fluid becomes rigid, its specific acoustic impedance tends to infinity. Thus, the first terms in the numerator and denominator of Eq. (F.12) become large and Eq. (F.12) reduces to

$$B = A\,. \tag{F.13}$$

The coefficient A represents the field incident on the boundary, created by the source. Thus, Eq. (F.13) indicates perfect reflection of the incident wave (i.e., $B/A = 1$). In contrast, if the second medium is a vacuum, then its specific acoustic impedance tends to zero. Here, the second term in both the numerator and denominator of Eq. (F.12) become large and the equation reduces to

$$B = -A\,. \tag{F.14}$$

In this case the field reflected from the interface is now in antiphase with the incident field defined by A.

A more traditional form of Eq. (F.12) can be written by considering the source amplitude (the coefficient A) to represent a single plane wave incident

on the interface at an angle θ as measured from the interface normal. Under these circumstances $\kappa = k \sin\theta$, which is interpreted as the component of wave propagation parallel to the interface. Substitution of this result into $\kappa_{l,n}$ gives $\kappa_{l,n} = k\cos\theta_n$. Equation (F.12) then recovers the classical result for reflection from a two-fluid interface:[†]

$$R = \frac{B}{A} = \frac{Z_2 - Z_1}{Z_2 + Z_1}\,, \tag{F.15}$$

where $Z_n = \rho_n c_{l,n}/\cos\theta_n$ is the impedance of the n^{th} medium.

Solutions for the coefficient B in Eqs. (F.13) and (F.14) are simple enough to perform the inverse transform analytically, and are used to check certain cases of the numerical simulations in Chapter 4 of this dissertation.

F.2 Viscous Fluid Near a Rigid or Pressure-Release Surface

Now we reduce the boundary conditions [Eqs. (F.5)–(F.8)] and the general solutions [Eqs. (F.1)–(F.4)] by considering a source immersed in a viscous fluid near a rigid or pressure-release surface. Consequently, we take the second medium to either be rigid or a vacuum.

We first consider a source immersed in a viscous liquid and located near a rigid wall. Thus, the coefficients describing wave propagation in the second medium [E and F in Eqs. (F.3) and (F.4)] are set to zero. For this

[†]Eq. (5B–9a) of Blackstock,[85] or Eq. (2.2.16) of Brekhovskikh.[59]

case we require continuity of particle displacement as the boundary condition. Therefore, Eqs. (F.5) and (F.6) reduce to

$$\kappa(A+B)+\kappa_{t,1}D=0\,, \tag{F.16}$$

$$-\kappa_{l,1}(A-B)+\kappa D=0\,. \tag{F.17}$$

Solving for the coefficients describing reflected waves traveling away from the interface gives

$$D=\frac{2\kappa\kappa_{l,1}}{\kappa^2-\kappa_{t,1}\kappa_{l,1}}A\,, \tag{F.18}$$

$$B=-\frac{\kappa^2+\kappa_{t,1}\kappa_{l,1}}{\kappa^2-\kappa_{t,1}\kappa_{l,1}}A\,, \tag{F.19}$$

for the coefficients corresponding to transverse and longitudinal wave propagation away from the interface, respectively.

The analysis for a source in a viscous fluid near a pressure-release surface is similar in that we do not consider wave propagation in the second medium. However, under these conditions we require that the stress is zero at the interface, instead of the displacement. Hence, Eqs. (F.7) and (F.8) become

$$\beta_1\kappa_{l,1}\,(A-B)-\alpha_1 D=0\,, \tag{F.20}$$

$$\alpha_1\,(A+B)+\beta_1\kappa_{t,1}D=0\,, \tag{F.21}$$

giving, respectively, for the coefficients corresponding to transverse and longi-

tudinal fields traveling away from the interface,

$$D = \frac{2\beta_1\alpha_1\kappa_{l,1}}{\alpha_1^2 - \beta_1^2\kappa_{t,1}\kappa_{l,1}}A\,, \tag{F.22}$$

$$B = -\frac{\alpha_1^2 + \beta_1^2\kappa_{t,1}\kappa_{l,1}}{\alpha_1^2 - \beta_1^2\kappa_{t,1}\kappa_{l,1}}A\,. \tag{F.23}$$

F.3 Ideal Fluid Near an Elastic Solid

The last case considered is an interface between an ideal fluid and an elastic solid. Because viscosity is not considered within the fluid, there is no transverse field in the fluid and the coefficient D is eliminated from the analysis. For this case we match normal particle displacement and normal stress between the fluid and the solid, and we set the shear stress at the interface to zero. Thus, Eqs. (F.6) to (F.8) become

$$-\kappa_{l,1}(A - B) = -\kappa_{l,2}E + \kappa F\,, \tag{F.24}$$

$$0 = \beta_2\kappa_{l,2}E - \alpha_2 F\,, \tag{F.25}$$

$$-\rho_1\omega^2(A + B) = \alpha_2 E - \beta_2\kappa_{t,2}F\,, \tag{F.26}$$

where $\alpha_1 = \tilde{\mu}_1\big(\kappa^2 + \kappa_{t,1}^2\big) \to -\rho_1\omega^2$ as the shear viscosity of the fluid tends to zero. Combining Eqs. (F.24) and (F.26) to eliminate B yields

$$-2\rho_1\omega^2\kappa_{l,1}A = \big(\alpha_2\kappa_{l,1} - \rho_1\omega^2\kappa_{l,2}\big)E - \big(\beta_2\kappa_{t,2}\kappa_{l,1} - \rho_1\omega^2\kappa\big)F,$$

and using this expression along with Eq. (F.25) admits explicit solutions for the coefficients corresponding to the longitudinal and transverse fields in the

solid, respectively:[†]

$$E = -\frac{2\rho_1\omega^2\alpha_2\kappa_{l,1}A}{\kappa_{l,1}\left(\alpha_2^2 - \beta_2^2\kappa_{t,2}\kappa_{l,2}\right) + \rho_1\omega^2\kappa_{l,2}\left(\beta_2\kappa - \alpha_2\right)}\,, \tag{F.27}$$

$$F = -\frac{2\rho_1\omega^2\beta_2\kappa_{l,1}\kappa_{l,2}A}{\kappa_{l,1}\left(\alpha_2^2 - \beta_2^2\kappa_{t,2}\kappa_{l,2}\right) + \rho_1\omega^2\kappa_{l,2}\left(\beta_2\kappa - \alpha_2\right)}\,. \tag{F.28}$$

Last, substitution of Eqs. (F.27) and (F.28) into into Eq. (F.26) gives the expression for the reflected component of the compressional wave,

$$B = \frac{\kappa_{l,1}\left(\alpha_2^2 - \beta_2^2\kappa_{t,2}\kappa_{l,2}\right) - \rho_1\omega^2\kappa_{l,2}\left(\beta_2\kappa - \alpha_2\right)}{\kappa_{l,1}\left(\alpha_2^2 - \beta_2^2\kappa_{t,2}\kappa_{l,2}\right) + \rho_1\omega^2\kappa_{l,2}\left(\beta_2\kappa - \alpha_2\right)}A\,, \tag{F.29}$$

which takes on a different form than the first expression in Eq. (11) in Zhu et al.[61] since this analysis assumes a compressional source removed from the fluid-solid interface.[‡] We emphasize that the expression given here can be used for any axisymmetric source configuration in the fluid, making the expressions very general for studying transmission and reflection due to a host of different interfaces or source functions.

The important quantity in all of the cases illustrated in this appendix is the coefficient corresponding to the reflected compressional wave in the fluid, B. This quantity is used to calculate the reverberant pressure and its gradient in the bubble dynamics simulations outlined in Section 2.1.

[†]Consistent with Eqs. (7.230) and (7.231) of Achenbach,[60] or the last two expressions in Eq. (11) of Zhu et al.[61]

[‡]Zhu et al.[61] considered a force source in contact with the interface.

Bibliography

[1] E.-A. Brujan, K. Nahen, P. Schmidt, and A. Vogel, "Dynamics of laser-induced cavitation bubbles near elastic boundaries: influence of the elastic modulus", Journal of Fluid Mechanics **433**, 283–314 (2001). xiii, xx, 2, 6, 32, 33, 36, 83, 97, 98, 102, 104, 105, 130, 147, 148, 149, 150, 151, 161

[2] T. A. Hay, Yu. A. Ilinskii, E. A. Zabolotskaya, and M. F. Hamilton, "Model for bubble pulsation in liquid between parallel viscoelastic layers", The Journal of the Acoustical Society of America **132**, 124–137 (2012). xiv, 5, 6, 12, 20, 24, 33, 34, 36, 48

[3] H. Chen, A. A. Brayman, W. Kreider, M. R. Bailey, and T. J. Matula, "Observations of translation and jetting of ultrasound-activated microbubbles in mesenteric microvessels", Ultrasound in Medicine & Biology **37**, 2139–2148 (2011). xx, 6, 32, 83, 102, 104, 128, 150, 151

[4] S. Qin and K. W. Ferrara, "The natural frequency of nonlinear oscillation of ultrasound contrast agents in microvessels", Ultrasound in Medicine & Biology **33**, 1140 – 1148 (2007). 1, 2

[5] S. Qin and K. W. Ferrara, "A model for the dynamics of ultrasound contrast agents in vivo", The Journal of the Acoustical Society of America **128**, 1511–1521 (2010). 2

[6] Yu. A. Pishchalnikov, O. A. Sapozhnikov, M. R. Bailey, J. C. Williams Jr., R. O. Cleveland, T. Colonius, L. A. Crum, A. P. Evan, and J. A. McAteer, "Cavitation bubble cluster activity in the breakage of kidney stones by lithotripter shockwaves", Journal of Endourology **17**, 435–446 (2003). 2

[7] E. Johnsen and T. Colonius, "Shock-induced collapse of a gas bubble in shockwave lithotripsy", The Journal of the Acoustical Society of America **124** (2008). 2

[8] M. R. Bailey, L. N. Couret, O. A. Sapozhnikov, V. A. Khokhlova, G. ter Haar, S. Vaezy, X. Shi, R. Martin, and L. A. Crum, "Use of overpressure to assess the role of bubbles in focused ultrasound lesion shape in vitro", Ultrasound in Medicine & Biology **27**, 695 – 708 (2001). 2

[9] M. Bailey, V. Khokhlova, O. Sapozhnikov, S. Kargl, and L. Crum, "Physical mechanisms of the therapeutic effect of ultrasound (a review)", Acoustical Physics **49**, 369–388 (2003). 2

[10] E. Johnsen and T. Colonius, "Damage potential of single-bubble collapse in shockwave lithotripsy", The Journal of the Acoustical Society of America **123**, 3368–3368 (2008). 2

[11] J. B. Freund, T. Colonius, and A. P. Evan, "A cumulative shear mechanism for tissue damage initiation in shock-wave lithotripsy", Ultrasound in Medicine & Biology **33**, 1495 – 1503 (2007). 2

[12] J. B. Freund, "Suppression of shocked-bubble expansion due to tissue confinement with application to shock-wave lithotripsy", The Journal of the Acoustical Society of America **123**, 2867–2874 (2008). 2

[13] E.-A. Brujan, K. Nahen, P. Schmidt, and A. Vogel, "Dynamics of laser-induced cavitation bubbles near an elastic boundary", Journal of Fluid Mechanics **433**, 251–281 (2001). 2, 6

[14] A. Shima, "Studies on bubble dynamics", Shock Waves **7**, 33–42 (1997). 3

[15] Lord. Rayleigh, "On the pressure developed in a liquid during the collapse of a spherical cavity", Philosophical Magazine Series 6 **34**, 94–98 (1917). 3

[16] T. G. Leighton, *The Acoustic Bubble* (Academic Press) (1994). 3, 14, 74

[17] H. N. Oğuz and A. Prosperetti, "The natural frequency of oscillation of gas bubbles in tubes", The Journal of the Acoustical Society of America **103**, 3301–3308 (1998). 3, 4

[18] X. M. Chen and A. Prosperetti, "Thermal processes in the oscillations of gas bubbles in tubes", The Journal of the Acoustical Society of America **104**, 1389–1398 (1998). 4

[19] E. Sassaroli and K. Hynynen, "Forced linear oscillations of microbubbles in blood capillaries", The Journal of the Acoustical Society of America **115**, 3235–3243 (2004). 4

[20] C. Feuillade, "Acoustically coupled gas bubbles in fluids: Time-domain phenomena", The Journal of the Acoustical Society of America **109**, 2606–2615 (2001). 4, 68

[21] D. C. Thomas, "Stability and dynamics of systems of interacting bubbles with time-delay and self-action due to liquid compressibility", Ph.D. dissertation, The University of Texas at Austin (2012). 4, 14, 67, 68

[22] A. Prosperetti and A. Lezzi, "Bubble dynamics in a compressible liquid. part 1. First-order theory", Journal of Fluid Mechanics **168**, 457–478 (1986). 4, 14

[23] A. Lezzi and A. Prosperetti, "Bubble dynamics in a compressible liquid. part 2. Second-order theory", Journal of Fluid Mechanics **185**, 289–321 (1987). 4, 14, 133

[24] C. Heckman, S. Sah, and R. Rand, "Dynamics of microbubble oscillators with delay coupling", Communications in Nonlinear Science and Numerical Simulation **15**, 2735 – 2743 (2010). 4

[25] A. A. Doinikov, R. Manasseh, and A. Ooi, "Time delays in coupled multi-bubble systems (l)", The Journal of the Acoustical Society of America **117**, 47–50 (2005). 4, 6

[26] Yu. A. Ilinskii and E. A. Zabolotskaya, "Cooperative radiation and scattering of acoustic waves by gas bubbles in liquids", The Journal of the Acoustical Society of America **92**, 2837–2841 (1992). 4, 133

[27] J. B. Keller and M. Miksis, "Bubble oscillations of large amplitude", The Journal of the Acoustical Society of America **68**, 628–633 (1980). 4, 14

[28] T. G. Leighton, D. G. Ramble, A. D. Phelps, C. L. Morfey, and P. P. Harris, "Acoustic detection of gas bubbles in a pipe", Acta Acustica united with Acustica **84**, 801–814 (1998-09-01T00:00:00). 5

[29] T. G. Leighton, P. R. White, C. L. Morfey, J. W. L. Clarke, G. J. Heald, H. A. Dumbrell, and K. R. Holland, "The effect of reverberation on the damping of bubbles", The Journal of the Acoustical Society of America **112**, 1366–1376 (2002). 5

[30] J. Cui, M. F. Hamilton, P. S. Wilson, and E. A. Zabolotskaya, "Bubble pulsations between parallel plates", The Journal of the Acoustical Society of America **119**, 2067–2072 (2006). 5

[31] J. C. Atkisson, "Models for acoustically driven bubbles in channels", Ph.D. dissertation, The University of Texas at Austin (2008). 5

[32] A. A. Doinikov and A. Bouakaz, "Ultrasonically induced dynamics of a contrast agent microbubble between two parallel elastic walls", Physics in Medicine and Biology **58**, 6797 (2013). 6

[33] A. Ungar and Z. Alterman, "Acoustic wave propagation from a moving point source", Bulletin of the Seismological Society of America **63**, 1937–1950 (1973). 6

[34] A. P. Dowling and J. E. F. Williams, *Sound and Sources of Sound* (Ellis Horwood Limited) (1983). 6, 16, 37, 175

[35] P. M. Morse and K. U. Ingard, *Theoretical Acoustics* (McGraw-Hill) (1968). 6, 16

[36] K. G. Sabra and D. R. Dowling, "Broadband performance of a time reversing array with a moving source", The Journal of the Acoustical Society of America **115**, 2807–2817 (2004). 6, 38

[37] K. G. Sabra, "Broadband performance of time-reversing arrays in shallow water", Ph.D. dissertation, The University of Michigan (2003), pp. 60–63. 6, 38

[38] H. Schmidt and W. A. Kuperman, "Spectral and modal representations of the Doppler-shifted field in ocean waveguides", The Journal of the Acoustical Society of America **96**, 386–395 (1994). 6, 38

[39] K. Rao, T. Michaud, and H. Schmidt, "Doppler shifts in underwater acoustics using field solutions", in *OCEANS '91. Ocean Technologies and Opportunities in the Pacific for the 90's. Proceedings.*, volume 2, 779–782 (1991). 6, 38

[40] M. J. Lighthill, "On sound generated aerodynamically. I. General theory", Proceedings of the Royal Society of London. Series A. Mathematical and Physical Sciences **211**, 564–587 (1952). 6, 37, 38

[41] H. Levine and S. M. Candel, "Acoustic power output from moving point singularities", The Journal of the Acoustical Society of America **81**, 1695–1702 (1987). 6, 38, 177

[42] M. V. Lowson, "The sound field for singularities in motion", Proceedings of the Royal Society of London. Series A. Mathematical and Physical Sciences **286**, 559–572 (1965). 6, 37, 38

[43] A. A. Doinikov and S. T. Zavtrak, "On the mutual interaction of two gas bubbles in a sound field", Physics of Fluids **7**, 1923–1930 (1995). 6

[44] E. Kurihara, T. A. Hay, Yu. A. Ilinskii, E. A. Zabolotskaya, and M. F. Hamilton, "Model for the dynamics of two interacting axisymmetric spherical bubbles undergoing small shape oscillations", The Journal of the Acoustical Society of America **130**, 3357–3369 (2011). 6, 83

[45] Yu. A. Ilinskii, M. F. Hamilton, and E. A. Zabolotskaya, "Bubble interaction dynamics in Lagrangian and Hamiltonian mechanics", The Journal of the Acoustical Society of America **121**, 786–795 (2007). 6, 12, 13, 14

[46] A. Harkin, T. J. Kaper, and A. Nadim, "Coupled pulsation and translation of two gas bubbles in a liquid", Journal of Fluid Mechanics **445**, 377–411 (2001). 6, 12, 83, 130

[47] H. Chen, W. Kreider, A. A. Brayman, M. R. Bailey, and T. J. Matula, "Blood vessel deformations on microsecond time scales by ultrasonic cavitation", Phys. Rev. Lett. **106**, 034301 (2011). 6

[48] T. A. Hay, Yu. A. Ilinskii, E. A. Zabolotskaya, and M. F. Hamilton, "Model for the dynamics of a spherical bubble undergoing small shape oscillations between parallel soft elastic layers", The Journal of the Acoustical Society of America **134**, 1454–1462 (2013). 7

[49] A. J. Reddy and A. J. Szeri, "Coupled dynamics of translation and collapse of acoustically driven microbubbles", The Journal of the Acoustical Society of America **112**, 1346–1352 (2002). 12, 13

[50] A. A. Doinikov, "Mathematical model for collective bubble dynamics in strong ultrasound fields", The Journal of the Acoustical Society of America **116**, 821–827 (2004). 12, 13

[51] J. Magnaudet and D. Legendre, "The viscous drag force on a spherical bubble with a time-dependent radius", Physics of Fluids **10**, 550–554 (1998). 13

[52] Yu. A. Ilinskii, P. S. Wilson, and M. F. Hamilton, "Bubble growth by rectified diffusion at high gas supersaturation levels", The Journal of the Acoustical Society of America **124**, 1950–1955 (2008). 14, 133

[53] A. Prosperetti, "Thermal effects and damping mechanisms in the forced radial oscillations of gas bubbles in liquids", The Journal of the Acoustical Society of America **61**, 17–27 (1977). 14

[54] M. J. Miksis and L. Ting, "Nonlinear radial oscillations of a gas bubble including thermal effects", The Journal of the Acoustical Society of

America **76**, 897–905 (1984). 14

[55] L. D. Landau and E. M. Lifshitz, *Fluid Mechanics*, 2nd edition (Butterworth-Heinemann) (1987). 15

[56] P. M. Morse and H. Feshbach, *Methods of Theoretical Physics: Part I* (McGraw-Hill) (1953). 17, 18

[57] G. Barton, *Elements of Green's Functions and Propagation: Potentials, Diffusion, and Waves* (Oxford University Press) (1989). 17

[58] D. G. Duffy, *Green's Functions with Applications* (Chapman & Hall/CRC) (2001). 17, 25, 28

[59] L. M. Brekhovskikh and O. A. Godin, *Acoustics of Layered Media I: Plane and Quasi-Plane Waves* (Springer-Verlag) (1990). 20, 190

[60] J. D. Achenbach, *Wave Propagation in Elastic Solids* (Elsevier) (1975). 20, 168, 170, 193

[61] J. Zhu, J. S. Popovics, and F. Schubert, "Leaky Rayleigh and Scholte waves at the fluid–solid interface subjected to transient point loading", The Journal of the Acoustical Society of America **116**, 2101–2110 (2004). 20, 46, 193

[62] A. T. de Hoop and J. H. M. T. van der Hijden, "Generation of acoustic waves by an impulsive point source in a fluid/solid configuration with a

plane boundary", The Journal of the Acoustical Society of America **75** (1984). 20

[63] L. Debnath, *Integral Transforms and Their Applications*, 320 (Chapman & Hall/CRC) (2008). 26

[64] E. G. Williams, *Fourier Acoustics: Sound Radiation and Nearfield Acoustical Holography* (Academic Press) (1999). 28, 30, 67, 179

[65] M. Overvelde, V. Garbin, B. Dollet, N. de Jong, D. Lohse, and M. Versluis, "Dynamics of coated microbubbles adherent to a wall", Ultrasound in Medicine & Biology **37**, 1500 – 1508 (2011). 32

[66] A. D. Pierce, *Acoustics: An Introduction to Its Physical Principles and Applications*, 165 (Acoustical Society of America) (1989). 37, 38

[67] P. M. Morse and K. U. Ingard, *Theoretical Acoustics*, 717–737 (McGraw-Hill) (1968). 37, 38

[68] H. L. Oestreicher, "Field of a spatially extended moving sound source", The Journal of the Acoustical Society of America **29**, 1223–1232 (1957). 37, 38

[69] H. L. Oestreicher, "Supplementary notes to "Field of a spatially extended moving sound source"", The Journal of the Acoustical Society of America **30**, 480–481 (1958). 37

[70] S. Cohen, Alan, and C. Hindmarsh, "Cvode, a stiff/nonstiff ODE solver in C", Computers in Physics **10**, 138–143 (1996). 40, 48

[71] E. A. Zabolotskaya, "Interaction of gas bubbles in a sound field", Soviet Physics. Acoustics. **30**, 365–368 (1984). 83

[72] S. Catheline, J.-L. Gennisson, G. Delon, M. Fink, R. Sinkus, S. Abouelkaram, and J. Culioli, "Measurement of viscoelastic properties of homogeneous soft solid using transient elastography: An inverse problem approach", The Journal of the Acoustical Society of America **116**, 3734–3741 (2004). 97

[73] A. P. Sarvazyan, O. V. Rudenko, S. D. Swanson, J. Fowlkes, and S. Y. Emelianov, "Shear wave elasticity imaging: a new ultrasonic technology of medical diagnostics", Ultrasound in Medicine & Biology **24**, 1419 – 1435 (1998). 97, 101

[74] A. Karpiouk, S. Aglyamov, Yu. Ilinskii, E. Zabolotskaya, and S. Emelianov, "Assessment of shear modulus of tissue using ultrasound radiation force acting on a spherical acoustic inhomogeneity", Ultrasonics, Ferroelectrics and Frequency Control, IEEE Transactions on **56**, 2380–2387 (2009). 97

[75] H. L. Oestreicher, "Field and impedance of an oscillating sphere in a viscoelastic medium with an application to biophysics", The Journal of the Acoustical Society of America **23**, 707–714 (1951). 97

[76] J. Heikkil, T. Karjalainen, M. Vauhkonen, and K. Hynynen, "Simulations of localized harmonic motions on a blood vessel wall induced by an acoustic radiation force used in ultrasound elastography", Physics in Medicine and Biology **51**, 4587 (2006). 97

[77] H. Chen, A. A. Brayman, and T. J. Matula, "Characteristic microvessel relaxation timescales associated with ultrasound-activated microbubbles", Applied Physics Letters **101**, 163704 (2012). 97, 109, 138

[78] E. L. Madsen, H. J. Sathoff, and J. A. Zagzebski, "Ultrasonic shear wave properties of soft tissues and tissuelike materials", The Journal of the Acoustical Society of America **74**, 1346–1355 (1983). 97, 112, 138, 165

[79] L. A. Frizzell, E. L. Carstensen, and J. F. Dyro, "Shear properties of mammalian tissues at low megahertz frequencies", The Journal of the Acoustical Society of America **60**, 1409–1411 (1976). 97, 112, 138, 165

[80] X. Yang and C. Church, "A simple viscoelastic model for soft tissues the frequency range 6-20 MHz", Ultrasonics, Ferroelectrics and Frequency Control, IEEE Transactions on **53**, 1404–1411 (2006). 97

[81] Y. C. Fung, *Biomechanics: Mechanical Properties of Living Tissues*, 40–52, 2nd edition (Springer-Verlag) (1993). 98, 99

[82] S. Nasseri, L. E. Bilston, and N. Phan-Thien, "Viscoelastic properties of pig kidney in shear, experimental results and modelling", Rheologica Acta **41**, 180–192 (2002). 104, 109, 138

[83] L. D. Landau and E. M. Lifshitz, *Theory of Elasticity*, 3rd edition (Pergamon Press) (1986). 167, 174

[84] G. B. Arfken and H. J. Weber, *Mathematical Methods for Physicists*, 6th edition (Elsevier) (2005). 169

[85] D. T. Blackstock, *Fundamentals of Physical Acoustics* (Wiley-Interscience) (2000). 175, 180, 190

[86] G. Mott, "Reflection and refraction coefficients at a fluid-solid interface", The Journal of the Acoustical Society of America **50**, 819–829 (1971). 175

[87] B. Bianco and T. Tommasi, "Influence of viscosity on the reflection coefficient at a fluid–solid interface", The Journal of the Acoustical Society of America **98**, 2374–2376 (1995). 175